

Performance of Ships in Waves

Von der Fakultät für Ingenieurwissenschaften,
Abteilung Maschinenbau und Verfahrenstechnik,
der Universität Duisburg-Essen
zur Erlangung des akademischen Grades
eines Doktors der Ingenieurwissenschaften

Dr.-Ing.

genehmigte Dissertation

von

Sebastian Sigmund

aus

Solingen

Gutachter: Prof. Dr.-Ing. Ould el Moctar
Prof. Dr.-Ing. Milovan Perić

Tag der mündlichen Prüfung: 05. März 2018

Preface

This thesis is part of the requirements for obtaining the degree of Doctor-Ingenieur from the University of Duisburg-Essen. During a time that was both challenging and pleasant, I have performed the presented work at the Institute of Ship Technologies, Maritime Technologies and Transport Systems (ISMT) in Duisburg. This research was funded by Bundesministerium für Wirtschaft und Energie (BMWi) and the European Union.

My supervisor has been Prof. Dr.-Ing. Bettar Ould el Moctar. I thank him for giving me the chance to work within his team. Without his professional and personal support, this thesis would not have been present today. I also thank my colleague Malte Riesner for opening the door and for fruitful discussions regarding my work and other important technical issues. Special thanks also go out to my patient office neighbor Madhi Ghesmi for his mental and technical support. Furthermore, I thank Jens Ley and Dr. Thomas Schellin for their support and all the colleges and the staff of the institute for their helpfulness and for the pleasant working environment. To all of you, I hope to see you soon and I wish you all the best for the future.

Last but not least, I thank my loving family for their considerable support. They absorbed my ups and downs, gave me shelter and were there all the time. Thank you!

Abstract

Due to environmental, economical and safety related issues, power prediction for operational conditions is desired within the maritime industry. In this context, accurate and reliable predictions of ship performance in waves is essential.

In this thesis, advanced numerical methods based on the solution of the Reynolds-averaged Navier-Stokes (RANS) equations were used to perform extensive and systematic investigations of the performance of ships in regular and irregular waves. In particular, the effects of ship speed, skin friction, wave steepness, and encounter angle on the wave-added resistance, and the interaction between wave radiation and wave diffraction forces were analyzed. Moreover, the influence of waves on the nominal wake fraction and the propulsion characteristics was investigated. Therefore, the ship's resistance, propeller open water characteristics and propulsion forces were computed for calm water and for waves. Additionally, the attainable ship speed of a free-running cruise ship in calm water and in regular and irregular waves was computed, and the speed loss was determined. Grid studies has been performed, mean values and oscillation amplitudes were determined carefully using Fourier analysis, and actual wave heights were monitored and used for normalization. Whenever possible, computational results were compared with the results of scale model test measurements. Overall, very good agreement was obtained.

Generally, it was shown that RANS methods are well suited for the prediction of ship performance in waves considering most nonlinear effects. The findings obtained in this work contribute to the understanding of the fundamental physics related to the wave-added resistance and about the propulsion of ships in waves in a sustainable manner. Furthermore, these findings may be used to further develop efficient prediction tools suitable for the ship design process.

Declaration

Part of the work described in this dissertation has previously been published in the following references:

- Sigmund, S. and el Moctar, O. (2018): Advanced numerical and experimental investigation of added resistance of different ship types in short and long waves. *Ocean Engineering* Vol. 147, pp 51-67
- Sigmund, S. and el Moctar, O. (2017): Numerical and Experimental Investigation of Propulsion in Waves. *Ocean Engineering* Vol. 144, pp 35-49
- Sigmund, S. and el Moctar, O. (2016): Numerical Prediction of the Propulsion Characteristics of Ships in Waves. *Proc. 35th Int. Conf. on Ocean, Offshore and Arctic Eng., Busan, South Korea, OMAE2016-54793*
- el Moctar, O., Sigmund, S. Ley, J., and Schellin, T. (2016): Numerical and Experimental Analysis of Added Resistance of Ships in Waves. *Journal of Ocean, Offshore and Arctic Eng.*, 139(1)
- el Moctar, O., Sigmund, S. Ley, J., and Schellin, T. (2015): Numerical and Experimental Analysis of Added Resistance of Ships in Waves. *Proc. 34rd Int. Conf. on Ocean, Offshore, and Arctic Eng., St. Johns, Canada, OMAE2015-42403*
- Ley, J., Sigmund, S. and el Moctar, O. (2014): Numerical Prediction of the Added Resistance of Ships in Waves. *Proc. 33rd Int. Conf. on Ocean, Offshore, and Arctic Eng., San Francisco, USA, OMAE2014-24216*

Contents

| | |
|--|--------------|
| List of Figures | xiii |
| List of Tables | xxiii |
| Nomenclature | xxiv |
| 1 Introduction | 1 |
| 2 Theoretical Background and State of the Art | 5 |
| 2.1 Ship Resistance | 6 |
| 2.2 Propeller / Hull Interaction | 14 |
| 2.2.1 Wake Flow | 14 |
| 2.2.2 Thrust Deduction | 16 |
| 2.3 Propulsion Characteristics | 17 |
| 3 Numerical Methods | 23 |
| 3.1 Governing Equations | 23 |
| 3.2 Free Surface Treatment | 26 |
| 3.3 Discretization | 27 |
| 3.4 Velocity-Pressure Coupling | 28 |
| 3.5 Modeling of Waves | 29 |
| 3.6 Ship Motion | 30 |
| 3.6.1 Euler Angle | 30 |
| 3.6.2 Rigid Body Motion Equations | 32 |
| 3.6.3 Grid Techniques | 33 |
| 3.7 Computational Procedure | 37 |

| | | |
|----------|---|------------|
| 4 | Verification and Validation | 41 |
| 4.1 | Test Cases | 42 |
| 4.2 | Numerical grids and discretization errors | 48 |
| 5 | Wave-Added Resistance | 61 |
| 5.1 | Computational Procedure | 61 |
| 5.2 | Results | 65 |
| 5.2.1 | Effects of Heave and Pitch Motions on the Wave-Added Resistance | 76 |
| 5.2.2 | Effects of Ship Speed on the Wave-Added Resistance | 88 |
| 5.2.3 | Effects of Viscosity on the Wave-Added Resistance . | 92 |
| 5.2.4 | Effects of Wave Steepness on the Wave-Added Resistance | 100 |
| 5.2.5 | Interaction between Radiation and Diffraction Forces | 104 |
| 5.2.6 | Influence of Encounter Angle on the Wave-Added Resistance | 107 |
| 5.3 | Conclusions | 112 |
| 6 | Nominal Wake Field in Waves | 115 |
| 6.1 | Grid Sensitivity Study | 115 |
| 6.2 | Results | 117 |
| 6.3 | Conclusion | 124 |
| 7 | Ship Propulsion in Waves | 127 |
| 7.1 | Experimental and Computational Procedure | 127 |
| 7.2 | Results | 129 |
| 7.2.1 | Propeller Open Water Test | 129 |
| 7.2.2 | Resistance Test | 132 |
| 7.2.3 | Self-Propelled Model | 132 |
| 7.2.4 | Propulsion Characteristics in Waves | 151 |
| 7.3 | Conclusion | 163 |
| 8 | Speed Loss in Waves | 165 |
| 8.1 | Computational Procedure | 166 |
| 8.2 | Speed Loss in Regular Waves | 168 |

| | | |
|----------|---|------------|
| 8.3 | Speed Loss in Irregular Waves | 172 |
| 8.4 | Conclusion | 176 |
| 9 | Conclusion and Outlook | 179 |
| | Bibliography | 185 |

List of Figures

| | | |
|---|--|----|
| 1 | Wave-added resistance of a cruise ship in a regular head waves with a relative length of 1.09 times the ship length - Difference of mean longitudinal force in waves, \bar{F}_X , and calm water resistance, R_T | 7 |
| 2 | The wave-added resistance for a cruise ship, a containership and a tanker at nearly the same speeds | 10 |
| 3 | Current effective wake field for a free-running twin-screw cruise ship in waves. The influence of the ship's hull is clearly visible in the velocity distribution | 15 |
| 4 | Sequence of rotations of yaw, pitch and roll (top to bottom); here, (ξ, η, ζ) are ship fixed and (x, y, z) are global coordinates. G denotes ζ_0 , the origin of the body fixed coordinate system, (Brunswig, 2004). | 31 |
| 5 | Computation of the wave-added resistance for a cruise ship in head waves using the mesh moving technique at $\mathbf{Fn} = 0.223$, $\lambda_W/L = 0.98$ and $\mathbf{h}_W = 3.6m$ | 35 |
| 6 | Computation of the wave-added resistance for a containership in head waves using the mesh morphing technique at $\mathbf{Fn} = 0.218$, $\lambda_W/L = 1.125$ and $\mathbf{h}_W = 6m$ | 36 |
| 7 | Computation of a free-running turning circle for a containership using sliding grid in combination with the mesh moving technique at $\mathbf{Fn} = 0.139$, $\lambda_W/L = 0.85$, $\mathbf{h}_W = 3.8m$ and $\mathbf{n} = 10rps$ | 37 |
| 8 | Schematic solution procedure of the employed numerical methods, (Peric and Schreck, 2009) | 38 |
| 9 | Considered test cases | 41 |

List of Figures

| | | |
|----|---|----|
| 10 | Section plans of the Cruise Ship, the Containership DTC, the Tanker KVLCC2 and the Wigley Hull III | 44 |
| 11 | Configurations of the propulsion components of the Containership DTC (left) and the Cruise Ship (right) | 45 |
| 12 | Experimental setup for the Cruise Ship (top) and the Containership DTC (bottom) (el Moctar, 2016) | 47 |
| 13 | Representative numerical grid of the performed computations; here for the Cruise Ship | 48 |
| 14 | Dimensionless wall distance, y^+ , on wetted surfaces of the Containership DTC at $\mathbf{Re} = 1.0 \cdot 10^7$ and $\mathbf{Fn} = 0.218$ | 50 |
| 15 | Computed total and frictional calm water resistance coefficients versus number of control volumes for the Containership DTC at $\mathbf{Fn} = 0.218$ and $\mathbf{Re} = 1.0 \cdot 10^7$ and the Cruise Ship at $\mathbf{Fn} = 0.159$ and $\mathbf{Re} = 1.1 \cdot 10^7$ | 51 |
| 16 | Heave RAOs for the Containership DTC at $\mathbf{Fn} = 0.218$ and the Tanker KVLCC2 at $\mathbf{Fn} = 0.142$ versus normalized wave frequency and wave length to ship length ratio computed on different sized grids | 53 |
| 17 | Pitch RAOs for the Containership DTC at $\mathbf{Fn} = 0.218$ and the Tanker KVLCC2 at $\mathbf{Fn} = 0.142$ versus normalized wave frequency and wave length to ship length ratio computed on different sized grids | 54 |
| 18 | Wave-added resistance RAOs for the Containership DTC at $\mathbf{Fn} = 0.218$ and the Tanker KVLCC2 at $\mathbf{Fn} = 0.142$ versus normalized wave frequency and wave length to ship length ratio computed on different sized grids | 55 |
| 19 | Representative spatial discretization of a propeller for numerical investigations | 56 |
| 20 | Measured and computed propeller open water characteristics for the Cruise Ship | 57 |
| 21 | Local refinements of the numerical grids ahead of and behind the models | 58 |

| | | |
|----|--|----|
| 22 | Computed wave pattern in calm water (top) and in regular head waves (bottom) of the Containership DTC at $F_n = 0.218$, $\lambda_w/L = 1.125$ and $h_w = 0.12m$ | 66 |
| 23 | Actual and target short wave amplitude near bow of the Tanker KVLCC2 at $F_n = 0.142$ and $\lambda_w/L = 0.3$ | 67 |
| 24 | Computed and measured time histories of heave and pitch motion of the Containership at $F_n = 0.139$, $\lambda_w/L = 0.91$ and $h_w = 0.14m$ | 69 |
| 25 | Computed time histories and mean values of longitudinal forces for the Cruise Ship and the Containership DTC advancing at constant forward speed in calm water and in short regular head waves | 70 |
| 26 | Computed time histories and mean values of longitudinal forces for the Tanker KVLCC2 and the Wigley Hull III advancing at constant forward speed in calm water and in short regular head waves | 71 |
| 27 | Computed time histories and mean values of longitudinal forces for the Cruise Ship and the Containership DTC advancing at constant forward speed in calm water and in intermediately regular head waves | 72 |
| 28 | Computed time histories and mean values of longitudinal forces for the Tanker KVLCC2 and the Wigley hull III advancing at constant forward speed in calm water and in intermediately regular head waves | 73 |
| 29 | Computed time histories and mean values of longitudinal forces for the Cruise Ship and the Containership DTC advancing at constant forward speed in calm water and in long regular head waves | 74 |
| 30 | Computed time histories and mean values of longitudinal forces for the Tanker KVLCC2 and the Wigley hull III advancing at constant forward speed in calm water and in long regular head waves | 75 |

List of Figures

31 Computed and measured RAOs of heave and pitch amplitudes in regular head waves for the Cruise Ship at **F_n = 0.223** 77

32 Computed and measured RAOs of heave and pitch amplitudes in regular head waves for the Containership DTC at **F_n = 0.139** 78

33 Computed and measured RAOs of heave and pitch amplitudes in regular head waves for the Tanker KVLCC2 at **F_n = 0.142** 79

34 Computed and measured RAOs of heave and pitch amplitudes in regular head waves for the Wigley Hull III at **F_n = 0.30** 80

35 Computed and measured phase angles of heave and pitch motions in regular head waves for the Cruise Ship at **F_n = 0.159** 82

36 Computed and measured phase angles of heave and pitch motions in regular head waves for the Containership DTC at **F_n = 0.139** 83

37 Computed and measured phase angles of heave and pitch motions in regular head waves for the Tanker KVLCC2 at **F_n = 0.142** 84

38 Computed and measured wave-added resistance coefficients in regular head waves for the Cruise Ship at **F_n = 0.223** and the Containership DTC at **F_n = 0.139** 85

39 Computed and measured wave-added resistance coefficients in regular head waves for the Tanker KVLCC2 at **F_n = 0.142** and the Wigley Hull III at **F_n = 0.30** 86

40 Comparative computed wave-added resistance coefficients for the Cruise Ship at **F_n = 0.159**, the Containership DTC at **F_n = 0.139** and the Tanker KVLCC2 at **F_n = 0.142** 87

41 Response amplitude operators of computed and measured heave and pitch motions for the Cruise Ship advancing at two different ship speeds in regular head waves 89

| | | |
|----|---|-----|
| 42 | Response amplitude operators of computed and measured heave and pitch motions for the Containership DTC advancing at two different ship speeds in regular head waves . . . | 90 |
| 43 | Comparative computed and measured wave-added resistance coefficients for the Cruise Ship and the Containership DTC advancing at two different ship speeds in regular head waves | 91 |
| 44 | Computed time histories, mean and calm water values of friction force for the Containership DTC at $F_n = 0.139$ and $Re = 6.1 \cdot 10^6$ and the Tanker KVLCC2 at $F_n = 0.142$ and $Re = 2.5 \cdot 10^6$ in short waves | 93 |
| 45 | Computed time histories, mean and calm water values of friction force for the Containership DTC at $F_n = 0.139$ and $Re = 6.1 \cdot 10^6$ and the Tanker KVLCC2 at $F_n = 0.142$ and $Re = 2.5 \cdot 10^6$ in intermediately long waves | 94 |
| 46 | Computed time histories, mean and calm water values of friction force for the Containership DTC at $F_n = 0.139$ and $Re = 6.1 \cdot 10^6$ and the Tanker KVLCC2 at $F_n = 0.142$ and $Re = 2.5 \cdot 10^6$ in long waves | 95 |
| 47 | Computed and measured coefficients of total (red) and frictional (blue) wave-added resistance for the Cruise Ship at $F_n = 0.223$ and the Containership DTC at $F_n = 0.139$ in regular head waves | 96 |
| 48 | Computed and measured coefficients of total (red) and frictional (blue) wave-added resistance for the Tanker KVLCC2 at $F_n = 0.142$ and the Wigley Hull III at $F_n = 0.30$ in regular head waves | 97 |
| 49 | Representative shear stress distributions in calm water (upper hull) and in regular head waves (lower hull) for the Containership DTC at $F_n = 0.139$ and $Re = 6.1 \cdot 10^6$ and the Tanker KVLCC2 at $F_n = 0.142$ and $Re = 2.5 \cdot 10^6$ | 99 |
| 50 | Total and frictional wave-added resistance coefficients at $Re = 6.1 \cdot 10^6$ and $Re = 2.9 \cdot 10^9$ (full scale) of the Containership DTC at $F_n = 0.139$ in regular head waves | 101 |

51 Computed and measured wave-added resistance coefficients in regular head waves of different steepness for the Cruise Ship at **$F_n = 0.223$** 101

52 Computed and measured wave-added resistance coefficients in regular head waves of different steepness for the Tanker KVLCC2 at **$F_n = 0.142$** for the Containership DTC at **$F_n = 0.139$** 102

53 Coefficients of total wave-added resistance (solid), diffraction force (dotted line) and radiation force (dashed line) for the Cruise Ship at **$F_n = 0.223$** , the Containership DTC at **$F_n = 0.139$** 105

54 Coefficients of total wave-added resistance (solid), diffraction force (dotted line) and radiation force (dashed line) for the Tanker KVLCC2 at **$F_n = 0.139$** and the Wigley Hull III at **$F_n = 0.30$** 106

55 Numerical grid used for oblique wave computations (top) and wave pattern of the Cruise Ship at **$F_n = 0.159$** , $\lambda_w/L = 1.09$ and $\mu = 150^\circ$ (bottom) 108

56 Computed and measured RAOs of heave, pitch and roll amplitudes in regular oblique waves for the Cruise Ship at **$F_n = 0.159$** and $\mu = 150^\circ$ 109

57 Computed and measured wave-added resistance coefficients in regular oblique waves for the Cruise Ship at **$F_n = 0.159$** 110

58 Computed and measured wave-added resistance coefficients in regular oblique waves for the Cruise Ship at **$F_n = 0.159$** 111

59 Influence of local refinements on the nominal wake fraction for the Containership DTC at **$F_n = 0.139$** 116

60 Change in the wake field during one encounter period for the Containership DTC at **$F_n = 0.139$** 118

| | | |
|----|---|-----|
| 61 | Time histories and time-averaged values of the wake fraction in short waves as well as calm water values for the Cruise Ship at $F_n = 0.223$, the Containership DTC at $F_n = 0.139$, and the Tanker KVLCC2 at $F_n = 0.142$ | 119 |
| 62 | Time histories and averaged values of the wake fraction in medium long waves as well as calm water values for the Cruise Ship at $F_n = 0.223$, the Containership DTC at $F_n = 0.139$, and the Tanker KVLCC2 at $F_n = 0.142$ | 120 |
| 63 | Time histories and averaged values of the wake fraction in long waves as well as calm water values for the Cruise Ship at $F_n = 0.223$, the Containership DTC at $F_n = 0.139$, and the Tanker KVLCC2 at $F_n = 0.142$ | 121 |
| 64 | Ratio of wake fraction in calm water and in waves against dimensionless wave frequency for the Containership DTC at $F_n = 0.139$ and the Tanker KVLCC2 at $F_n = 0.142$ | 123 |
| 65 | Ratio of wake fraction in calm water and in waves against dimensionless wave frequency for the Cruise Ship at $F_n = 0.223$ | 124 |
| 66 | Axial velocity distribution around the propeller of the Containership DTC in homogeneous inflow | 130 |
| 67 | Computed and measured propeller open water characteristics for the Cruise Ship and the Containership DTC . | 131 |
| 68 | Wave pattern for the Cruise Ship at $F_n = 0.223$, $\lambda_w/L = 1.09$, $h_w = 0.1m$ and $n = 15.53rps$ and for the Containership DTC at $F_n = 0.087$, $\lambda_w/L = 0.85$, $h_w = 0.1m$ and $n = 9.05rps$ | 134 |
| 69 | Axial velocities at aft ship for the Cruise Ship at $F_n = 0.223$, $\lambda_w/L = 1.09$, $h_w = 0.1m$ and $n = 15.53rps$. . . | 135 |
| 70 | Axial velocities at aft ship for the Containership DTC at $F_n = 0.087$, $\lambda_w/L = 0.85$, $h_w = 0.1m$ and $n = 9.05rps$ | 136 |
| 71 | Variation of axial propeller inflow for the Cruise Ship at $F_n = 0.223$, $\lambda_w/L = 1.09$, $h_w = 0.1m$ and $n = 15.53rps$. . . | 137 |
| 72 | Time history of the vertical motion in the propeller plane for the Cruise Ship at $F_n = 0.223$, $\lambda_w/L = 1.09$ and $n = 15.53rps$ | 138 |

List of Figures

73 Non-dimensional heave and pitch for the Cruise Ship at **$F_n = 0.223$** , **$\lambda_w/L = 0.98$** , **$h_w = 0.1m$** and **$n = 15.4rps$** under towed and self-propelled conditions (see Tabel 10) 139

74 Non-dimensional heave and pitch for the Containership DTC at **$F_n = 0.087$** , **$\lambda_w/L = 0.85$** , **$h_w = 0.095m$** and **$n = 10.43rps$**) under towed and self-propelled conditions (see Tabel 10) 140

75 Heave and pitch RAOs for the towed and the self-propelled Cruise Ship at **$F_n = 0.223$** 141

76 Time histories of the propeller’s vertical motion (top), the torque coefficient (center), and the thrust coefficient (bottom) for the Cruise Ship at **$F_n = 0.223$** , **$\lambda_w/L = 0.49$** , **$h_w = 0.1m$** and **$n = 13.57rps$** 143

77 Time histories of the propeller’s vertical motion (top), the torque coefficient (center), and the thrust coefficient (bottom) for the Cruise Ship at **$F_n = 0.223$** , **$\lambda_w/L = 0.98$** , **$h_w = 0.1m$** and **$n = 15.4rps$** 144

78 Time histories of the propeller’s vertical motion (top), the torque coefficient (center) and the thrust coefficient (bottom) for the Containership DTC at **$F_n = 0.087$** , **$\lambda_w/L = 0.44$** , **$h_w = 0.1m$** and **$n = 8.02rps$** 145

79 Time histories of the propeller’s vertical motion (top), the torque coefficient (center) and the thrust coefficient (bottom) for the Containership DTC at **$\lambda_w/L = 0.85$** , **$h_w = 0.1m$** and **$n = 9.05rps$** 146

80 Time histories of wake fraction and thrust deduction for the Cruise Ship at **$F_n = 0.223$** , **$\lambda_w/L = 0.49$** , **$h_w = 0.1m$** and **$n = 13.57rps$** 148

81 Time histories of wake fraction and thrust deduction for the Cruise Ship at **$F_n = 0.223$** , **$\lambda_w/L = 0.98$** , **$h_w = 0.1m$** and **$n = 15.4rps$** 149

82 Computed and measured coefficients of thrust and torque for the Cruise Ship at **$F_n = 0.223$** and the Containership DTC at **$F_n = 0.087$** in regular head waves and calm water 150

| | | |
|----|--|-----|
| 83 | Effective and delivered power for the Cruise Ship at $F_n = 0.223$ and the Containership DTC at $F_n = 0.087$ in regular head waves and calm water | 152 |
| 84 | Propulsive efficiency for the Cruise Ship at $F_n = 0.223$ and the Containership DTC at $F_n = 0.087$ in regular head waves and calm water | 154 |
| 85 | Open water efficiency for the Cruise Ship at $F_n = 0.223$ and the Containership DTC at $F_n = 0.087$ in regular head waves and calm water | 155 |
| 86 | Rotative efficiency for the Cruise Ship at $F_n = 0.223$ and the Containership DTC at $F_n = 0.087$ in regular head waves and calm water | 156 |
| 87 | Hull efficiency for the Cruise Ship at $F_n = 0.223$ and the Containership DTC at $F_n = 0.087$ in regular head waves and calm water | 158 |
| 88 | Thrust deduction factor and wake fraction for the Cruise Ship at $F_n = 0.223$ in regular head waves and calm water | 159 |
| 89 | Thrust deduction factor and wake fraction for the Cruise Ship at $F_n = 0.223$ and the Containership DTC at $F_n = 0.087$ in regular head waves and calm water | 160 |
| 90 | All efficiency for the Cruise Ship at $F_n = 0.223$ and the Containership DTC at $F_n = 0.087$ in regular head waves | 162 |
| 91 | Wave pattern for the free-running Cruise Ship with constant propeller speed at $n = 14.8\text{rps}$ and $\lambda_W/L = 0.89$ | 166 |
| 92 | Numerical grid used for computations of the speed loss in regular and irregular head waves | 167 |
| 93 | Heave and pitch motions for the free-running Cruise Ship in regular head waves with propeller speed at $n = 14.8\text{rps}$ and $\lambda_W/L = 0.98$ | 169 |
| 94 | Propeller thrust (top), torque (middle) and ship speed (bottom) for the Cruise Ship at $n = 14.8\text{rps}$ and $\lambda_W/L = 0.98$ | 170 |
| 95 | Computed and measured speed losses for the Cruise Ship in regular waves | 171 |

List of Figures

96 Wave pattern around the free-running Cruise Ship in irregular waves according to JONSWAP spectrum with $\gamma = 3.3$, $H_S = 0.15m$, and $T_P = 1.33s$, taking engine dynamics into account 173

97 Time histories of the wave elevation, heave and pitch motions for the Cruise Ship in irregular waves according to JONSWAP spectrum with $\gamma = 3.3$, $H_S = 0.15m$, and $T_P = 1.33s$ taking engine dynamics into account 174

98 Propeller speed, torque, and thrust for the Cruise Ship in irregular waves according to JONSWAP spectrum with $\gamma = 3.3$, $H_S = 0.15m$, and $T_P = 1.33s$ taking engine dynamics into account 175

99 Computed speed loss for the Cruise Ship in irregular waves according to JONSWAP spectrum with $\gamma = 3.3$, $H_S = 0.15m$, and $T_P = 1.33s$ taking engine dynamics into account 176

List of Tables

| | | |
|----|---|-----|
| 1 | Main parameters of investigated ships | 43 |
| 2 | Parameters of the rudder and the propellers of the Containership DTC and the Cruise Ship | 46 |
| 3 | Containership DTC at $F_n = 0.218$: Results of the grid study and grid uncertainty, U_G | 50 |
| 4 | Coefficients of the measured and computed propulsion forces for the Cruise Ship and the Containership DTC in calm water | 59 |
| 5 | Speed and wave parameters of the performed computations with the Cruise Ship and the Containership DTC in ship scale . . | 63 |
| 6 | Speed and wave parameters of the performed computations with the Tanker KVLCC2 and the Wigley Hull in ship scale . . . | 64 |
| 7 | Actual and target wave amplitude of short waves computations with the tanker KVLCC2 at $F_n = 0.142$ | 65 |
| 8 | Computed and measured calm water resistance coefficients of all ships | 68 |
| 9 | Containership DTC at $F_n = 0.139$: Influence of local refinements on the computed nominal wake fraction | 117 |
| 10 | Wave parameter and propeller speed in ship scale | 128 |
| 11 | Computed and measured calm water resistance for the Cruise Ship and the Containership DTC determined for propulsion investigation | 132 |
| 12 | Computed and measured wave-added resistance for the Cruise Ship and the Containership DTC determined for propulsion investigation | 133 |
| 13 | Speed and wave parameters of the performed computations . . . | 168 |
| 14 | Engine characteristics used for computations | 172 |

Nomenclature

Acronyms

| | |
|-----------------------|--|
| BEM | Boundary element method |
| BS | Body-fixed coordinate system |
| CD | Central differencing scheme |
| CFD | Computational fluid dynamics |
| <i>CO₂</i> | Carbon dioxide |
| COMET | Continuum mechanics engineering tool |
| CPU | Central processing unit |
| CV | Control volume |
| DOF | Degree of freedom |
| DNS | Direct numerical simulation |
| DTC | Duisburg test case |
| EEDI | Energy efficiency design index |
| FVM | Finite volume method |
| GM | Metacentric height |
| GS | Global coordinate system |
| HSVA | Hamburgische Schiffbau Versuchsanstalt |
| HRIC | High resolution interface capturing scheme |
| IE | Implicit euler time marching scheme |
| IMO | International maritime organization |
| ITTC | International towing tank conference |
| ITTLL | Implicit three time level time marching scheme |
| ISMT | Institut für Schiffstechnik, Meerestechnik und Transportsysteme |
| JONSWAP | Joint north sea wave project |
| KRISO | Korean research institute for ships and offshore; formerly named MOERI |

| | |
|-----------------|---|
| KVLCC | KRISO very large crude oil carrier |
| MARINTEK | Norwegian marine technology research institute |
| MOERI | Maritime and ocean engineering research institute |
| MULES | Multidimensional universal limiter with explicit solution |
| NSG | Navier-Stokes equations |
| OpenFOAM | Open field operation and manipulation |
| PISO | Pressure implicit with splitting of operator |
| RANSE | Reynolds-averaged Navier-Stokes equation |
| RAO | Response amplitude operator |
| SIMPLE | Semi-implicit method for pressure-linked equations |
| SVA | Schiffbau Versuchsanstalt |
| THD | Thrust deduction |
| TEU | Twenty-foot equivalent unit |
| VCG | Vertical center of gravity |
| VOF | Volume of fluid method |

Latin Letters

| | |
|------------|---------------------------------------|
| A_e | Propeller expanded area |
| A_R | Rudder area |
| A_0 | Propeller disc area |
| b | Body forces |
| b_ϕ | Sources/ sinks of ϕ |
| B | Ship breath |
| c | Wave speed |
| c_b | Block coefficient |
| C_F | Non-dimensional frictional resistance |
| C_T | Non-dimensional calm water resistance |
| C_{AW} | Non-dimensional wave-added resistance |
| C_θ | Non-dimensional pitch amplitude |
| C_Z | Non-dimensional heave amplitude |
| D | Propeller diameter |
| $D(\mu)$ | Spreading function |

| | |
|--------------------------|---|
| d | Ship draft |
| F_D | Friction deduction force |
| F_X | Longitudinal force in waves |
| \bar{F}_X | Time-averaged longitudinal force in waves |
| f_e | Encounter frequency |
| Fn | Froude number |
| g | Gravity |
| G | Center of gravity |
| h | Water depth |
| h_R | Rudder height |
| H_W | Wave height |
| I | Unit tensor |
| I_G | Moment of inertia w.r.t to center of gravity |
| J | Propeller advance ratio |
| k | Wave number/ turbulent kinetic energy |
| k_{XX}, k_{YY}, k_{ZZ} | Radius of gyration |
| k_T | Coefficient of the propeller thrust |
| k_Q | Coefficient of the propeller torque behind the ship |
| k_{Q0} | Coefficient of the propeller torque in homogeneous inflow |
| L | Ship length |
| m | Mass |
| M_G | Moments |
| n | Propeller speed |
| n | Normal vector |
| p | Pressure |
| P_E | Effective power |
| P_D | Delivered power |
| P_M | Mean propeller pitch |
| P_T | Thrust power |
| R | Ship resistance |
| R_{AW} | Wave-added resistance |
| Re | Reynolds number |
| R_F | Frictional resistance |

Nomenclature

| | |
|-------------|--|
| Rn | Reynolds stress tensor |
| R_T | Calm Water resistance |
| R_{SEA} | Added resistance due to a seaway |
| $S(\omega)$ | Wave density spectrum |
| S | CV-surface |
| S_W | Ship's wetted surface |
| T | Wave period/ propeller thrust |
| T | Stress tensor |
| T_e | Encounter period |
| T_T | Transformation matrix |
| t | Time/ thrust deduction factor |
| δt | Time step |
| v | Ship velocity |
| v_a | Axial propeller inflow velocity |
| w | Taylor wake fraction |
| Q | Propeller torque |
| Q_0 | Propeller torque at homogeneous inflow |
| V | CV-volume |
| y^+ | Non-dimensional wall distance |
| z | Number of propeller blades |
| Z_a | Heave amplitude |
| x, y, z | Global coordinates |

Greek Letters

| | |
|--------------------|------------------------------------|
| α | Scalar volume fraction |
| Γ | Diffusivity coefficient |
| ε | Dissipation rate |
| ζ | Wave elevation |
| ζ_a | Wave amplitude |
| η_D | Propulsion efficiency |
| η_0 | Propeller efficiency |
| η_H | Hull efficiency |
| η_R | Relative rotativ efficiency |
| θ | Pitch angle |
| θ_a | Pitch amplitude |
| λ | Scaling factor |
| λ_W | Wave length |
| μ | Dynamic viscosity/ encounter angle |
| μ_T | Turbulent viscosity |
| μ_{EFF} | Effective viscosity |
| ν | Kinetic viscosity |
| ρ | Fluid density |
| τ_W | Shear force |
| ϕ | Scalar variable/ heel angle |
| ξ, η, ζ | Body fixed coordinates |
| ψ | Yaw angle |
| ω | Wave frequency |
| $\tilde{\omega}$ | Non-dimensional wave frequency |
| ω_G | Angular velocity |
| Ω | Invariant measure of strain rate |

1 Introduction

The installed power of a ship is generally defined by the contractually agreed design speed. The design speed needs to be proven by the shipyard during sea trials. The environmental conditions that are contractually specified for these sea trials typically represent nearly ideal fair weather conditions: the prevailing wind speed does not exceed two on the Beaufort scale, and the significant wave height of the seaway is stipulated to be less than $0.5m$. There are three principal reasons for why sea trials are performed and why the ship power performance is consequently assessed and optimized under calm water conditions. First, calm water conditions are relatively unambiguous and thus better suited for use in contracts. Second, during sea trials, it is easier to reach an agreement between the owner and shipyard on calm water conditions if the wave height is obtained from weather forecasts or visually observed. Third, power prediction and design optimization based on scale model tests and computations are easier to perform for calm water conditions. However, to ensure that a ship is also capable of reaching its contractual design speed under less favorable operating conditions, a general experience-based 15 percent of reserve power, called “sea margin”, is added to the power required for calm water conditions according to ITTC (2008). An additional 10 percent engine margin accounts for aging of the ship’s hull (caused by fouling) and the installed machinery. To date, this procedure has proven to be suitable for practical applications and has seldom been questioned. This was brought about by the increasing size of modern ships operating at higher service speeds and the associated increased installed power, as well as the available long-term experience with these ships. Thus, ships are equipped with sufficient reserve power for adequate maneuverability in severe seaways. However, the disadvantage of this approach is that a ship is optimized for conditions that it may rarely encounter, and the added reserve power is generally considered to be

independent of ship size or type. This situation may lead to both underpowered smaller ships and overpowered larger ships operating in the same sea areas. Due to increasing operational costs and business competition, ship operators are becoming increasingly motivated to critically scrutinize the fuel consumption of their fleet. Consequently, ships are requested to be designed and optimized for their operational conditions. Therefore, the current design procedures should be challenged and possibly adapted to optimize ships for near-service operational conditions.

Both the economic crisis starting in 2008 and increasing oil prices led the maritime sector to reconsider its planning and to modify the operating profile of their fleets. New concepts were adopted, such as “slow steaming”, which is characterized by the continuous operation of ships at installed power levels that are reduced by 40 percent or more. Subsequently, new builds were ordered, which were designed to operate at 40 to 70 percent of the installed power compared to previous designs. Furthermore, the demand for designs that can be operated at not only one but several power ranges has increased. Consequently, the entire maritime community – ranging from engine manufacturers to logistics companies - is in the process of developing concepts that allow ships to continuously operate at their most efficient and economical operational point by installing reduced power.

It was initially believed that this course of action would be of short duration for the period of high oil prices. However, such concepts are also fueled by eco-political agreements (e.g., the Kyoto Protocol). The International Maritime Organization (IMO) has introduced a new indicator: the Energy Efficiency Design Index (EEDI), see MEPC (2011). The target was to limit CO_2 emissions relative to a ship’s load capacities and the service speed. To achieve the agreed upon reduction of emitted greenhouse gases specified in the Kyoto Protocol, it is necessary to continuously reduce the EEDI. Installing reduced power is an effective way to comply with the reduction of ship-specific EEDI. For ship owners, the present concepts for new builds are likely to remain financially interesting, even with falling fuel prices, because exceeding an EEDI will be penalized in the future. However, the reduced power requirements of new builds with unchanged size raise safety-related concerns, particularly for institutions responsible for ship safety matters, such

as the IMO, flag state administrations, classification societies and insuring companies. Two aspects are mainly of importance: adequate maneuverability (maintaining and changing course) even in heavy seaways and the assumed ship speed (speed loss) in waves as a prerequisite for a global strength analysis of the ship's hull girder. Consequently, selection of the propelling machinery installed on board may be based not only on the desired service speed but also on the required maneuverability in severe seas.

Consequently, due to economic, environmental and safety issues, a ship's performance in operational conditions is of increasing interest in the maritime industry. In addition to the calm water values, a ship's performance in operational conditions is significantly influenced by environmentally caused changes of the resistances (wind, waves, ice, and fouling) and the propulsion characteristics. The flow around ships in waves is very complex, particularly in the vicinity of the operating propeller and the free surface. It is significantly influenced by nonlinearities, such as flow separation, ventilation, wave breaking, and turbulence, among others. Widely used methods to predict ship performance in seaways are based on empirical formulas or on the potential theory. These methods do not cover most of the nonlinearities. In this thesis, advanced numerical methods solving the Reynolds-averaged Navier-Stokes equations (RANS), which best cover the mentioned effects, were used for an extensive and systematic investigation of the influence of waves on the performance of ships, namely the wave-added resistance, the wake field, the propulsion characteristics, and the speed loss in waves. Thus, the basic investigation of nonlinearities related to the performance of ships in waves represents the most substantial research progress by this thesis. The major research questions are:

- How accurate and reliable are RANS methods for predicting wave-added resistance, and how are the results influenced by discretization errors?
- How does ship speed influence the wave-added resistance?
- How does friction affect the wave-added resistance?
- How do the radiation and diffraction forces interact in the nonlinear regime? Can these problems be considered separately?

- How does the wave-added resistance depend on the wave height? Does the quadratic correlation also hold for steep waves?
- How does the encounter angle influence the wave-added resistance in waves?
- How do waves influence the nominal wake fraction of ships?
- How can ship propulsion in waves be reliably and efficiently computed using RANS methods?
- How do waves and ship motion influence the propulsive efficiency of different ship types?
- How do waves and ship motion influence the effective wake fraction and the thrust deduction factor?
- How accurate and effective are RANS methods for determining the speed loss of ships in regular and irregular waves?
- How does the engine dynamic influence the speed loss in irregular waves?

Within this work the research questions are deduced, the numerical methods and computational procedures are presented and the results are discussed to address the research questions. Therefore this thesis is structured as follows: In chapter 2, the theoretical backgrounds on a ship's resistance, the wave-added resistances and propulsion theory are given. Chapter 3 presents the numerical methods used in this work. In chapter 4 the considered ship types, experimental setups and validation work are presented. In chapters 5,6,7 and 8 the computational procedures to determine the wave-added resistance the nominal wake fraction, the propulsion characteristics in waves and the speed loss are explicitly introduced. Furthermore, the results are presented and discussed in these chapters. Chapter 9 provides an overview on the outcomes of this work and possible directions for future work.

2 Theoretical Background and State of the Art

In this work the performance of a ship is evaluated based on economical, ecological, and safe operation. Key aspects in this context are the hydrodynamic characteristics of the hulls itself and its appendages, as well as the interaction among them. Regardless of whether in waves or in calm water, these hydrodynamic properties of a ship are summarized and most commonly evaluated on basis of the propulsive efficiency, η_D . It is defined as the ratio of the effective power, $P_E = R \cdot v$, and the delivered power, $P_D = 2\pi Qn$, required to drive the ship:

$$\eta_D = \frac{P_E}{P_D} = \frac{R \cdot v}{2\pi Qn} \quad (2.1)$$

where R is the towed ship's resistance, v is the ship speed, Q is the propeller torque, and n is the propeller speed. The propulsive efficiency is clearly influenced by resistance as a characteristic of the hull and by the propeller torque as a characteristic of the propeller. However, the flow field that the propeller operates in is changed by the (typically located upstream) hull. The propulsion system in turn changes the flow field at the hull of the ship. Since these complex propeller/ hull interactions are contained in the delivered power, P_D , identifying the efficiency optimization potential of a ship is difficult. The hope is that advanced numerical methods will allow a comprehensive optimization of the ship interacting with the propeller as a whole system in the future. At present, however, ship optimization is performed on the basis of the propulsion characteristics obtained in the traditional propulsion model based on experimental fluid dynamics. The model considers the propeller and ship

separately and introduces special efficiencies and factors to account for the effects of interaction (Bertram, 2000).

In this chapter, the relevant physics of the ship resistance, the propeller/ hull interaction and the evaluation of the ship propulsion characteristics in waves will be presented. In addition, the prediction methods that are available in this field of ship hydrodynamics are introduced and discussed.

2.1 Ship Resistance

Ship resistance, R , is of fundamental importance in ship hydrodynamics. R is one of the values that characterize a ship, and influences nearly all its technical aspects, e.g., hull shape, propulsion components and load capacity. For practical reasons, it is common to split the resistance that a ship experiences under operational conditions into the calm water resistance, R_T , and the added resistances and consider them separately.

The calm water resistance is defined as the longitudinal force that a towed ship experiences under idle conditions without environmental disturbances and without appendages (Krüger, 2004a). Calm water is clearly defined and it is relatively easy to reproduce in test or computations. Thus, the calm water resistance is considered as an important criterion for the ship design. According to the design stage, the calm water conditions can be predicted using empirical methods, numerical methods, and model scale tests.

However, ships face additional resistance components when in service. The added resistances are caused by seaways, wind, shallow water, ice, ship aging and appendages (Krueger, 2004b). For a sea-going ship, in many cases, the added resistances due to seaways, R_{SEA} , is causing the most considerable increase in the ships total resistance. It is defined as the difference of the calm water resistance and the time-averaged longitudinal hydrodynamic force in a seaway.

To illustrate this point, figure 1 shows the total longitudinal force in waves, F_X , the time-averaged longitudinal force in waves, \bar{F}_X , and the calm water resistance. Meanwhile, the total resistance of a ship in a seaway caused by

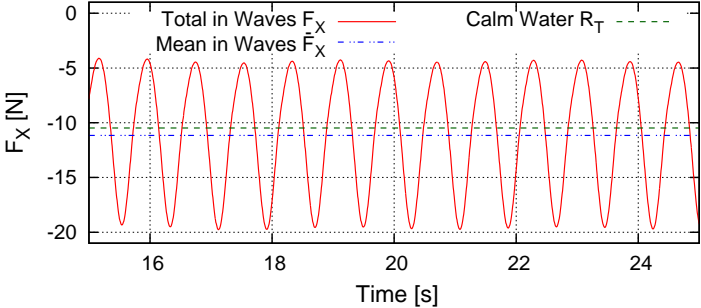


Figure 1: Wave-added resistance of a cruise ship in a regular head waves with a relative length of 1.09 times the ship length - Difference of mean longitudinal force in waves, \bar{F}_X , and calm water resistance, R_T

hydrodynamic forces is defined as the sum of the calm water resistance and the added resistance due to a seaway:

$$R = R_T + R_{SEA} \tag{2.2}$$

Characteristics of seaways are usually provided in a statistical way. Very long physical times of deterministic simulation with randomly realized wave elevations would be required to determine statistical values of ship responses. Time-domain methods that can be used for deterministic simulations are relatively expressive and typically exceeds a reasonable effort. Instead, the seaway is expressed as the superposition of a finite set of regular waves with different heights, phases and periods, represented by a wave energy density spectrum, $S(\omega)$. By knowing the quadratic transfer function of the wave-added resistance, R_{AW}/ζ_a^2 , for every considered regular wave frequency, ω , the added resistance of a ship in a seaway can be determined as follows:

$$R_{SEA} = 2 \int_0^\infty \int_0^{2\pi} \left(\frac{R_{AW}}{\zeta_a^2} \right) (\omega) S(\omega) D(\mu) d\mu d\omega \quad (2.3)$$

where R_{AW} represents the wave-added resistance and ζ_a the wave amplitude. Since seaways are short crested, a spreading function $D(\mu)$ is introduced, which depends on the wave propagation angle μ . Now, the wave-added resistance for a finite number of wave frequencies needs to be predicted only. This significantly reduces the computational effort and allows the use of efficient potential flow methods stated in the frequency-domain. Since this spectral method is frequently used in practical applications, the wave-added resistance is of great interest in ship hydrodynamics.

The wave-added resistance primarily depends on the following:

- ship speed
- ship motion
- hull shape
- wave height
- wave length
- encounter angle.

Especially in steep waves, nonlinearities such as flow separation, ventilation, wave breaking, turbulence, and other viscous effects are occurring. Moreover, common bow shapes together with ship motion and water surface elevation are causing nonlinear changes of the immersed hull area in waves. For this reasons the waves-added resistance is very difficult to predict. In the literature however, the wave-added resistance is considered to be a pressure-dominated phenomenon that is not significantly influenced by viscous effects (Ström-Tejsen et al., 1973). It can be extrapolated from the model scale to the ship scale using Froude similarity. Furthermore, following potential theory, in very flat waves the problem can be linearized and the forces that cause the wave-added resistance can be classified in two separate problems (Soeding, 1982):

- **Excitation forces** act on the fixed hull, and they are caused by incoming waves. These forces can be further divided into Froude-Krylov forces and diffraction forces. Froude-Krylov forces are excited by the hydrostatic pressure caused by elevation of the free surface, including the Smith effect. The diffraction forces are a result of the dynamic effects produced by the wave's orbital velocities.
- **Radiation forces** act on the moving hull in calm water. These forces are caused by a hydrostatic pressure due to the ship's current floating position and a hydrodynamic part as a result of the movement of the ship.

Often, the quadratic transfer function of the wave-added resistance is presented. Here, the non-dimensional wave-added resistance, C_{AW} , is plotted against the non-dimensional wave frequency, $\tilde{\omega}$. The typical characteristics of the quadratic transfer function of the wave-added resistance for different ship types are shown in figure 2. Its maximum is where the wave length is approximately equivalent to the ship length. Here, motion responses are relatively large; thus, the radiation forces are dominating. In shorter waves, the radiation forces decrease along with ship motions. In these areas, the diffraction forces are dominant.

Further information regarding sea-keeping and the wave-added resistance of ships and offshore structures are available in Faltinsen (1998), Journee (2001) and Lloyd and Frina (1998).

As discussed earlier, predicting the wave-added resistance is of high practical interest. Therefore, a considerable amount of research effort has naturally been devoted to this problem. In general, there are experimental, empirical and numerical methods for predicting the wave-added resistance.

In experimental fluid dynamics, model tests are generally performed to predict the wave-added resistance. The model's resistance is measured in calm water and in regular waves of different frequency at the same speed. The differences between calm water resistance and total resistance in the various waves define the wave-added resistance. The challenge is to measure forces without influencing the ship's motion. This measurement is often realized using springs in a rectangular or diamond-shaped frame. Furthermore, the

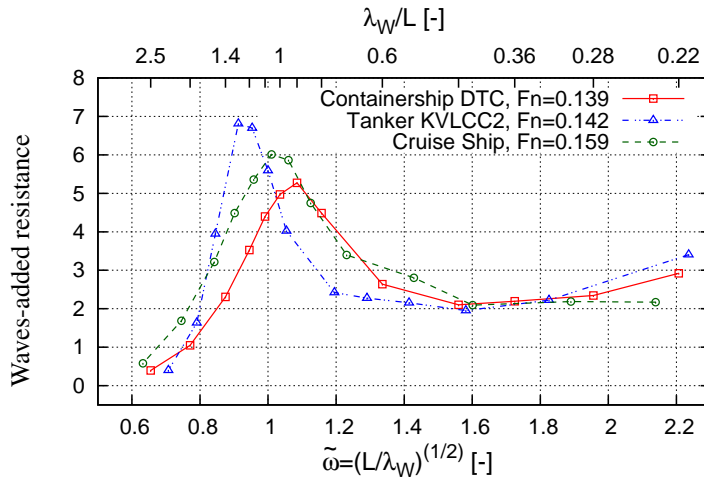


Figure 2: The wave-added resistance for a cruise ship, a containership and a tanker at nearly the same speeds

wave-added resistance is generally small compared to the calm water resistance and the total resistance in waves. Consequently, small measurement errors significantly influence the results. Occasionally, full-scale measurements are also performed. The wave-added resistance is determined based on the measured thrust and ship speed. Here, challenges originate from the unknown influence of waves on the propulsion characteristics. Despite the aforementioned uncertainties, experimental results are the most important reference for validating theoretical methods.

Empirical methods (e.g., Dilk, 2012; Liu et al., 2013; Tsujimoto et al., 2008) allow for an efficient prediction of the wave-added resistance. These methods are based on very few design features (e.g., length, breadth, and flare angle) of the ship only. Thus, these methods are particularly used in early design stages. However, the reliability is limited and depends strongly on the wave conditions and hull shape.

The techniques based on potential theory can be classified into two main categories, namely, far-field methods, which are based on considering the diffracted and radiated wave energy and momentum flux at infinity, and near-field methods, which are based on direct integration of the steady second-order hydrodynamic pressure acting on the wetted ship surface. Maruo (1957) introduced the first far-field approach, which was later extended by Maruo (1960,1963) and Joosen (1966). Boese (1970) developed the first near-field direct pressure integration method, albeit by considering a highly simplified pressure distribution. Gerritsma and Beukelman (1972) introduced the radiated energy approach, which basically followed Maruo's far-field approach. Evaluating the above approaches, Strom-Tejsen et al. (1973) found large discrepancies between the numerical results and comparative model test measurements. Using ship motions obtained from the strip theory of Salvesen et al. (1970), Salvesen (1978) obtained satisfactory predictions by applying Gerritsma and Beukelman's method, thereby confirming the importance of accurate ship motion predictions to reliably estimate added resistance in waves. By introducing a simplified added resistance formula to model the complicated interaction of diffracted waves and the steady flow around the ship, Faltinsen et al. (1980) presented a more accurate potential theory near-field direct pressure integration approach. In this way, they validated their results even for short waves. Recently, Liu et al. (2011) used a well-established frequency-domain panel method and a new hybrid time-domain Rankine source Green function method to predict the added resistance in waves by obtaining first-order velocity potentials and Kochin functions, which are terms that are necessary for computing added resistance according to Maruo's far-field method. They used a wide range of case studies to validate their results and concluded that their method is satisfactory for predicting the added resistance of ships in waves. They recently developed a three-dimensional Rankine panel method that accounts for the interaction of the linear periodic wave-induced flow with the nonlinear steady flow caused by the ship's forward speed in calm water, taking nonlinear free surface conditions and dynamic squat into account (Söding et al., 2012). In this method, added resistance in waves is obtained by pressure integration. Kashiwagi et al. (2010) also investigated the prediction accuracy of added resistance in short

waves when forward speed is present and attributed inaccuracies to hydrodynamic nonlinear effects (Kim and Kim, 2011; Kim et al., 2012; Papanikolaou and Schellin, 1993; Lyu and el Moctar, 2017; Duan and Li, 2013; Guo and Steen, 2011; Kashiwagi et al., 2010; Kuroda et al., 2008; Seo et al., 2013; Seo et al., 2014; Sportelli and Huijsmans, 2012; Turnock et al., 2014; Söding et al., 2014).

Although boundary element methods based on Rankine sources are efficient and therefore predominantly used to screen relevant wave scenarios for design issues, computational fluid dynamics (CFD) methods based on the numerical solution of RANS or Euler equations are increasingly being applied to account for nonlinearities, breaking waves, and so forth. Such methods have demonstrated their ability to provide results with accuracy comparable to model test measurements in many problems of ship hydrodynamics (Larsson et al., 2010; Oberhagemann et al., 2012; el Moctar, 2001; el Moctar et al., 2011, 2016; Schellin and el Moctar, 2007; Carrica et al., 2011). However, the application of such methods to added resistance predictions is still rare. Although such methods might, in principle, also directly address the problem of power increase in irregular waves, both long waves (and the correspondingly large ship motions) and short waves (which contribute to the added resistance through diffraction) should be resolved simultaneously, which significantly increases the required grid size and computational time. Therefore, the application of CFD methods to the added resistance problem has thus far been limited mainly to regular wave situations in a restricted range of wave frequencies (el Moctar et al., 2016; Ley et al., 2014; Sadat-Hosseini et al., 2013; Simonsen et al., 2013).

For a systematic investigation of the wave-added resistance, RANS-based methods have been used in this work. The obtained forces and the motion amplitudes were normalized as follows:

$$C_{AW} = \frac{(\bar{F}_X - R_T) \cdot L}{\rho g B^2 \zeta_a^2} \quad (2.4)$$

$$C_{\theta} = \frac{\theta_a}{k\zeta_a} \quad (2.5)$$

$$C_Z = \frac{Z_a}{\zeta_a} \quad (2.6)$$

where ρ is the density of the water; g is gravity; B is ship breadth; L is ship length; ζ_a and λ_W are wave amplitude and length; Z_a and θ_a are heave and pitch amplitude, respectively; and $k = 2\pi/\lambda_W$ is wave number. For normalization, it is essential to use actual wave amplitudes rather than target values. Therefore, the amplitudes of undisturbed waves next to the ship's bow need to be monitored in all simulations.

The calm water resistance coefficient, C_T , reads:

$$C_T = \frac{R_T}{0.5\rho v^2 S_W} \quad (2.7)$$

where S_W is the wetted surface of the hull.

Because model tests are not suitable for predicting the frictional resistance component for ships, it is common practice to rely on the ITTC 1957 friction line (Hadler, 1958; ITTC, 2008) to specify a ship's frictional resistance coefficient:

$$C_F = \frac{0.075}{\log(Re - 2)^2} \quad (2.8)$$

with the Reynolds number, $Re = v \cdot L/\mu$, where v denotes the ship speed and μ is the kinematic viscosity of water. Frictional resistance, R_F , then reads:

$$R_F = C_F 0.5\rho v^2 S_W \quad (2.9)$$

The response amplitude operators are plotted against the dimensionless wave frequencies defined as follows:

$$\tilde{\omega} = \sqrt{L/\lambda_w} \quad (2.10)$$

2.2 Propeller / Hull Interaction

Propeller / hull interaction is a complex issue and important to take into account when evaluating the propulsive performance of a ship. Propeller / hull interaction is primarily dominated by two effects: the wake and the thrust deduction. In this section, both phenomena will be presented briefly. Detailed information are provided in, e.g., Bertram (2000), Krüger (2004c) and Verhoelt (2001).

2.2.1 Wake Flow

A moving body in water can be idealized as a disturbance of the homogeneous flow. Downstream of the body, the disturbance will be highly developed, and the wake flow establishes. Since its propeller is usually placed in the wake flow area, this phenomenon has great importance for ship design. To evaluate the influence of the wake flow on the propulsion behavior of a ship, the velocity distribution and flow direction in the propeller plane, the wake field, is considered. In calm water conditions the wake field is primarily characterized by three components. The first component is the potential wake, which is the wake field that would be generated in an inviscid fluid. It features small axial velocity components near the stagnation points directly in front of and behind the body. The second component is called wave wake. It is induced by the orbital velocities of the ship's wave system. The third and most important component is the frictional wake. Whereas the first and second effects are typically small, the third component considers the behavior of the flow in the boundary-layer region due to viscous effects. In addition, possible flow separation and the generation of vortices, for example, in the bilge region, contribute to the frictional wake. Consequently, only methods that consider

the viscosity of the fluid are suitable to investigate the wake flow. A more detailed description of the different influences on the wake can be found in Verhoelt (2001).

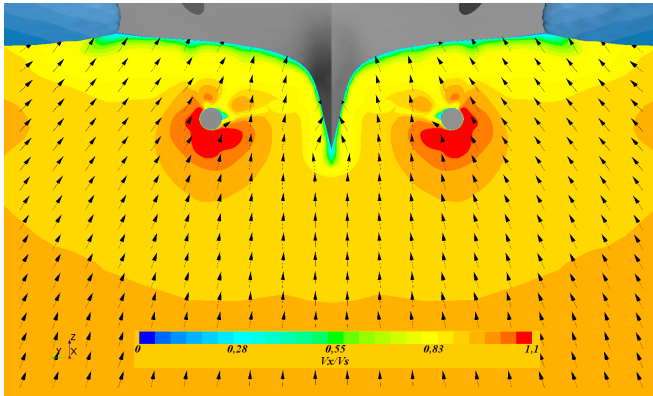


Figure 3: Current effective wake field for a free-running twin-screw cruise ship in waves. The influence of the ship’s hull is clearly visible in the velocity distribution

Figure 3 shows a wake field of a free-running twin-screw ship advancing in waves. The footprint of the hull and its appendages (struts and so forth) can clearly be observed in the vicinity of the stern tube. Generally, the flow in the propeller plane is accelerated by the operating propeller. In particular, in regions close to the ship’s surface, large velocity losses can be observed. This figure is obtained from the RANS computation with a cruise ship that will be discussed later.

As previously mentioned, the wake field of a ship significantly influences the behavior of the propeller (typically located behind the ship). This issue is generally quantified using the wake fraction, which is defined as the ratio of the mean propeller inflow velocity, v_a , and the ship’s velocity, v .

The wake fraction reads as follows:

$$w = 1 - \frac{v_a}{v} \quad (2.11)$$

There are two different ways to determine the mean axial velocity in the propeller plane and thus the wake fraction:

- **Effective wake fraction** is obtained with the operating propeller. v_a in the propeller plane is obtained by comparing the propeller characteristics behind the ship (propulsion test) and in the homogeneous inflow (propeller open water test).
- **Nominal wake fraction** is obtained without a propeller. The mean axial velocity in the propeller plane is obtained by averaging the computed or measured axial velocities at discrete points within the propeller plane determined in a towing test.

The nominal wake is an important input for the design of wake-adapted propellers and is the subject of many design optimization studies, such as the propeller example presented in Stück et al. (2011) and Fahrbach (2004). Thus, the pitch of the propeller blade at different radii is specified based on the wake field. Tangential variations of the inflow velocity cause oscillations of propeller forces and propeller cavitation, which may result in ship vibration and structural damage.

2.2.2 Thrust Deduction

The propeller thrust required to drive a ship at a constant speed is significantly higher than the resistance of the towed ship at the same speed. This increase in the ship's resistance is called thrust deduction and is caused by the propeller-induced acceleration of the flow at aft ship, which influences the pressure distribution on the hull.

For the propulsion condition of a ship, this leads to:

$$T = R + THD \quad (2.12)$$

where T is propeller thrust and THD is the trust deduction. Thrust deduction is generally presented as the non-dimensional thrust deduction factor, t , and it reads as follows:

$$t = 1 - \frac{R}{T}. \quad (2.13)$$

Both wake fraction and thrust deduction factor depend on the velocity field in the aft ship region. It is obvious that the velocity field is significantly influenced by the orbital velocities of incident waves and also by velocity components induced by ship motions in operational condition. However, during ship design, typically the wake field and thrust deduction are considered only under calm water conditions and less is currently known about the influence of waves on the propeller/ hull interaction. Only a few investigations using numerical methods have been performed to address this issue (e.g., Wu et al. 2012, 2013) and only the nominal wake fraction is considered. Investigations on the influence of waves on the effective wake fraction or on the thrust deduction factor are not known to the author.

2.3 Propulsion Characteristics

To determine the propulsion characteristics, the resistance of the towed ship, propeller open water characteristics and propulsion forces are needed. Brief descriptions of the necessary experiments, the associated computations and the calculation of the propulsion characteristics are given in this section.

The propeller open water characteristics are determined by running the propeller in undisturbed inflow conditions at different propeller advance ratios, $J = v_a/nD$. For this purpose, propellers of diameter D are tested for constant propeller speed, n , whereby the propeller inflow axial velocity, v_a , is varied. Propeller thrust, T , and torque, Q_0 , are measured and normalized as follows:

$$k_T = \frac{T}{\rho D^4 n^2} \quad (2.14)$$

$$k_{Q0} = \frac{Q_0}{\rho D^5 n^2} \quad (2.15)$$

$$\eta_0 = \frac{J}{2\pi} \cdot \frac{k_T}{k_{Q0}} \quad (2.16)$$

where k_T is the thrust and k_Q the torque coefficient. Index 0 indicates open water conditions.

The ship resistance is evaluated in the towing test. The bare hull is towed by a carriage at a constant speed. The forces required to tow the model are measured. The result is the ship resistance as a function of ship speed.

In the propulsion test, the model is equipped with propulsion components and it is self-propelled. The results are the propeller thrust and the propeller torque according to the propeller speed required to drive the model at a predefined speed. Friction deduction, F_D , needs to be applied to account for scaling effects shifting the operating point of the propeller. It is defined as:

$$F_D = (C_{T,M} - C_{T,S}) \frac{1}{2} \rho v_M^2 S_{w,M} \quad (2.17)$$

Here, indices M and S denote model scale and full scale, respectively. To apply friction deduction force during experiments, two methods are common: the British method and the continental method (Bertram, 2000). Following the continental method, the friction reduction force is applied, and the propeller speed is adjusted until the target speed is achieved. Following the British method, two runs with different propeller speeds per considered ship speed are conducted. For every run, the propeller speed is constant. The remaining forces are measured at the towing carriage. At the self-propulsion

point of the model, corresponding to full scale, the residual force equals the predefined friction deduction force. The propeller speed, force and moment are determined by performing interpolation. Both methods are used in practice.

As mentioned above, the propulsive efficiency is defined as the ratio of the effective power and the delivered power:

$$\eta_D = \frac{P_E}{P_D} = \frac{Rv}{2\pi Qn} \quad (2.18)$$

The propulsive efficiency of a ship is a very complex and sensitive construct that depends on multiple effects caused by different physical phenomena. To prove the physical consistency of computationally or experimentally obtained results and to identify optimization potential, the propulsive efficiency is split into partial efficiencies. Therefore, equation 2.18 is extended by $\frac{Q_0}{Q}$ and rearranged as follows:

$$\eta_D = \frac{P_E}{P_D} = \frac{T v_a}{2\pi Q_0 n} \frac{Q_0}{Q} \frac{(1-t)}{(1-w)} = \eta_0 \eta_R \eta_H \quad (2.19)$$

The propeller open water efficiency, η_0 , provides the ratio of the thrust power, P_T , and the delivered power:

$$\eta_0 = \frac{P_T}{P_D} = \frac{T v_a}{2\pi Q_0 n} \quad (2.20)$$

The propeller thrust is obtained from the propulsion test and is used to determine v_a and Q_0 from the propeller open water characteristics (thrust identity). Consequently, η_0 is the open water efficiency according to the thrust obtained under self-propelled conditions. It provides information about the general suitability of the chosen propeller to propel the ship. Typically, it ranges from 0.65 to 0.75.

The relative rotative efficiency, η_R , is defined as the ratio of the propeller torque in open water and in self-propelled conditions:

$$\eta_R = \frac{Q_0}{Q} \quad (2.21)$$

This parameter provides information about the influence of the wake field on the propeller torque. Typical values range from 1.0 to 1.05.

The hull efficiency, η_H , is defined as the ratio of effective power and thrust power, and sets thrust deduction factor, $t = 1 - R_T/T$, and wake fraction, $w = 1 - JnD/v$, in relation. It reads as follows:

$$\eta_H = P_E/P_T = \frac{(1-t)}{(1-w)} \quad (2.22)$$

The hull efficiency evaluates the propeller/ hull interaction and can reach values of greater than one. The wake fraction is generally calculated using thrust identity, which means that v_a is obtained from the propeller curves using k_T (rather than k_Q) as an input value.

This experimental procedure has been developed in test facility and is predominantly used for calm water. Experiments are reliable and considered to be a reference for other methods. However, they are very expensive, and only a limited number of design variations can be investigated without the need for a new model. Furthermore, it is not possible to investigate the system holistically. Obtaining details about small-scale flow conditions, such as flow separation, is extremely expensive or simply not possible.

Till now the influence of the seaway on the propulsion characteristics has been barely investigated explicitly. However, experimental procedures for required power in waves have been developed at different institutions (e.g. ITTC 2012, 2014, Kitagawa et al., 2014). Presumably, due to the added resistance in waves, this influence only shifts the operation point of the propeller. However, propulsion is decisively affected by the velocity distribution in the propeller plane, and this distribution in turn is influenced by not only the seaway-induced ship motions, but also the orbital wave particle velocities.

Propulsion tests in waves at the propeller's operating point are difficult to conduct because implementing a speed-dependent frictional deduction is difficult. Moreover, measuring the propeller's wake in a seaway is complex and thus difficult to perform. Techniques based on potential theory may be inappropriate due to the associated frictionless and irrotational flow assumptions. In contrast, approaches based on solving the Navier-Stokes equations represent a good approximation of the physical flow conditions. To date, such approaches have mainly been used to compute a ship's resistance in calm water, where for the case of calm water propulsion, the geometric modeling of the rotating propeller is generally dispensed with. Rather, so-called body force methods are widely used. Such methods vary from a simple preset distribution of propulsion forces in the propeller plane (e.g., Choi et al., 2010; el Moc-tar, 2001; Winden et al., 2014) to coupling a boundary element method with a RANS solver (e.g., Cura-Hochbaum and Vogt, 2008; Krasilnikov, 2013). Using body force methods leads to a significant savings of computational time; nevertheless, such methods impose limits in mapping the physical flow, and they are also subject to uncertainties. To date, RANS computations of propulsion based on the geometric modeling of a rotating propeller (using sliding or overset grid techniques) have mainly been performed by neglecting the free surface or under calm water conditions (e.g., Lübke, 2005; Carrica, et al., 2010, 2011) for a specified propeller rate and a given ship speed. The results from these investigations often showed good agreement with measurements. However, numerical studies of propulsion characteristics for ships in waves based on solving the Navier-Stokes equations are rarely found in the literature.

Although CFD offers completely different strategies to evaluate and optimize ship propulsion, in this work, the presented classical experimental-based procedure was used to determine the propulsion characteristics in waves. Rather than using calm water values of resistance and propeller forces in self-propelled conditions, average values (Fourier analysis) obtained in waves are used (except for propeller open water characteristics). For this, the hull, the rotating propeller using the sliding grid technique, and the rudder were geometrically modeled and the free surface was taken into account in all compu-

tations. The computations were conducted at model scale and compared to model test measurements.

3 Numerical Methods

The Navier-Stokes equations (NSG) and the mass conservation equation are the mathematical foundation of the numerical methods used, since they provide a description of the flow of Newtonian fluids. Due to high Reynolds numbers and consequently fully turbulent flows, NSG are Reynolds-averaged and turbulence models are applied to reduce the numerical effort. An interface-capturing method is used to model two-phase flow. The governing equations are implicitly coupled with a 6-degree of freedom (DOF) rigid body equation in combination with various grid techniques to account for ship motion. The obtained system of non-linear partial differential equations cannot be solved analytically. Thus, the equations are spatially and temporally discretized using second-order schemes and linearized by applying Picard iteration. Then, the equations are solved iteratively in a segregated procedure, coupling pressure and velocity semi-implicitly.

The fundamentals of the governing equations and of the methods and procedures used are presented in this chapter. More details are available in Ferizger and Peric (2002), Muzafferija and Peric (1999) and el Moctar et al. (2016).

3.1 Governing Equations

Since the finite volume method (FVM) for discretization is used, the governing equations are presented in integral form (Hirt, 1981). For an isothermal, viscous, turbulent flow of an incompressible fluid, mass conservation, $\frac{d}{dt}m = 0$, and momentum conservation, $\frac{d}{dt}(m\mathbf{v}) = \sum F$, can be expressed as follows:

$$\frac{\partial}{\partial t} \int_V \rho dV + \int_S \mathbf{v} \cdot \mathbf{n} dS = 0 \quad (3.1)$$

$$\frac{\partial}{\partial t} \int_V \rho \mathbf{v} dV + \int_S \rho \mathbf{v} \mathbf{v} \cdot \mathbf{n} dS = \int_S \mathbf{T} \cdot \mathbf{n} dS + \int_V \rho \mathbf{b} dV \quad (3.2)$$

Here, V denotes a control volume (CV) bounded by its surface, S , and with the normal vector, \mathbf{n} , pointing outward. Body forces are denoted as \mathbf{b} , and fluid density is indicated by ρ . \mathbf{v} represents the velocity vector.

With the unit tensor, \mathbf{I} , pressure, p , and the dynamic viscosity, μ , the stress tensor, \mathbf{T} , reads as follows:

$$\mathbf{T} = -p\mathbf{I} + \mu[\nabla\mathbf{v} + (\nabla\mathbf{v})^T] \quad (3.3)$$

For typical Reynolds numbers in marine applications ($Re \gg 10^6$), direct numerical solution (DNS) is not yet applicable. Due to small turbulent vortex structures that need to be resolved spatially and temporally, the computational effort is far too high for practical use. To overcome this issue, different approaches to model turbulence were developed. These approaches differ in computational effort depending on the rate of physical correctness. In marine applications, turbulence models based on Reynolds-averaging of the Navier-Stokes equations are widely used. Here, the flow variables in Equations (24) and (25) are decomposed into an average value, $\bar{\phi}$, and a turbulent fluctuation, ϕ' :

$$\phi(x, t) = \bar{\phi}(x, t) + \phi'(x, t) \quad (3.4)$$

The averaging takes place over a time interval, T , which is much longer than the time scale of the turbulent fluctuations, but shorter than the time scale of non-turbulent flow unsteadiness (e.g. blade passing period):

$$\lim_{T \rightarrow \infty} \frac{1}{T} \int_T \phi(x, t) dT = \bar{\phi}(x) \quad \lim_{T \rightarrow \infty} \frac{1}{T} \int_T \phi'(x) dT = 0 \quad (3.5)$$

By time averaging of the equations, the fluctuation disappears in the linear terms. The non-linear convection term yields an additional term, the Reynolds stress tensor, \mathbf{Rn} , which contains another six unknowns:

$$\mathbf{Rn} = -\rho(\overline{\mathbf{v}'\mathbf{v}'}) \quad (3.6)$$

Now, NSGs are expressed for Reynolds-averaged flow quantities.

The eddy viscosity assumption of Boussinesq (1877), stating that the effects of \mathbf{Rn} can be modeled as additional diffusion, is basis of all two equation turbulence models and introduces the effective dynamic viscosity, μ_{EFF} . The effect dynamic viscosity is defined as the sum of dynamic viscosity, μ , and turbulent viscosity, μ_T :

$$\mu_{EFF} = \mu + \mu_T \quad (3.7)$$

The turbulent viscosity is determined based on velocity and length scale, v_T and l_T , of the turbulence:

$$\mu_T \approx \rho v_T l_T \quad (3.8)$$

The velocity scale is usually taken corresponding to the square root of the turbulent kinetic energy, $k = 1/2 \overline{u_i u_i}$. The turbulent kinetic energy is obtained by solving a transport equation first. In the two equation turbulence models, the length scale is obtained from relations involving k and either the turbulent dissipation rate ε or the specific turbulent dissipation, ω , e.g. $l_T \approx k^{3/2}/\varepsilon$, leading to:

$$\mu_T \approx C_P \rho \frac{k^2}{\varepsilon} \quad (3.9)$$

Using these turbulence models additional transport equations are solved to obtain ω or ε .

In this work, Menter's shear stress transport (SST) $k - \omega$ turbulence model is used predominately (Menter, 1994). It combines the $k - \omega$ and the $k - \varepsilon$ model. The turbulent viscosity is determined with the turbulent kinetic energy, k , and the specific turbulent dissipation, ω , as

$$\mu_T = \frac{a_1 k}{\max(a_1 \omega, \Omega F_2)} \quad (3.10)$$

where a_1 is the closure coefficient, Ω is the invariant measure of strain rate, and F_2 is the formulation for the blending from $k - \omega$ to $k - \varepsilon$. The scalar quantities k and ω/ε of the model have to be transported. The transport equation for generic scalar quantities reads as follows:

$$\frac{\partial}{\partial t} \int_V \rho \phi dV + \int_S \rho \phi \mathbf{v} \cdot \mathbf{n} dS = \int_S \Gamma \nabla \phi \cdot \mathbf{n} dS + \int_V \rho \mathbf{b}_\phi dV \quad (3.11)$$

where ϕ is the scalar variable (k or ω), Γ is the diffusivity coefficient, and \mathbf{b}_ϕ represents sources or sinks of ϕ . For details about source terms and model parameters, see Menter (1994). the Turbulent viscosity varies within solution domain by several orders of magnitude and makes the system of equations that needs to be solved highly non-linear.

3.2 Free Surface Treatment

To model two-phase flows, the Volume of Fluid method (VOF) is used. For the entire computational domain, only one velocity and pressure field exists. A fluid is considered to consist of two phases, namely, water and air. The

distribution of water within the domain is defined by the volume fraction scalar α , which represents the water fraction in every CV. The value of α is computed using an additional scalar transport equation:

$$\frac{\partial}{\partial t} \int_V \alpha dV + \int_S \alpha \mathbf{v} \cdot \mathbf{n} dS = 0 \quad (3.12)$$

The density, ρ , and viscosity, ν , of fluids within each cell are then determined as follows:

$$\rho = \sum_i \rho_i \alpha_i \quad (3.13)$$

$$\nu = \sum_i \nu_i \alpha_i \quad (3.14)$$

The VOF approach has proven to be suitable to account for complex free surface phenomena, such as wave breaking and overturning waves. However, the position of the free surface cannot be computed explicitly. Rather, the water surface needs to be reconstructed from the α field by interpolation. The free surface is assumed to be located where α equals 0.5. To avoid smearing of the free surface and nonphysical fluid properties, the values of α need to be bounded ($0 \leq \alpha \leq 1$), and cells with $0 < \alpha < 1$ need to be minimized. To satisfy these requirements, special numerical schemes were used to discretize the α transport equation (see the next section).

3.3 Discretization

The conservation equations cannot be solved analytically. Thus, these equations are transformed into algebraic equations and solved numerically. Using the finite volume method, the fluid domain is subdivided into a finite number of control volumes, which contain flow variables in their center. For each CV, an algebraic equation is set up using a finite approximation for volume and surface integrals and for spatial and temporal derivatives. Integrals are

approximated using the midpoint rule in combination with 2nd-order interpolation schemes. Derivatives are estimated using finite differences based on a Taylor polynomial. Generally, temporal derivatives are approximated using *Crank-Nicolson* or *implicit three time level time marching scheme*. When possible, all approximations are of second-order accuracy. The first order *Euler implicit* scheme is only used marching toward steady-state solution, when the flow development does not have to be time accurate. In rare cases, the discretization schemes for convection were changed to first-order upwind differences for stability reasons. Special discretization schemes were used for the α -transport equation to guarantee a sharp water surface during the computation. Here, schemes blending between central, upwind and downwind differences were used; see Muzaferija and Peric (1999) for more details on the HRIC-scheme (high-resolution interface capturing).

3.4 Velocity-Pressure Coupling

To obtain a consistent solution of velocity and pressure, both conversation equations (24) and (25) need to be fulfilled simultaneously. Since it is not possible to compute all equations simultaneously, they are solved using projection methods coupled in a semi-implicit manner. First, the velocity field is computed using linearized momentum equations and the pressure field of the previous time step or iteration. Then, the pressure-correction equation is solved, which is derived from the discretized momentum and mass conservation equations. Subsequently, the velocity and pressure fields are corrected using the pressure-correction field. Various algorithms, e.g., SIMPLE, PISO, and PIMPLE, based on this concept are available in the software used in this work. In general, these algorithms vary in the way that the pressure-correction equation is set up and the velocity field is corrected. Here, the SIMPLE algorithm is most often used to couple pressure and velocity. The major steps of SIMPLE are summarized as follows:

- Solve iteratively the linearized momentum equations using the latest pressure and velocity fields to estimate a provisional velocity field, v^{m*} , which does not satisfy the continuity equation (inner iterations)
- Solve the pressure-correction equation to obtain p' ($p^m = p^{m-1} + p'$)
- Correct the velocity and pressure field to satisfy the continuity equation, getting v^m and p^m
- Repeat the procedure using v^m and p^m as improved starting estimation until the convergence criteria are satisfied, this completes the outer iteration loop
- Advance to the next time step

The SIMPLE algorithm is widely used in marine applications. However, the SIMPLE algorithm involves approximations which may introduce instability. This problem is solved by under relaxing the pressure and velocity fields. The following convergence criteria are usually used:

- When solving the linearized equation system (inner iteration), residuals are reduced by one order of magnitude
- Outer iterations are continued until residuals are reduced by three orders of magnitude

For more details on SIMPLE and related , see Ferziger and Peric (2002).

3.5 Modeling of Waves

Waves are specified at inlet using an appropriate boundary condition. In most cases , Stokes 5th order wave theory after Fenton (1985) is used to prescribe regular waves. For irregular long-crested waves, the Jonswap spectrum is used. From these wave theories, the variation of the velocity and volume fraction at the inlet boundary over time is prescribed. In order to avoid wave

reflection from outlet boundary, wave damping is used; that is achieved by using source term in the momentum equation which forces the vertical velocity component to zero over certain distance from boundary. For optimal setup of the wave damping, see Peric and Abdel-Maksoud (2017).

3.6 Ship Motion

For the computation of the ship motion, a rigid body motion solver for 6-DOF is implicitly coupled with the governing equations. Flow forces and moments are present in the global coordinate system (**GS**). However, the inertia matrix of the ship is constant only in the body-fixed coordinate system (**BS**), which moves with the ship. Thus, the inertia matrix needs to be transformed in every time step from **BS** to **GS**. The relative orientation of **BS** in **GS** is expressed using the Euler angle. After determining ship motions, the numerical grid constantly needs to adapt to the new ship position.

In this section, Euler angle, the rigid body motion equation and the common grid techniques are presented. Detailed information is available in Brunswik and el Moctar (2004), Oberhagemann (2016), Ferziger and Peric (2002).

3.6.1 Euler Angle

The orientation of any reference frame relative to another can be defined by three angles. These Euler angles are consecutive rotations about the x-y-z axes. Thus, the order of rotation does not commute. Consequently, the sequence of rotations needs to be fixed. A common convention is to perform x-y-z rotations. The cycle of such a rotation sequence, often also denoted as rotation, is shown in figure 4 and consists of the following steps:

- The starting coordinate system is x, y, z . Rotation ψ about Z carries the axis to the intermediate position x^*, y^*, z . ψ is called the azimuth or yaw angle.
- From x^*, y^*, z , rotation θ about y^* further carries the axis to ξ, y^*, z^* . θ is the elevation or pitch angle.

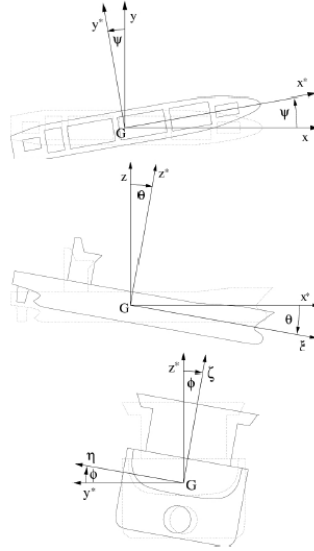


Figure 4: Sequence of rotations of yaw, pitch and roll (top to bottom); here, (ξ, η, ζ) are ship fixed and (x, y, z) are global coordinates. G denotes ζ_0 , the origin of the body fixed coordinate system, (Brunswick, 2004).

- Finally, from ξ, y^*, z^* , rotation ϕ about ξ carries the axis to the final position ξ, η, ζ . ϕ is the bank or heel angle.

This rotation sequence can be combined in the transformation matrix \mathbf{T}_T from **BS** to **GS** as a series of subsequent principle rotation matrices as follows:

$$\mathbf{T}_T = \begin{pmatrix} \cos\psi & -\sin\psi & 0 \\ \sin\psi & \cos\psi & 0 \\ 0 & 0 & 1 \end{pmatrix} \cdot \begin{pmatrix} \cos\theta & 0 & \sin\theta \\ 0 & 1 & 0 \\ -\sin\theta & 0 & \cos\theta \end{pmatrix} \cdot \begin{pmatrix} 1 & 0 & 0 \\ 0 & \cos\phi & -\sin\phi \\ 0 & \sin\phi & \cos\phi \end{pmatrix} \quad (3.15)$$

Note that to express \mathbf{T}_T in terms of the Euler angles, the sequence of rotation has to be reversed. Since the product of any number of rotation matrices is itself a rotation matrix, this yields the following:

$$\mathbf{T}_T = \begin{pmatrix} \cos\theta\cos\psi & \sin\phi\sin\theta\cos\psi - \cos\phi\sin\psi & \cos\phi\sin\theta\cos\psi + \sin\phi\sin\psi \\ \cos\theta\sin\psi & \sin\phi\sin\theta\sin\psi + \cos\phi\sin\psi & \cos\phi\sin\theta\cos\psi - \sin\phi\sin\psi \\ -\sin\theta & \sin\phi\cos\theta & \cos\phi\cos\theta \end{pmatrix} \quad (3.16)$$

3.6.2 Rigid Body Motion Equations

Translation and rotation of the rigid body in 6 DOF is determined by integrating the equation of linear and angular momentum. The equation for the variation of linear momentum with respect to the center of gravity reads as follows:

$$\frac{d}{dt}(m\mathbf{v}_G) = \mathbf{F} \quad (3.17)$$

where m is the mass of the investigated body, \mathbf{v}_G represents the linear velocity of the center of gravity, \mathbf{G} , and \mathbf{F} is the resulting force acting on the body. With constant mass, Eq. (45) may be written as follows:

$$m\dot{\mathbf{v}}_G = \mathbf{F} \quad (3.18)$$

where $\dot{\mathbf{v}}_G$ is the total linear acceleration of the center of gravity in the \mathbf{GS} reference frame. The equation for the angular momentum with respect to the center of gravity in \mathbf{BS} reads as follows:

$$\frac{d}{dt}(\mathbf{I}_G\omega_G) = \mathbf{M}_G \quad (3.19)$$

where ω_G represents the angular velocity of the rigid body and \mathbf{M}_G is the resulting moment acting on the body, all with respect to \mathbf{G} . \mathbf{I}_G is the tensor of the moment of inertia of the investigated body with respect to \mathbf{BS} .

$$\mathbf{I}_G = \begin{pmatrix} I_{xxG} & -I_{xyG} & -I_{xzG} \\ -I_{yxG} & I_{yyG} & I_{yzG} \\ -I_{zxG} & -I_{zyG} & -I_{zzG} \end{pmatrix} \quad (3.20)$$

With constant mass and moments of inertia of the rigid body with respect to \mathbf{BS} , eq. (47) may be rewritten as follows:

$$\frac{d}{dt}(\mathbf{I}_G \omega_G) = \mathbf{I}_G \dot{\omega}_G + \omega_G \times \mathbf{I}_G \omega_G = \mathbf{M}_G. \quad (3.21)$$

When expressing the tensor of the moments of inertia with respect to the center of mass expressed in the GS reference system, it changes with every rotation motion of the body. The equations for transforming linear and angular momentum in GS may be written as follows:

$$m\dot{\mathbf{v}}_G^{GS} = \mathbf{F}^{GS} \quad \mathbf{T}_T \mathbf{I}_G \mathbf{T}_T^{-1} \dot{\omega}_G^{GS} + \omega_G^{GS} \times \mathbf{T}_T \mathbf{I}_G \mathbf{T}_T^{-1} \omega_G^{GS} = \mathbf{M}_G^{GS} \quad (3.22)$$

where \mathbf{T}_T is the transformation matrix from the \mathbf{BS} to \mathbf{GS} reference system. This equation implies that the tensor moment of inertia of the body with respect to the GS , \mathbf{I}_G^{GS} is not constant. It changes with the motion of the body and therefore has to be updated every time that the body changes position. The columns of the matrix \mathbf{T}_T are the unit vectors $\mathbf{x}, \mathbf{y}, \mathbf{z}$ expressed in the \mathbf{GS} system attached to the \mathbf{BS} system.

3.6.3 Grid Techniques

Different grid techniques are available to move the ship within the numerical domain and to perform the movement of appendages such as the propeller or rudder. It is important to know the abilities and limits of such techniques

to choose the most suitable one corresponding to the specific flow problem. Often, grids need to be adapted to the grid technique. The most common techniques are as follows:

- Mesh moving
- Mesh morphing
- Sliding grid
- Overlapping grid

In this chapter, the basic principals of these grid techniques are presented. The abilities, benefits and drawbacks of these techniques are briefly discussed.

Mesh Moving When using the mesh moving technique, the entire grid is kept rigid, and the whole grid is moved coupled with the ship's motion. In general, this technique is robust, and the computational effort is relatively small. However, large ship rotation in combination with large fluid domains (used to avoid wave reflection) lead to large relative motion between the water surface and the numerical grid. Consequently, the free surface needs to be smoothly resolved in a wide range of the numerical grid to avoid interpolation errors. This requires immense manual efforts and significantly larger cell numbers. Furthermore, the method is only applicable for the motion of one body. Simulating the interaction of multiple bodies is not possible. Nevertheless, particularly for the propulsion computation in moderate wave heights and with relatively small motion angles in combination with the sliding grid technique for propeller rotation, the mesh moving technique delivers good results with relatively low effort. A moving grid surrounding a cruise ship in regular waves is shown in figure 5.

Mesh Morphing The mesh morphing technique allows some boundaries (here, the ship) of the grid to move, whereas others are fixed (far-field boundaries). Ship motions are performed by deforming cells in between. The advantage of this method is that only a portion of the grid has to be highly

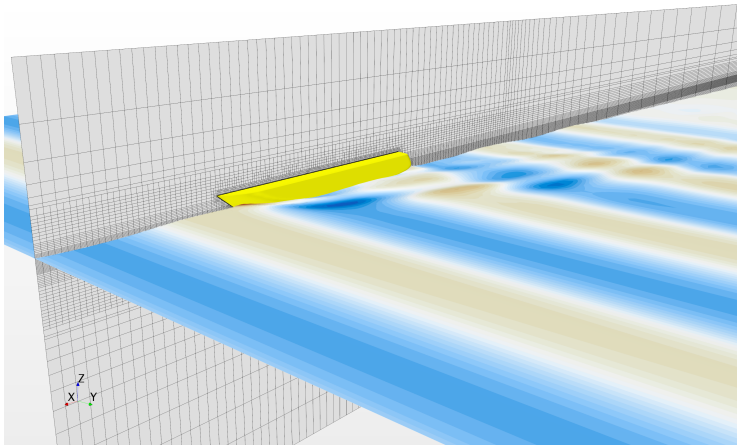


Figure 5: *Computation of the wave-added resistance for a cruise ship in head waves using the mesh moving technique at $\mathbf{Fn} = 0.223$, $\lambda_{\mathbf{W}}/\mathbf{L} = 0.98$ and $\mathbf{h}_{\mathbf{W}} = 3.6m$*

refined, whereas in the far-field, the higher resolution is only necessary in the vicinity of the fixed free surface interface, see figure 6.

Maintaining mesh quality is challenging especially for large rotation angles. Oberhagemann (2004, 2007) introduced a fast and robust grid morphing approach. The criterion on grid quality is explicitly enforced; therefore, this morphing approach has no inherent mechanism to preserve grid quality. Roll angles of more than 60° can easily be realized without producing degenerated volumes (Oberhagemann, 2016). Most of the added resistance computations were performed using this method.

Sliding Grid Within the sliding grid technique, a rotating grid region, e.g., around a ship's hull or propeller, and a non-rotating grid region are connected via a sliding interface. Translations are fulfilled by both regions. The exchange of flow variables is performed by interpolation, which significantly increases the computational effort. However, a great benefit of this technique

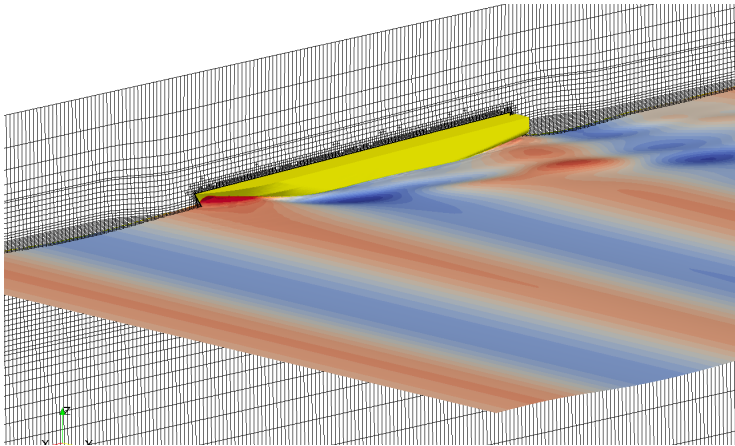


Figure 6: *Computation of the wave-added resistance for a containership in head waves using the mesh morphing technique at $\mathbf{Fn} = 0.218$, $\lambda_{\mathbf{W}}/\mathbf{L} = 1.125$ and $\mathbf{h}_{\mathbf{W}} = 6\mathbf{m}$*

is the opportunity to model relative rotation between grid regions of more than 180° . Therefore, the sliding grid technique is used to enable turning of the geometrically modeled propeller in propulsion computations and performing turning circle maneuvers in waves. Figure 7 shows a computation of a free-running turning circle of a containership in waves. Propeller and ship rotations are realized using the sliding grid technique. Ship translations are performed using the mesh moving technique.

Overlapping Grid The background grid, overlapped by the overset grid around the moving body, is employed using the overlapping grid technique. The overset grid is allowed to move freely within the background grid. Control volumes within the overlapped region in the background grid are set as inactive, and transfer cells (donor / acceptor cells) between background and overset grids are identified. Flow variables are interpolated from donor cells to the acceptor cells. The overlapping grid technique offers nearly unre-

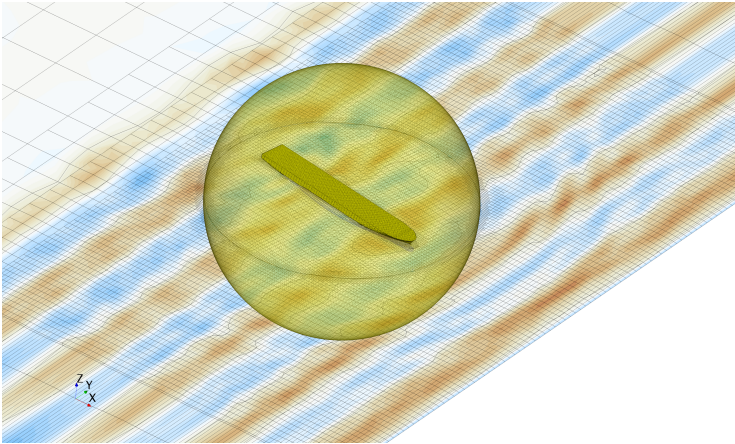


Figure 7: *Computation of a free-running turning circle for a containership using sliding grid in combination with the mesh moving grid technique at $\mathbf{Fn} = 0.139$, $\lambda_w/L = 0.85$, $h_w = 3.8m$ and $n = 10rps$*

stricted movement of multiple bodies; however, it comes with some disadvantages inherent to the method. The most important is that mass conservation across the overlapping zone is not guaranteed. Furthermore, the necessary determination of donor and acceptor cells and the interpolation between them adds a significant amount of computational effort to the simulation. Due to these significant disadvantages and uncertainties, the overlapping grid technique is not used in the present work.

3.7 Computational Procedure

In general, the procedure presented in figure 8 is used to couple rigid body motion solver with the RANS equation. Within one outer iteration, initially the new velocity and pressure field as well as fields of the volume fraction and turbulence parameters are computed (inner iteration). With the obtained flow forces, the position of the floating body is determined and the grid is

accordingly updated. This sequence is repeated till convergence is achieved and the procedure starts for the next time step.

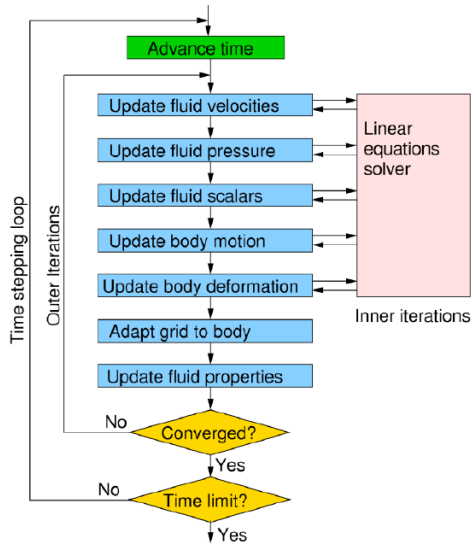


Figure 8: Schematic solution procedure of the employed numerical methods, (Peric and Schreck, 2009)

The residuals for the inner iterations were set to 10^{-3} with a limit of 1000 for each equation. For transient computations, the outer iterations were set to 5-10 per time step, depending on the specific case. In general, very small time steps of $\max \delta t = 0.005$ seconds were used; when modeling the operating propeller, the time step was even smaller. Computations were performed on the computer cluster of the ISMT of the University of Duisburg-Essen. Using MPI (www.mpi.com), the computational domain was subdivided and computed in parallel on 8 – 32 CPUs. With exceptions, the solution time was approximately 5 days for the wave-added resistance computations and 3 weeks for propulsion computations. Overall, approximately 500 cases of

the wave-added resistance and approximately 100 self-propelled cases were computed and considered in this work. Computations were performed using the solvers Comet (Ley et al. 2014), OpenFOAM (OpenFOAM, 2016), STAR-CCM+ (Siemens, 2016) and fine/Marine (Numeca, 2013).

4 Verification and Validation

To validate the numerical methods and simulation setups, different well-known test cases were used. Initially grid studies were performed. Then the calm water resistance, time histories, amplitudes and averaged values of motions and forces of the test cases in waves were computed and carefully compared with experimental results. Moreover, computed and measured propeller forces in open water conditions and behind the ship (calm water and waves) were compared. Used test cases and their experimental setups, numerical grids, discretization errors, and selected results of the performed validation work are presented in this chapter.

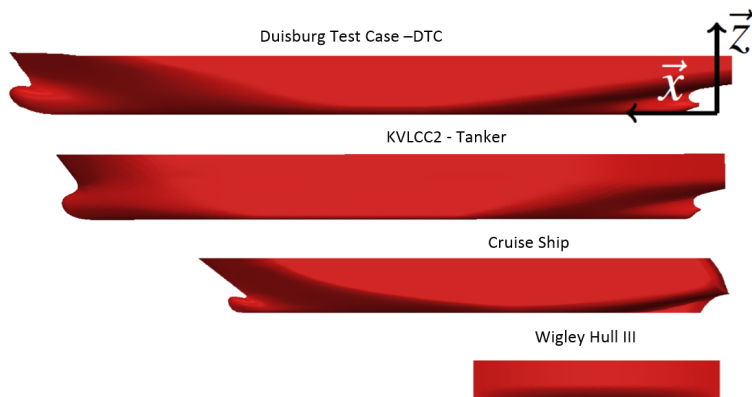


Figure 9: Considered test cases

4.1 Test Cases

To cover a wide range of practical needs, investigations were performed for four different conventional ship types. Specifically, studies were performed for a modern medium-size cruise ship (Ley et al., 2014; Valanto and Hong, 2015), a post-Panamax 14000 TEU containership referred to as the Duisburg Test Case (DTC) (el Moctar et al., 2010; el Moctar et al., 2016; Sprenger et al., 2016), the MOERI tanker KVLCC2 (Simman, 2008), and the well-known Wigley hull (Journee, 2003). Figure 9 presents an overview of the test cases. Beside the ship length, the block coefficient and the bow shape varies significantly, which may have great influence on the performance of the test cases in waves. Their main parameters are presented in Table 1. Figure 10 shows all section plans.

Extensive model tests in calm water and in waves were performed for all test cases. The Hamburg Ship Model Basin (HSVA) performed the model test for the cruise ship. The Norwegian Marine Technology Research Institute (MARINTEK) and the SVA Potsdam conducted the test for the containership (with different sized models). The tanker was tested at the Maritime and Ocean Engineering Research Institute (MOERI). Finally, the Delft University of Technology performed the test for the Wigley hull. To measure forces in waves, the cruise ship and the containership were moored with soft springs that held the models captive and allowed them to move with six degrees of freedom, see figure 12. Transducers were attached to the springs to measure the towing force. The tanker and the Wigley hull were only free to heave and pitch. All other degrees of freedom were suppressed.

For the cruise ship and the containership, the propulsion characteristics in waves were determined in addition. For these computations, the two ships were equipped with all appendages, including rudder and propeller. The configurations of the propulsion components are shown in figure 11. The propeller and rudder data are summarized in Table 2.

Table 1: Main parameters of investigated ships

| Symbol | Containership DTC | Tanker KVLC2 | Cruise Ship | Wigley Hull III |
|----------------------------------|----------------------------|--------------|--------------|-----------------|
| Length [m] | 355.00 | 320 | 216.80 | 100 |
| Width [m] | 51.00 | 58 | 32.20 | 10 |
| Draft [m] | 14.50 | 20.8 | 7.20 | 6.26 |
| Displacement [m ³] | 173467 | 312622 | 33219 | 2888 |
| Wetted surface [m ²] | 22032.00 | 27194.00 | 8011.90 | 1490.80 |
| Block coefficient [-] | 0.66 | 0.81 | 0.65 | 0.46 |
| Froude number [-] | 0.052, 0.087, 0.139, 0.218 | 0.142 | 0.159, 0.223 | 0.30 |
| Metacentric height [m] | 1.5 | 5.71 | 2.75 | 0.65 |
| Vertical center of gravity [m] | 19.851 | 18.6 | 15.054 | 5.61 |
| Radius of gyration [m] | 88.75 | 80.00 | 59.58 | 25.00 |
| Radius of gyration [m] | 20.4 | 23.2 | 12.88 | 4 |
| Scale factor [-] | 59.4, 63.64 | 100.0 | 36.0 | 33.0 |

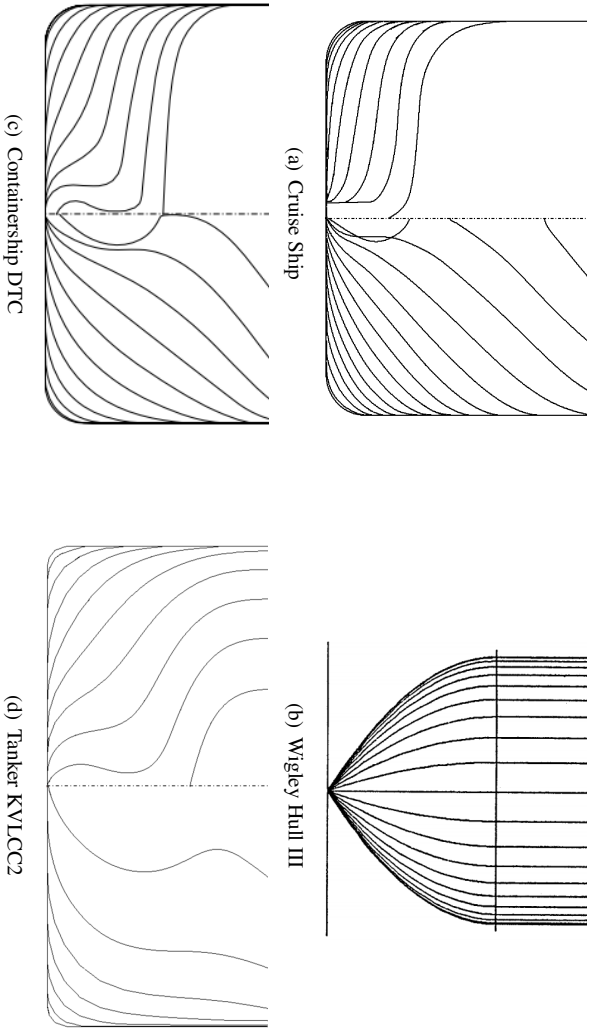
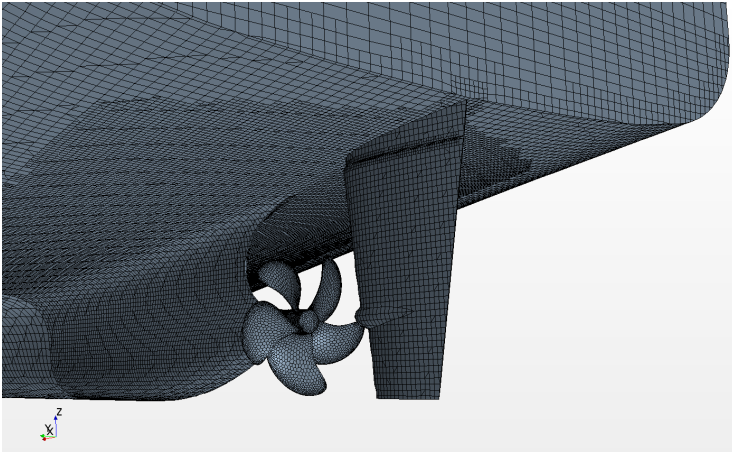
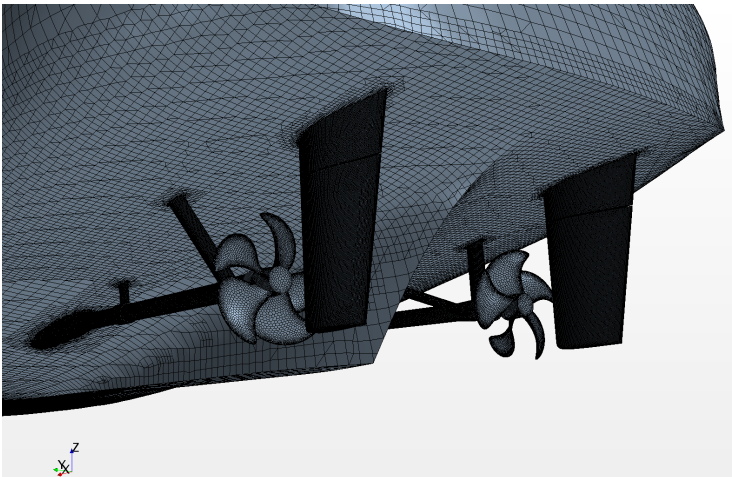


Figure 10: Section plans of the Cruise Ship, the Containership DTC, the Tanker KVLCC2 and the Wigley Hull III



(a) Containership DTC



(b) Cruise Ship

Figure 11: Configurations of the propulsion components of the Containership DTC (left) and the Cruise Ship (right)

Table 2: Parameters of the rudder and the propellers of the Containership DTC and the Cruise Ship

| | Symbol | Cruise Ship | Containership DTC |
|--------------------------|-----------|-----------------|------------------------|
| Number of propellers [-] | - | 2 | 1 |
| Type [-] | - | Fixed pitch | Fixed pitch |
| Propeller diameter [m] | D | 5.2 | 8.911 |
| Number of blades [-] | z | 5 | 5 |
| Disk area ratio [-] | A_e/A_0 | 0.8681 | 0.8 |
| Mean pitch ratio [-] | P_M/D | 1.0921 | 0.859 |
| Sense of rotation [-] | - | Inward over top | Right-handed |
| Number of rudders [-] | - | 2 | 1 |
| Type [-] | - | Conventional | 5° Twisted, Costa bulb |
| Height [m] | h_R | 4.5 | 12.9 |
| Area [m ²] | A_R | 18.7 | 62.1 |

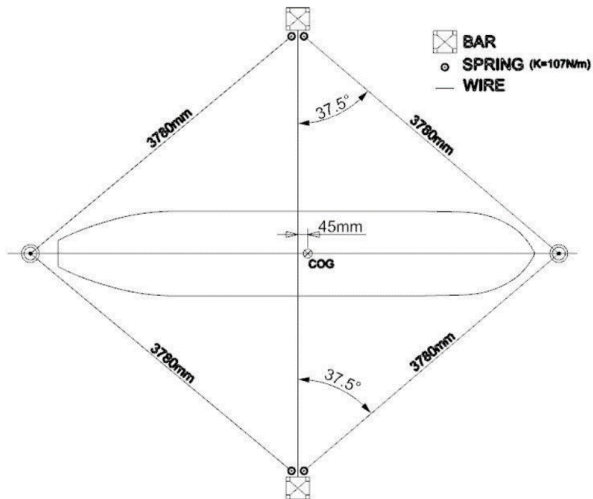
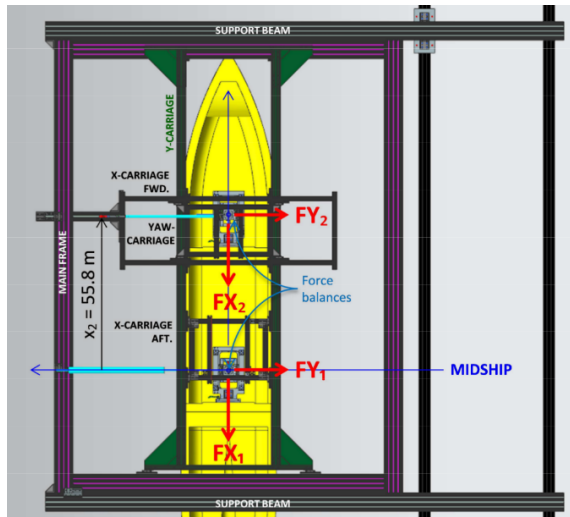


Figure 12: Experimental setup for the Cruise Ship (top) and the Container-ship DTC (bottom) (el Moctar, 2016)

4.2 Numerical grids and discretization errors

To determine wave-added resistance and propulsion characteristics in waves it is essential to use identical numerical methods, setups and grids for all associated computations (see section 2). Especially the discretization of the hulls and the appendages and of the incident waves was kept unchanged for all computations. To evaluate discretization errors, initially, grid studies in calm water and in waves were performed. When necessary, only very small changes of the spacial discretization were made (e.g. when adding propeller geometry) and all associated computations (e.g. calm water or propeller open water computations) were performed again with the updated grid. If serious changes were needed (e.g. for oblique wave computations), a new grid study for the changed grid was performed. In this section representative numerical grids are presented and related grid studies are shown.

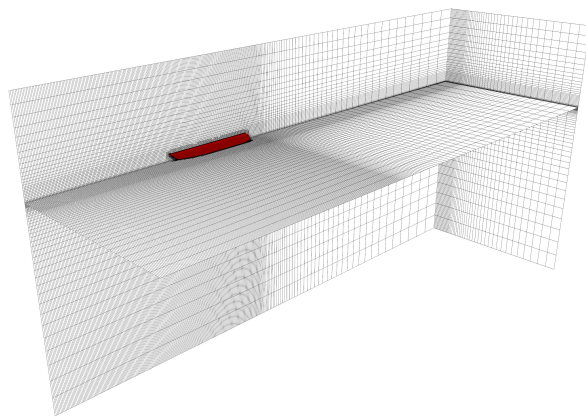


Figure 13: *Representative numerical grid of the performed computations; here for the Cruise Ship*

Computations were performed on unstructured grids consisting of hexahedral control volumes. Dimensions of the computational domain were oriented to the length of the ship models. The inlet boundary was located at

least one model length ahead of the models' forward perpendicular to reduce the free running length of incident waves; the outlet boundary, at least three model lengths behind the models' aft perpendicular to avoid wave reflection; the side boundaries, two-and a-half model lengths to port and starboard of the models' central symmetry plane; the bottom, at two model lengths below the calm water surface; and the top, at one model length above the calm water surface. To illustrate, figure13 shows the computational fluid domain for the cruise ship. To accurately resolve the wave pattern and the incident wave field, grids were locally refined in the vicinity of the free surface and in areas surrounding the hull. To dampen incident and hull-induced waves, the control volumes were smoothly stretched towards the outlet boundaries. To properly account for the boundary layer on the hull surface, prism layers were included and wall functions applied. The grids used comprised between $1.6 \cdot 10^6$ and $20.0 \cdot 10^6$ control volumes for the entire flow domain.

To investigate the influence of spatial and temporal discretization on the wave-added resistance, grid studies for all ships were performed advancing in calm water as well as in waves. Grids were refined systematically by multiplying the grids' base size in all directions by a factor of about $\sqrt{1.7}$. For each ship, a coarse, a medium, and a fine grid comprising 1.6 million to 7.5 million control volumes, extending over both port and starboard sides, were generated. For the containership, additional computations were conducted on a very fine grid comprising 20 million control volumes. To minimize the influence of turbulence modeling and wall functions, the dimensionless wall distance, y^+ , on hulls' wetted surfaces was kept constant for all grids at a mean value of approximately 80. Figure14 depicts this situation for the containership at $Fn = 0.218$ and $Re = 1.0 \cdot 10^7$. Grid studies for the containership were performed with scaling factor of 59.407 according to the model tests performed at SVA-Potsdam.

For the containership and the cruise ship, figure15 plots computed total and frictional calm water resistance coefficients, C_T , and the frictional resistance coefficient, C_F , according to the ITTC '57 friction line, versus the total numbers of control volumes. Frictional resistance coefficients compare favorably to the ITTC '57 value and remain nearly constant, whereas total resistance coefficients decrease with increasing number of control volumes. The reason



Figure 14: Dimensionless wall distance, y^+ , on wetted surfaces of the Containership DTC at $\mathbf{Re} = 1.0 \cdot 10^7$ and $\mathbf{Fn} = 0.218$

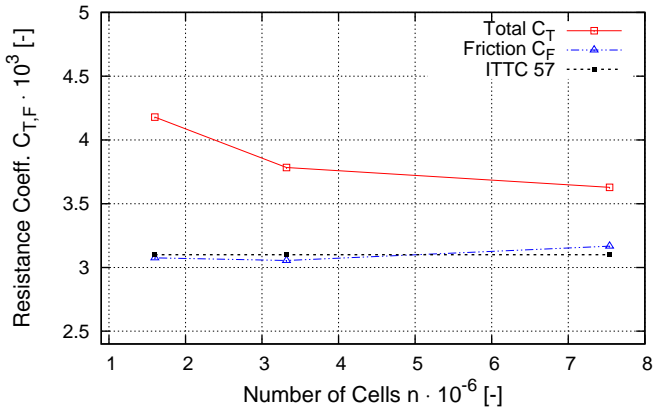
for this is numerical diffusion, which influenced the viscous pressure resistance and decreased with decreasing discretization errors resulting from finer grids.

Grid uncertainty studies for calm water resistance based on the ITTC procedure have been performed (ITTC, 1999). Table 3 presents the total resistance coefficient and the grid uncertainty, U_G , for the containership as an example.

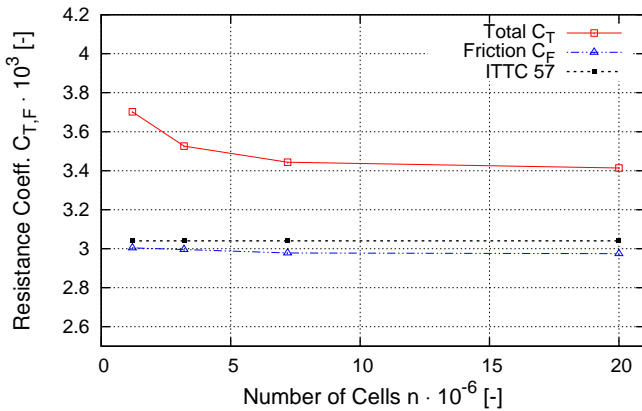
Table 3: Containership DTC at $\mathbf{Fn} = 0.218$: Results of the grid study and grid uncertainty, U_G

| | Grid 4 | Grid 3 | Grid 2 | Grid 1 | U_G |
|-----------------------|--------|--------|--------|--------|-------|
| $C_T \cdot 10^3$ | 3.702 | 3.526 | 3.444 | 3.414 | 1.25% |
| % of finer grid value | | -4.75% | -2.33% | -0.87% | |

To evaluate the influence of the discretization on the results of the computations with waves, RAOs of the heave and pitch motion and of the wave-added resistance have been computed with the coarse, medium and fine grid. To consider wave damping, affecting especially the short waves, normalization was performed using the actual computed (instead of the target) wave heights. Figure 16 - 18 plot the RAOs versus wave length to ship length ratio, λ_w/L , and normalized wave frequency, $(L/\lambda_w)^{1/2}$. The relatively small deviations between coefficients computed with the different sized grids led to



(a) Cruise Ship



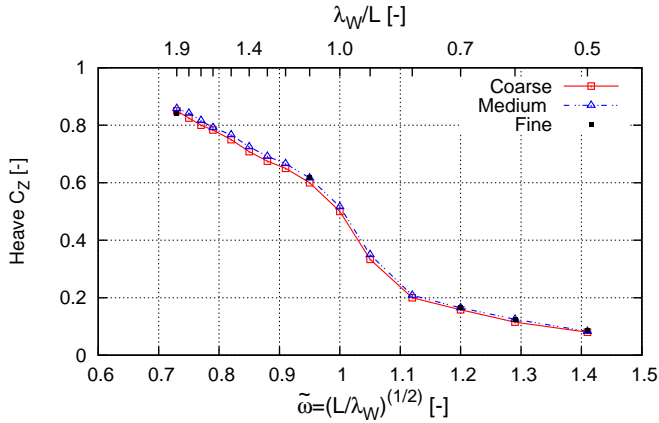
(b) Containership DTC

Figure 15: Computed total and frictional calm water resistance coefficients versus number of control volumes for the Containership DTC at $\mathbf{Fn} = 0.218$ and $\mathbf{Re} = 1.0 \cdot 10^7$ and the Cruise Ship at $\mathbf{Fn} = 0.159$ and $\mathbf{Re} = 1.1 \cdot 10^7$

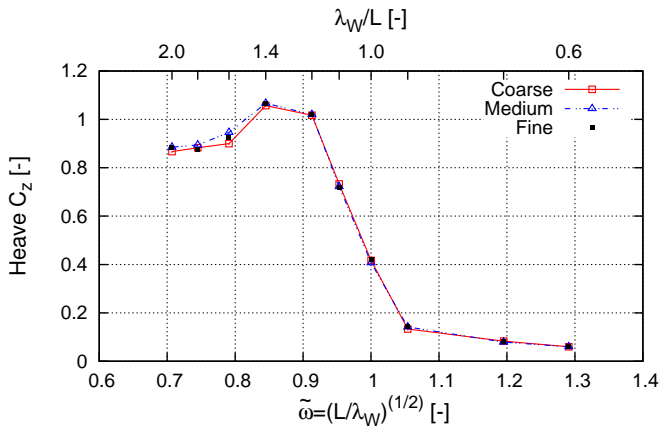
the conclusion, that the spatial discretization does not significantly influence the normalized wave-added resistance coefficient as long as the wave height at bow and stern of the model was constant, and the actual computed wave height was used for normalization.

To determine the propulsion characteristics, the propeller open water characteristics need to be computed (see section 2). Therefore, grids with either hexahedral or polyhedral cells were used. To assess grid sensitivity, coarse grids consisting of approximately $0.12 \cdot 10^6$ control volumes and fine grids consisting of approximately $1.3 \cdot 10^6$ control volumes for each propeller blade were generated. A representative grid discretizing a propeller is shown in figure 19.

Figure 20 presents the propeller open water characteristics computed with a coarse and a fine grid. While the grid size used here hardly influenced computed propeller thrusts, the propeller torques computed on the coarse grid deviate slightly from measured values as seen on the left side of figure 20. The maximum deviation between measured and computed propeller thrust and torque obtained with the fine grid does not exceed 3% for all propellers. However, maximum deviation of the propeller thrust computed with the coarse grid is 3.8% and of the propeller torque is 5.3% (cruise ship propeller only).

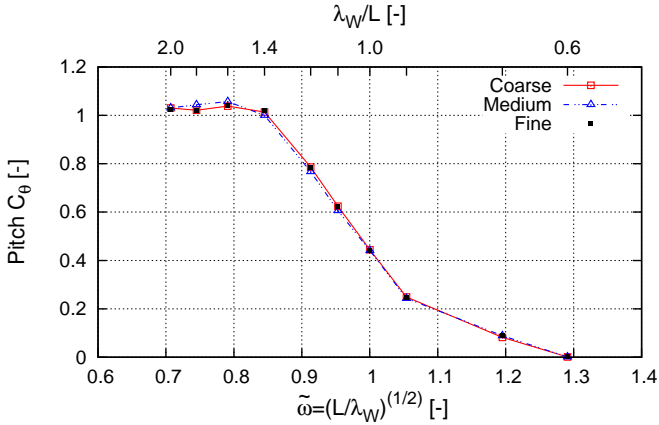


(a) Containership DTC

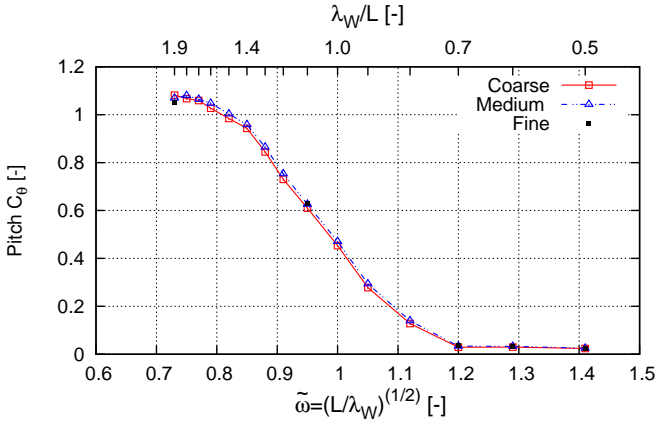


(b) Tanker KVLCC2

Figure 16: Heave RAOs for the Containership DTC at $\mathbf{Fn} = \mathbf{0.218}$ and the Tanker KVLCC2 at $\mathbf{Fn} = \mathbf{0.142}$ versus normalized wave frequency and wave length to ship length ratio computed on different sized grids

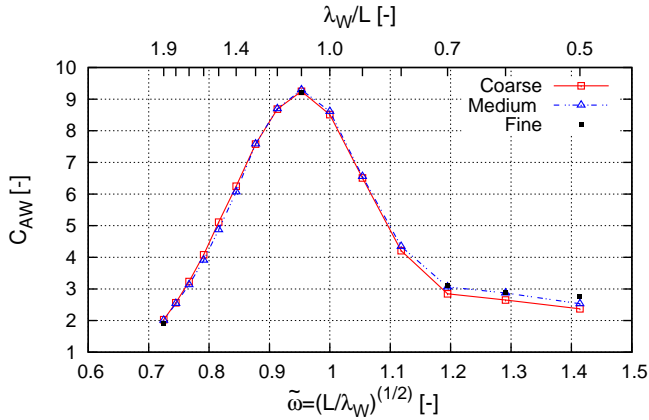


(a) Containership DTC

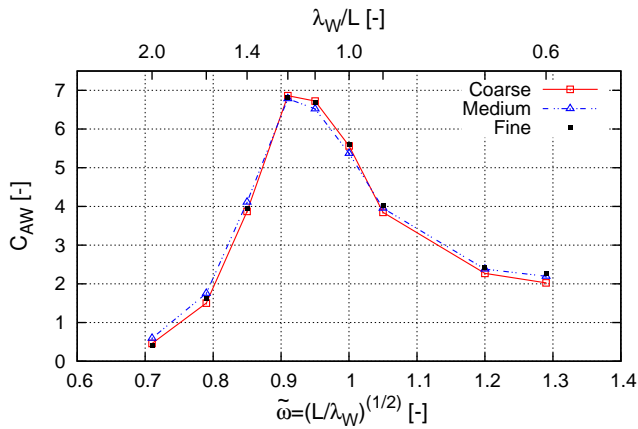


(b) Tanker KVLCC2

Figure 17: Pitch RAOs for the Containership DTC at $\mathbf{Fn} = 0.218$ and the Tanker KVLCC2 at $\mathbf{Fn} = 0.142$ versus normalized wave frequency and wave length to ship length ratio computed on different sized grids



(a) Containership DTC



(b) Tanker KVLCC2

Figure 18: Wave-added resistance RAOs for the Containership DTC at $\mathbf{Fn} = 0.218$ and the Tanker KVLCC2 at $\mathbf{Fn} = 0.142$ versus normalized wave frequency and wave length to ship length ratio computed on different sized grids

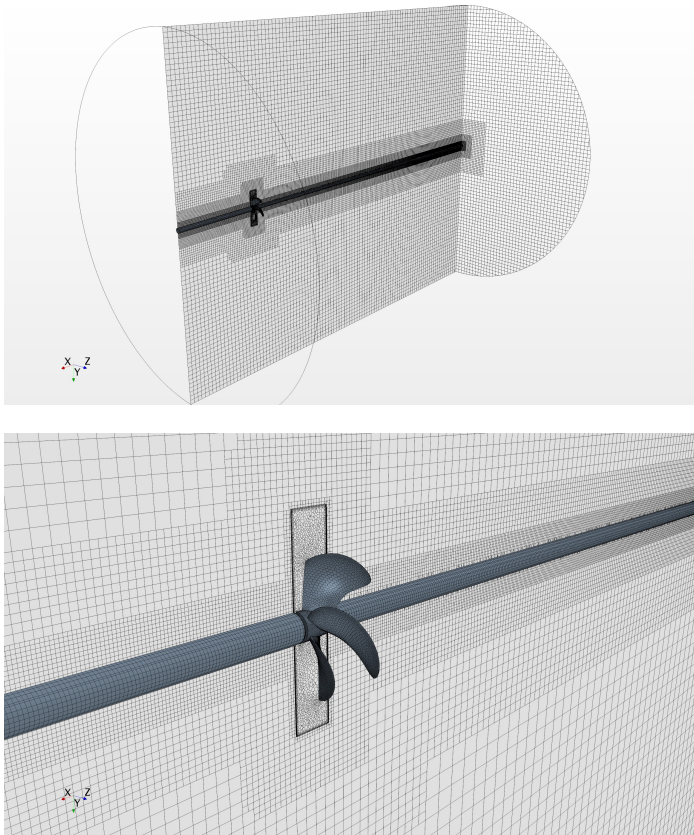


Figure 19: Representative spatial discretization of a propeller for numerical investigations

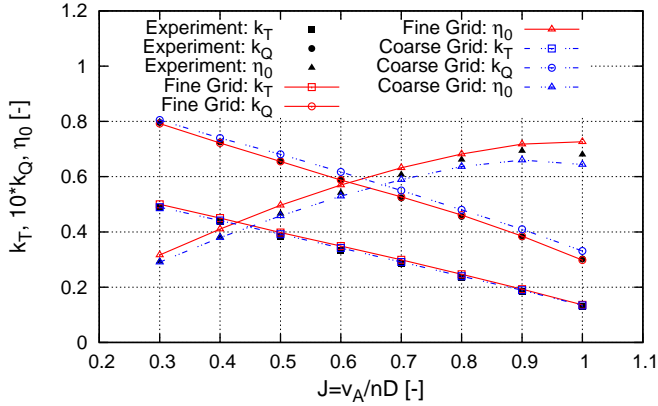


Figure 20: Measured and computed propeller open water characteristics for the Cruise Ship

For the propulsion computations, the above presented grids were combined. Depending on resistance or propulsion tests, the propeller domain with or without the geometry of the propeller was cross-linked to the grid. Figure 21 shows a side view of grid resolution of the computational fluid domain ahead of the models (left) and in the vicinity of the turning propeller (right) for self-propulsion simulations. Propulsion simulations utilized the sliding grid technique by generating a cylindrical block around the propeller region which glides along the surrounding grid of the hull and rudder region. The grid interface between the two grid regions was locally refined. To resolve the boundary layer at the hull, rudder and propeller prism layers were included and wall functions were applied. For comparison purposes, simulations in calm water as well as in waves were performed on identical grids again. When symmetry conditions allowed it, only half of the flow domain was modeled. This was the case for the computation with the cruise ship.

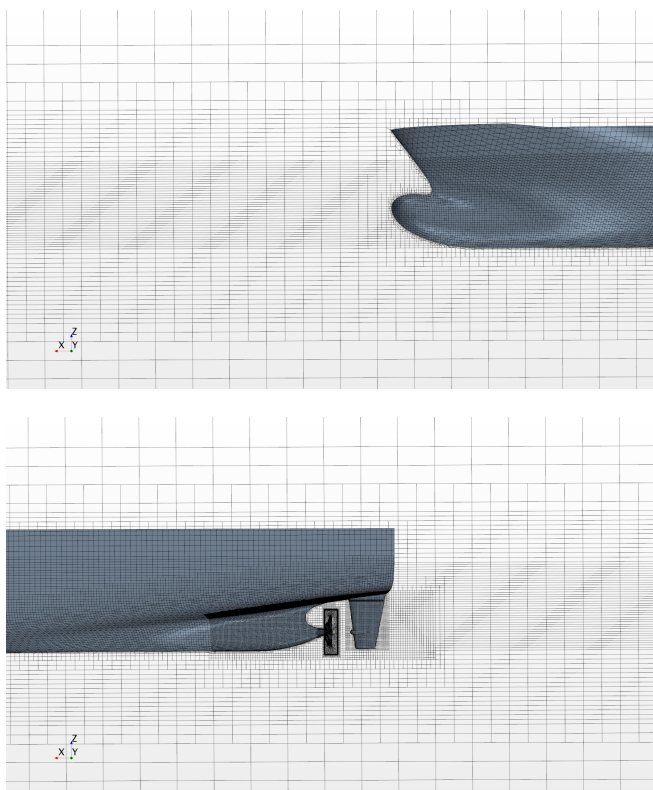


Figure 21: Local refinements of the numerical grids ahead of and behind the models

To validate grids and setup, propulsion tests were computed for calm water condition first. In table 4 the measured and computed coefficients of the propeller thrust and torque are presented. The computed results show excellent agreement with the experimental data. Thus, the numerical methods and grids showed their suitability for the intended investigation of the ship's performance in waves and were used for the computations.

Table 4: Coefficients of the measured and computed propulsion forces for the Cruise Ship and the Containership DTC in calm water

| | k_T [-] | | | | $10 \cdot k_Q$ [-] | | | |
|-------------|-----------|-------|-------|----------|--------------------|-------|----------|--|
| | F_n [-] | Comp. | Exp. | Dev. [%] | Comp. | Exp. | Dev. [%] | |
| Cruise Ship | 0.159 | 0.200 | 0.196 | 2.04 | 0.409 | 0.417 | 1.92 | |
| DTC | 0.223 | 0.207 | 0.201 | 2.98 | 0.402 | 0.407 | 1.23 | |
| | 0.139 | 0.260 | 0.245 | 6.12 | 0.429 | 0.419 | 2.38 | |

5 Wave-Added Resistance

As discussed in section 2, the wave-added resistance is of high practical interest. Thus, in this work, a fundamental investigation of the wave-added resistance was performed using the RANS-based field method. The objective was to investigate the basic physics of the wave-added resistance. Specifically, particular emphasis was placed on the following research questions:

- How does ship speed influence the wave-added resistance?
- How does friction affect the wave-added resistance?
- How do the radiation and diffraction problems interact in the nonlinear regime? Can these problems be considered separately?
- How does the wave-added resistance depend on the wave height? Does the quadratic correlation also hold for steep waves?
- How does the encounter angle influence the wave-added resistance?

In this chapter, the investigation of the wave-added resistance will be described in detail. Thereby, the computational procedure, pre- and post-processing, and the results will be presented. The content of this chapter has been published in Sigmund and el Moctar (2017), partly in exact wording.

5.1 Computational Procedure

The wave-added resistances of the cruise ship, the containership, the tanker and the Wigley hull were computed for 10 – 12 regular head waves of different length. With the wave length ranging from 0.2 to 2.5 times the ship length, both short and long waves were considered. Relatively short waves are of special interest, since large ships operate nearly all their lifetime in these waves. The test matrix for each ship is shown in Table 5 and 6. The

wave-added resistance of the containership has been investigated at a model scale of 63.64 according to the model tests performed at MARINTEK.

Determining the wave-added resistance of a ship using RANS methods comprises three steps. First, the calm water resistance for each specific ship speed is computed. Second, the averaged longitudinal force in waves is determined. Here, the ships were free to heave and pitch. All other degrees of freedom were suppressed. Third, the wave-added resistance is calculated by subtracting the calm water resistance from the time-averaged longitudinal force in waves. These steps, were performed in the same way to determine the frictional part of the wave-added resistance. For this procedure, it is essential to use the same numerical grids and test setups for all computations (in calm water as well as in waves) to minimize possible errors caused by spatial and temporal discretization, model test scale effects, and iterative computational techniques. For model scale conditions the numerical grids consisted of approximately 3.2×10^6 control volumes, and it relied on a time step of 0.005s, whereby the Courant number, on average, was less than 0.5. Representative grids are presented in section 4. At inlet boundaries, velocities, volume fractions, turbulent kinetic energies, and dissipation rates were specified. The hull surface was defined as no-slip wall. At outlet and top boundaries, hydrostatic boundary conditions were specified. The origin of the inertial frames was located on the ships' base line at their aft perpendiculars. The origin of the ship-fixed reference frames was situated at the ships' center of gravity.

Table 5: Speed and wave parameters of the performed computations with the Cruise Ship and the Containership DTC in ship scale

| Ship Type | Fn [-] | λ_W/L [-] | h_W [m] | h_W/λ_W [%] |
|-------------|--------------|-------------------|-----------|---------------------|
| | | Calm Water | | |
| | | 0.28 | 1.55 | 2.52 |
| | | 0.39 | 2.17 | 2.53 |
| | | 0.49 | 3.6 | 3.34 |
| | | 0.66 | 3.6 | 2.48 |
| | | 0.79 | 3.6 | 2.07 |
| Cruise Ship | 0.159, 0.223 | 0.89 | 3.6 | 1.84 |
| | | 0.98 | 3.6 | 1.67 |
| | | 1.09 | 3.6 | 1.50 |
| | | 1.23 | 3.6 | 1.33 |
| | | 1.41 | 3.6 | 1.16 |
| | | 1.8 | 3.6 | 0.91 |
| | | 2.5 | 3.6 | 0.65 |
| | | Calm Water | | |
| | | 0.22 | 2.99 | 3.83 |
| | | 0.28 | 5.66 | 5.70 |
| | | 0.36 | 8.27 | 6.47 |
| | | 0.44 | 12.09 | 7.74 |
| | | 0.60 | 7.51 | 3.53 |
| | | 0.80 | 9.93 | 3.50 |
| DTC | 0.052, 0.139 | 0.91 | 9.04 | 2.80 |
| | | 1.00 | 10.18 | 2.87 |
| | | 1.09 | 11.20 | 2.90 |
| | | 1.20 | 10.18 | 2.39 |
| | | 1.40 | 12.73 | 2.56 |
| | | 1.80 | 12.73 | 1.99 |
| | | 2.50 | 12.73 | 1.43 |

Table 6: Speed and wave parameters of the performed computations with the Tanker KVLCC2 and the Wigley Hull in ship scale

| Ship Type | Fn [-] | λ_W/L [-] | h_W [m] | h_W/λ_W [%] | | |
|-----------------|----------|-------------------|-----------|---------------------|--|--|
| Calm Water | | | | | | |
| KVLCC2 | 0.142 | 0.2 | 6.0 | 4.69 | | |
| | | 0.3 | 6.0 | 3.13 | | |
| | | 0.4 | 6.0 | 2.34 | | |
| | | 0.5 | 6.0 | 1.88 | | |
| | | 0.6 | 6.0 | 1.56 | | |
| | | 0.7 | 6.0 | 1.34 | | |
| | | 0.9 | 6.0 | 1.04 | | |
| | | 1.0 | 6.0 | 0.94 | | |
| | | 1.1 | 6.0 | 0.85 | | |
| | | 1.2 | 6.0 | 0.78 | | |
| | | 1.4 | 6.0 | 0.67 | | |
| Wigley Hull III | 0.30 | 1.6 | 6.0 | 0.59 | | |
| | | 1.8 | 6.0 | 0.52 | | |
| | | 2.0 | 6.0 | 0.47 | | |
| | | Calm Water | | | | |
| | | 0.50 | 1.35 | 2.71 | | |
| | | 0.59 | 1.26 | 2.13 | | |
| | | 0.75 | 1.37 | 1.82 | | |
| | | 0.91 | 1.04 | 1.15 | | |
| | | 1.00 | 1.19 | 1.19 | | |
| | | 1.05 | 1.04 | 0.99 | | |
| | | 1.11 | 0.91 | 0.82 | | |
| 1.25 | 1.01 | 0.81 | | | | |
| 1.38 | 0.90 | 0.65 | | | | |
| 1.50 | 0.81 | 0.54 | | | | |
| 1.75 | 1.42 | 0.81 | | | | |
| 2.00 | 1.28 | 0.64 | | | | |

5.2 Results

Wave patterns in calm water (top) and in incoming waves (bottom) for the containership computed on the same numerical grid are shown in figure 22. Obviously, the ship induced wave pattern is more pronounced in waves. Furthermore, waves were damped behind the model to avoid wave reflection.

Response amplitude operators were computed using only one numerical grid and one setup for all wave frequencies. The actual wave amplitudes of shortest waves were slightly lower than the amplitudes specified at the inlet boundary. Due to the increasing numbers of cells per wavelength, the difference between target and actual wave amplitude was decreasing for longer waves. In waves longer than 0.6 times ship length ($\lambda_W/L > 0.6$), deviations between target and actual wave amplitude were negligible. However, computed wave amplitudes of undisturbed waves were monitored next to a ship's bow in all computations, and actual amplitudes were used for normalization. Exemplary, figure 23 depicts target and actual wave amplitudes for $\lambda_W/L = 0.3$. For the tanker in wave lengths up to $\lambda_W/L = 0.6$, table 7 lists the percentage deviations of actual wave amplitudes from their target values. Deviations in longer waves were negligible.

Table 7: Actual and target wave amplitude of short waves computations with the tanker KVLCC2 at $\mathbf{Fn} = 0.142$

| $\lambda_W/L[-]$ | Target Amp. [m] | Actual Amp. [m] | Deviation [%] |
|------------------|-----------------|-----------------|---------------|
| 0.2 | 0.03 | 0.023 | 23.0 |
| 0.3 | 0.03 | 0.025 | 16.6 |
| 0.4 | 0.03 | 0.028 | 6.6 |
| 0.5 | 0.03 | 0.029 | 3.3 |
| 0.6 | 0.03 | 0.03 | 0.0 |

Table 8 summarizes computed and measured calm water resistance coefficients for the four ship types advancing at constant forward speeds. This table also lists the associated Froude number as well as the percentage deviation between computed and measured values. These deviations are less than

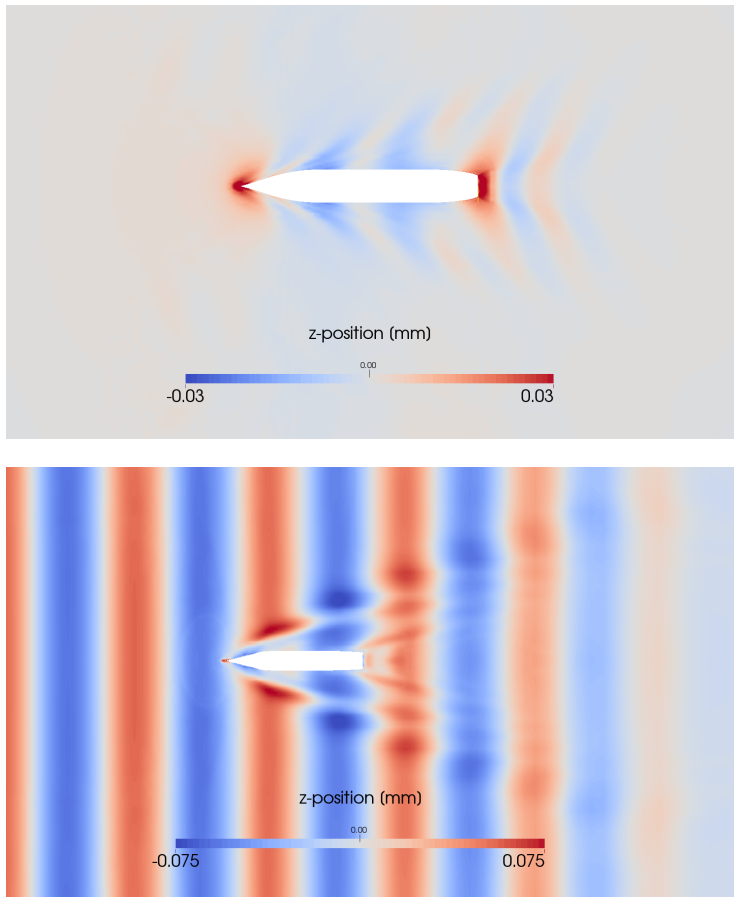


Figure 22: Computed wave pattern in calm water (top) and in regular head waves (bottom) of the Containership DTC at $\mathbf{Fn} = 0.218$, $\lambda_{\mathbf{W}}/\mathbf{L} = 1.125$ and $\mathbf{h}_{\mathbf{W}} = 0.12\mathbf{m}$

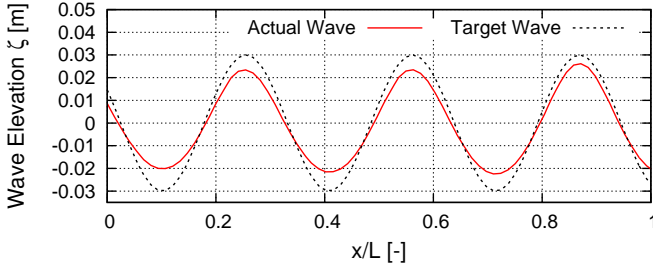


Figure 23: Actual and target short wave amplitude near bow of the Tanker KVLCC2 at $\mathbf{Fn} = 0.142$ and $\lambda_W/L = 0.3$

five percent, i.e., they are small and therefore deemed sufficiently accurate to carry on with the computations of the wave-added resistance.

Figure 24 presents time histories of computed and experimentally measured heave and pitch motions for the containership in regular head waves. The solid line identifies computed motions; the dotted line, experimentally measured motions. These motions are nearly harmonic and, generally, their amplitudes and phase angles compare favorably to measurements. The deviation between computed and measured amplitudes is less than 2%. Although not shown here, the corresponding time histories for the other three ships were similar; however, in the shortest waves, measured motions for these other ship typed were not always harmonic.

Figures 25 - 30 present time histories and mean values of computed longitudinal force, F_X , for the four investigated ships advancing at constant forward speed in calm water as well as in short, intermediately long, and long regular head waves. A dashed line identifies the force in calm water; a solid fluctuating line, the total longitudinal force in waves; and a dash/dotted line, the mean force in waves. The difference between dashed and dash/dotted lines defines the wave-added resistance. This difference is largest in figures 27 and 28. Here, waves length is about equal to ship length and the wave-added resistance attains its maximum ($\lambda_W/L \approx 1$). This is so because at this wave

Table 8: Computed and measured calm water resistance coefficients of all ships

| | $F_n[-]$ | $C_T \cdot 10^{-3}[-]$ | | | $C_F \cdot 10^{-3}[-]$ | | |
|-----------------|----------|------------------------|-------|-----------|------------------------|-------|-----------|
| | | CFD | EFD | Diff. [%] | CFD | EFD | Diff. [%] |
| Cruise Ship | 0.159 | 3.79 | 4.069 | -6.80 | 3.057 | 3.177 | -3.76 |
| | 0.223 | 3.97 | 4.088 | -2.88 | 3.05 | 2.994 | 2.00 |
| Containership | 0.14 | 3.774 | 3.808 | -0.89 | 3.106 | 3.245 | -4.20 |
| Tanker KVLCC2 | 0.142 | 5.181 | 5.066 | 2.99 | 3.824 | 3.862 | -0.98 |
| Wigley Hull III | 0.3 | 5.705 | 5.449 | 4.71 | 3.315 | 3.364 | -1.45 |

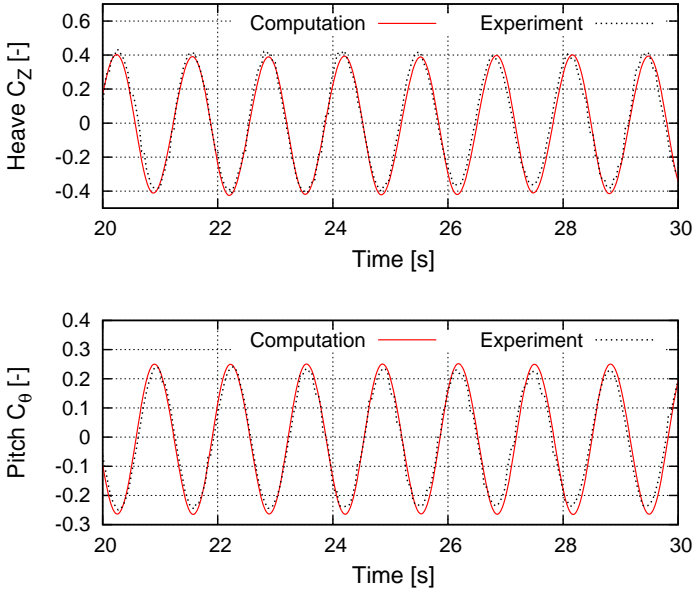
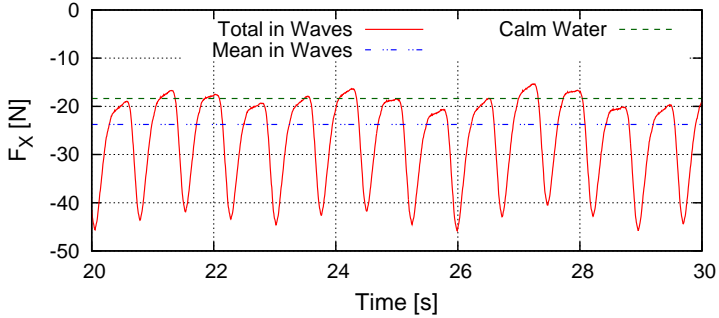


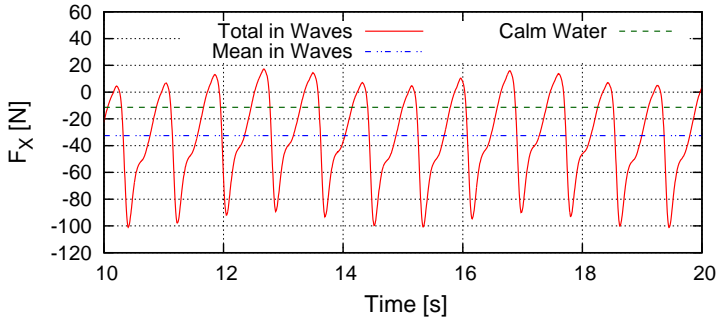
Figure 24: Computed and measured time histories of heave and pitch motion of the Containership at $\mathbf{Fn} = 0.139$, $\lambda_{\mathbf{W}}/\mathbf{L} = 0.91$ and $\mathbf{h}_{\mathbf{W}} = 0.14\mathbf{m}$

length radiated waves contribute most to the wave-added resistance at this wave length and the relative motion between hull and water surface is largest.

Furthermore, it is seen that, in shorter waves, nonlinearities of longitudinal force for the cruise ship and the containership are especially pronounced (see figures 25 and 27). It is these ships that are characterized by higher bow flare angles. Especially for the tanker in short waves, additional lower oscillation frequencies are visible. Generally, these low frequencies were considered determine mean values.



(a) Cruise Ship, $\lambda_w/L = 0.39$



(b) Containership DTC, $\lambda_w/L = 0.44$

Figure 25: Computed time histories and mean values of longitudinal forces for the Cruise Ship and the Containership DTC advancing at constant forward speed in calm water and in short regular head waves

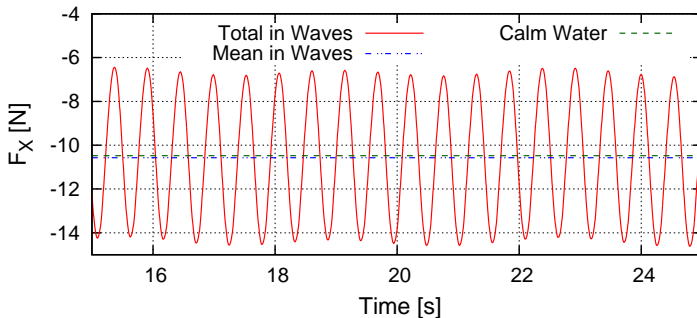
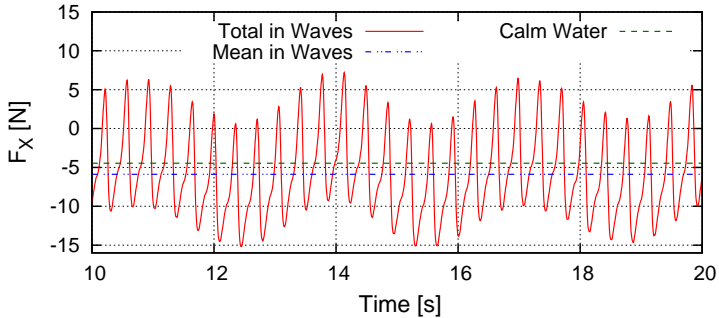
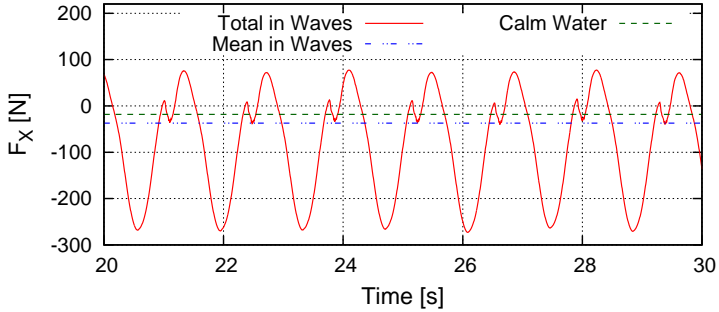
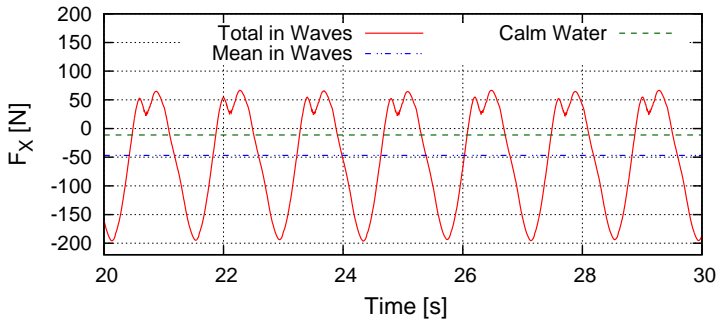


Figure 26: Computed time histories and mean values of longitudinal forces for the Tanker KVLCC2 and the Wigley Hull III advancing at constant forward speed in calm water and in short regular head waves



(a) Cruise Ship, $\lambda_w/L = 0.98$



(b) Containership DTC, $\lambda_w/L = 1.0$

Figure 27: Computed time histories and mean values of longitudinal forces for the Cruise Ship and the Containership DTC advancing at constant forward speed in calm water and in intermediately regular head waves

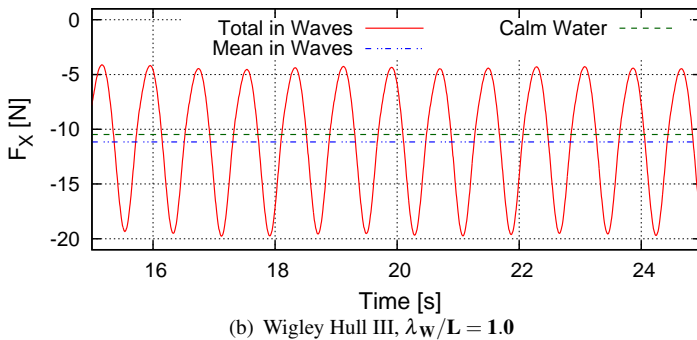
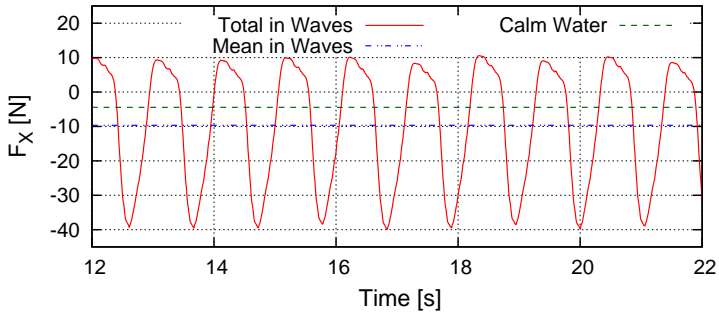
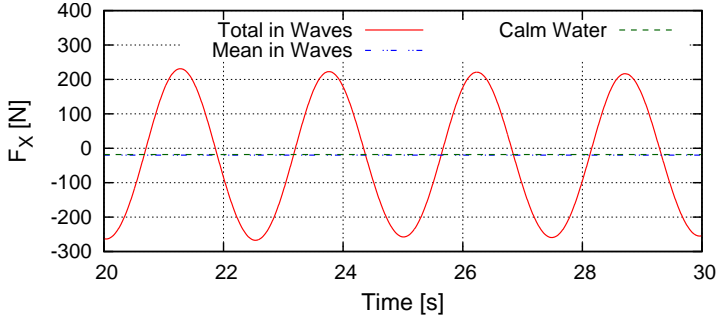
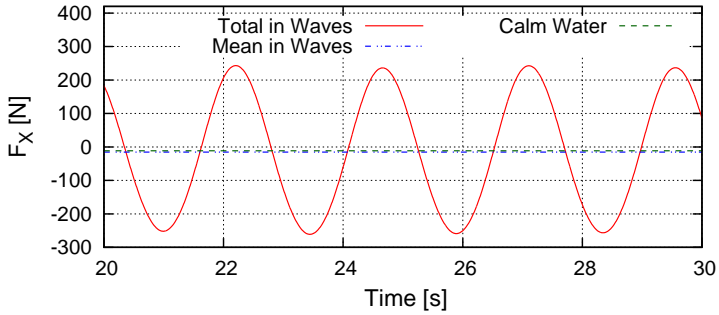


Figure 28: Computed time histories and mean values of longitudinal forces for the Tanker KVLCC2 and the Wigley hull III advancing at constant forward speed in calm water and in intermediately regular head waves



(a) Cruise Ship, $\lambda_w/L = 2.5$



(b) Containership DTC, $\lambda_w/L = 2.5$

Figure 29: Computed time histories and mean values of longitudinal forces for the Cruise Ship and the Containership DTC advancing at constant forward speed in calm water and in long regular head waves

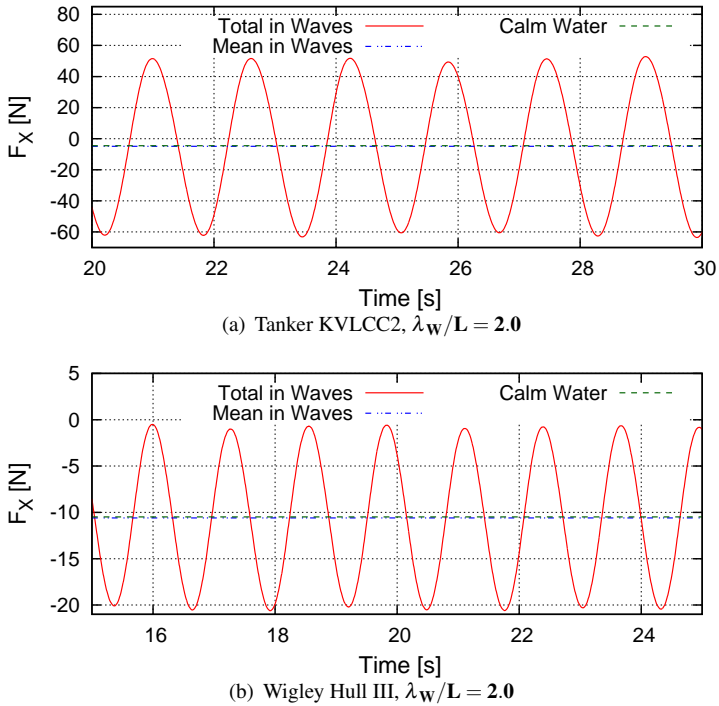


Figure 30: Computed time histories and mean values of longitudinal forces for the Tanker KVLCC2 and the Wigley hull III advancing at constant forward speed in calm water and in long regular head waves

5.2.1 Effects of Heave and Pitch Motions on the Wave-Added Resistance

The wave-added resistance is significantly influenced by ship motion responses and an accurate prediction of motion amplitudes and phase angles is very important. The comparative response amplitude operators of heave and pitch motions, shown in figures 31 - 34, demonstrate the generally fair agreement between computations and measurements. The maximum value of the response operators is slightly shifted towards longer waves for blunt ships, i.e., the tanker. Computed heave motions in the range of wave length $\lambda_W/L \approx 1$ deviate noticeably from measured motion responses of the cruise ship and the Wigley hull. Thus, computations of the heave and pitch motions using a Rankine source boundary element method (*BEM*), Soeding et al. (2014), Lyu and el Moctar (2017) were performed. *BEM* and *RANS* show similar tendency, see figure 31 (top). The unexpected deviations between computed and measured heave motions in the range of the above mentioned wave length cannot be explained and might be due to uncertainties related to the measured heave motions.

Not only the motion amplitudes, but also their phase angles between incident (head) waves and the particular motions influenced the wave-added resistance (Kashiwagi et al., 2010). Figures 35 - 37 plot these phase angles against wave parameters $\tilde{\omega}$ and λ_W/L . For the tanker, experimental measurements were available for comparison; for the containership and the cruise ship, computed results obtained from a boundary element method (Lyu and el Moctar, 2016; Riesner et al., 2017). Generally, measurements and computed results correlate favorably. As expected, in long waves ($\lambda_W/L \leq 2$), the phase angle between wave and heave motion develops against zero; the phase angle between wave and pitch motion against 90° . In the range of waves where the wave-added resistance attains peak values ($\lambda_W/L \approx 1$), phase angles are around 50° (except phase angles of the tanker's heave motion). Here, relative motions between the ship's bow and the wave elevation were largest. This caused pressures acting at the ship's bow to increase, thereby leading to a distinctly higher wave-added resistance.

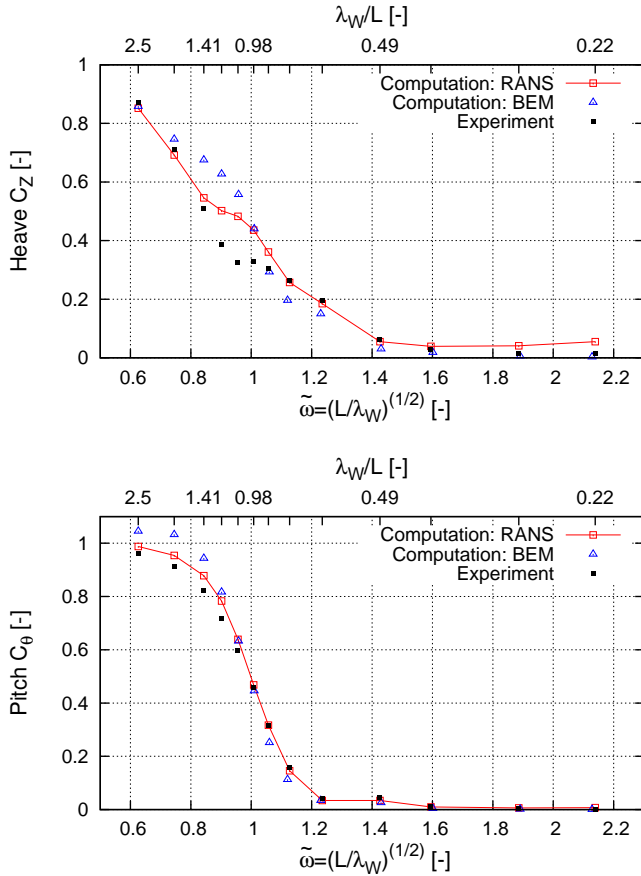


Figure 31: Computed and measured RAOs of heave and pitch amplitudes in regular head waves for the Cruise Ship at $\mathbf{Fn} = 0.223$

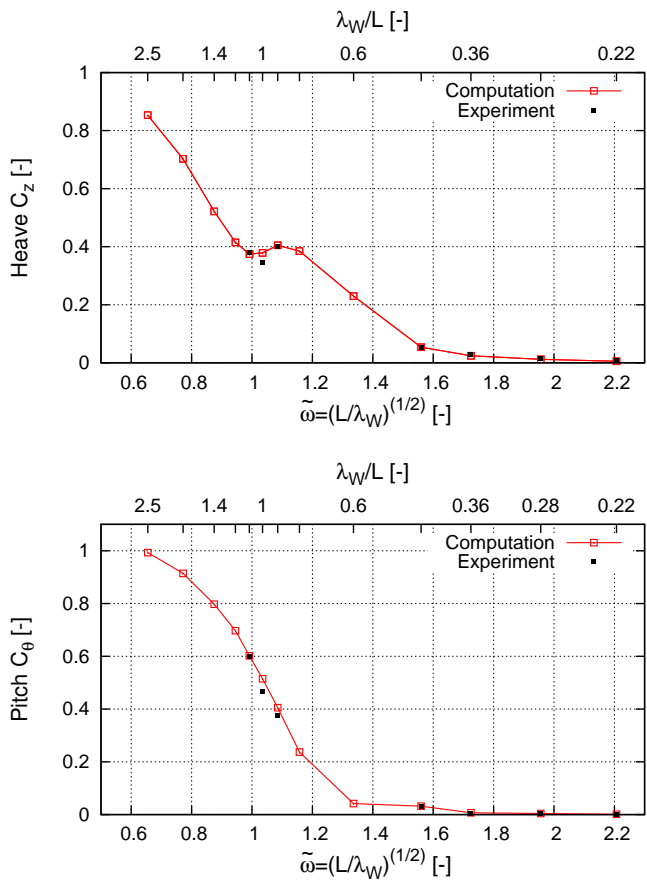


Figure 32: Computed and measured RAOs of heave and pitch amplitudes in regular head waves for the Containership DTC at $\mathbf{Fn} = \mathbf{0.139}$

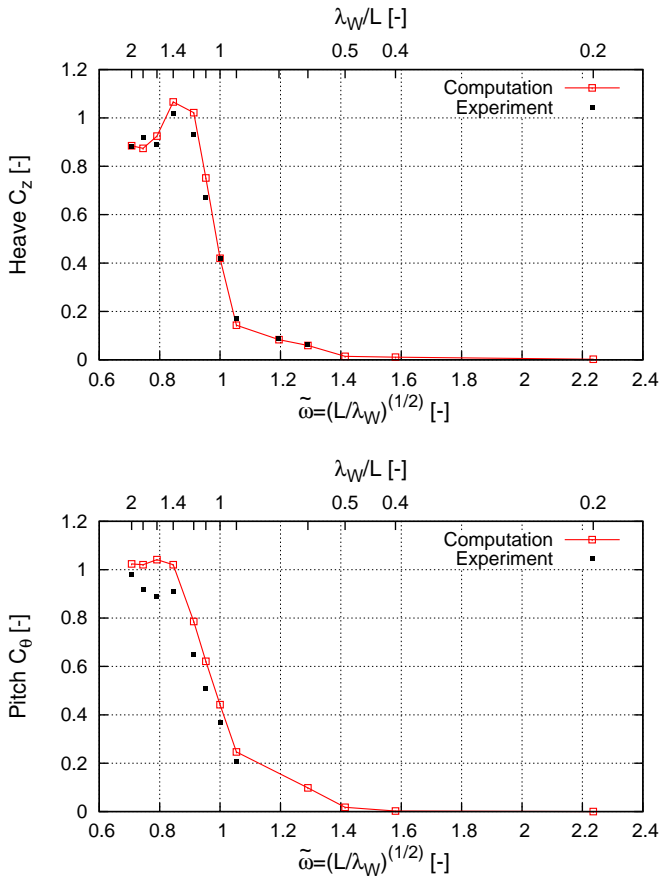


Figure 33: Computed and measured RAOs of heave and pitch amplitudes in regular head waves for the Tanker KVLCC2 at $\mathbf{Fn} = 0.142$

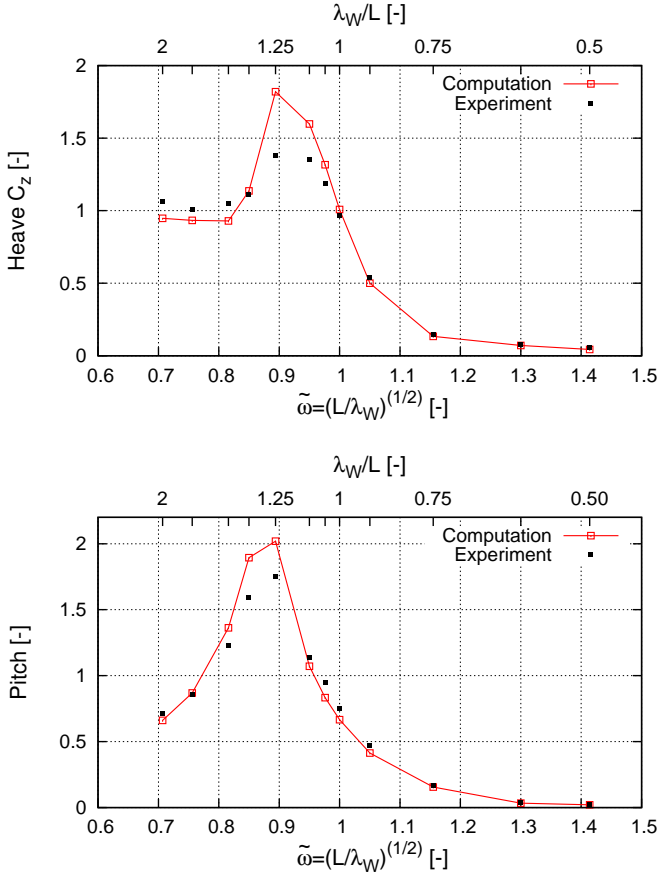


Figure 34: Computed and measured RAOs of heave and pitch amplitudes in regular head waves for the Wigley Hull III at $\mathbf{Fn} = 0.30$

Thus, in the vicinity of peak values of the wave-added resistance, a distinct correlation existed between phase angle and the wave-added resistance. In short waves ($\lambda_W/L \leq 0.6$), it was impossible to identify clear trends for any of the ships. Although some of these phase angles were large, the associated motion amplitudes were small.

The comparable normalized response amplitude operators of the wave-added resistance in regular head waves, C_{AW} , shown in figures 38 and 39, demonstrate here also the generally favorable agreement between computations and measurements. Nonlinear effects in short ($\lambda_W/L < 0.3$) and steep waves are seen to be more pronounced, and often these waves are not harmonic. Computational techniques that account for these (nonlinear) effects are important for an accurate prognosis. Boundary element methods are efficient and offer a good compromise between accuracy and computer time. However, they may be unable to entirely represent these nonlinear phenomena. In short waves, the agreement between computations and measurements is especially favorable. Here, wave diffraction dominates, and the wave radiation part of the wave-added resistance is nearly negligibly small.

The increase of the (normalized) wave-added resistance in shorter waves is predicted well by the computations. As mentioned above, the wave-added resistance in short waves is of practical relevance for larger (longer) ships because large ships operate under such conditions most of the time. However, it is appropriate to point out that in very short waves (e.g. $\lambda_W/L = 0.2$ and less) the absolute value of the wave-added resistance is relatively small compared to, for example, the calm water resistance. All wave-added resistance coefficients show a significant peak in the range of wave length equal to ship length. Here, ship motions and, consequently, radiation forces are highest. In the range of peak values for the cruise ship, the wave-added resistance coefficient is slightly overestimated. This is due to the relatively large deviations between computed and measured ship motions (see figure 31) at wave frequencies where radiation is dominant. In this case additional computation using a Rankine source method (BEM), see Soeding et al. (2014), Lyu and el Moctar (2017) were performed. BEM and RANS show similar tendency.

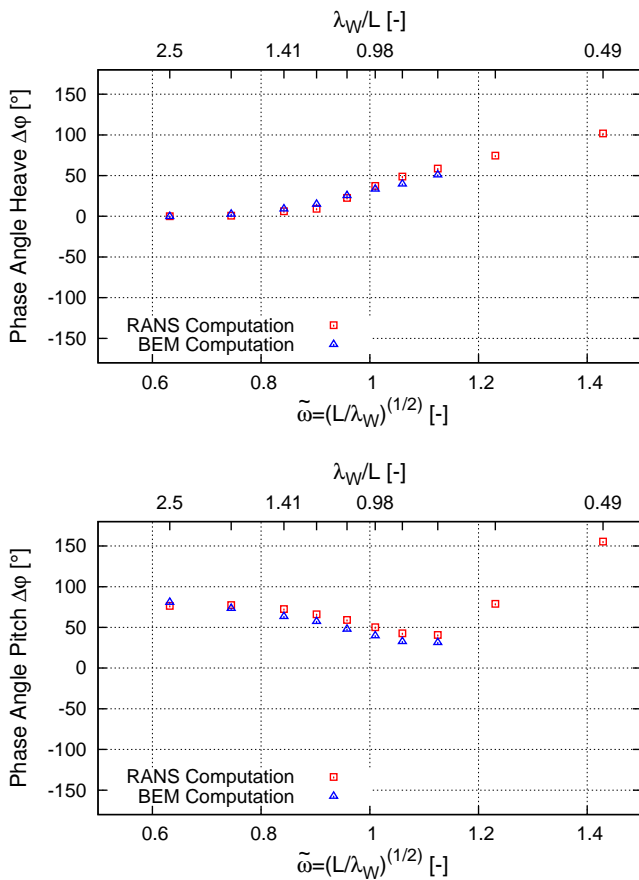


Figure 35: Computed and measured phase angles of heave and pitch motions in regular head waves for the Cruise Ship at **$F_n = 0.159$**

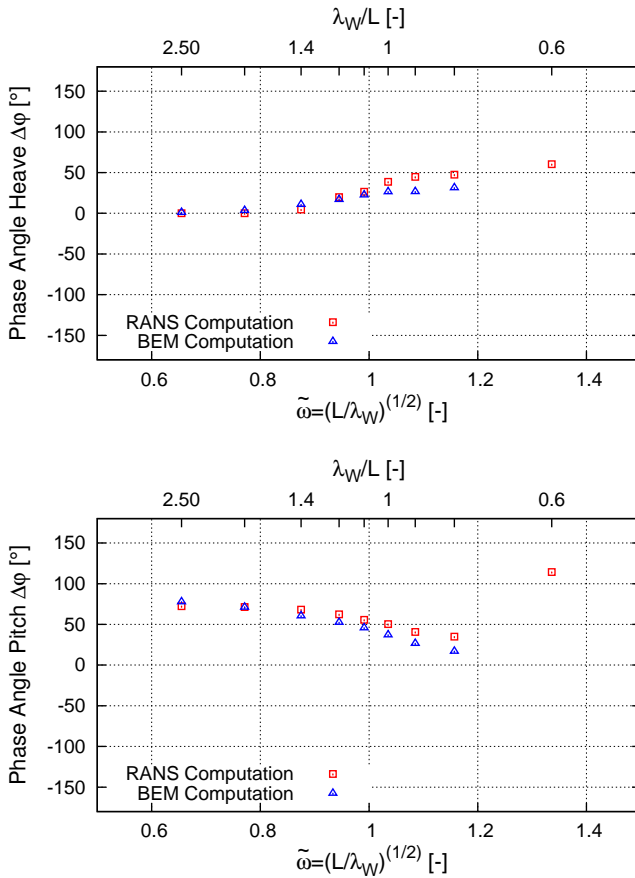


Figure 36: Computed and measured phase angles of heave and pitch motions in regular head waves for the Containership DTC at $\mathbf{Fn} = 0.139$

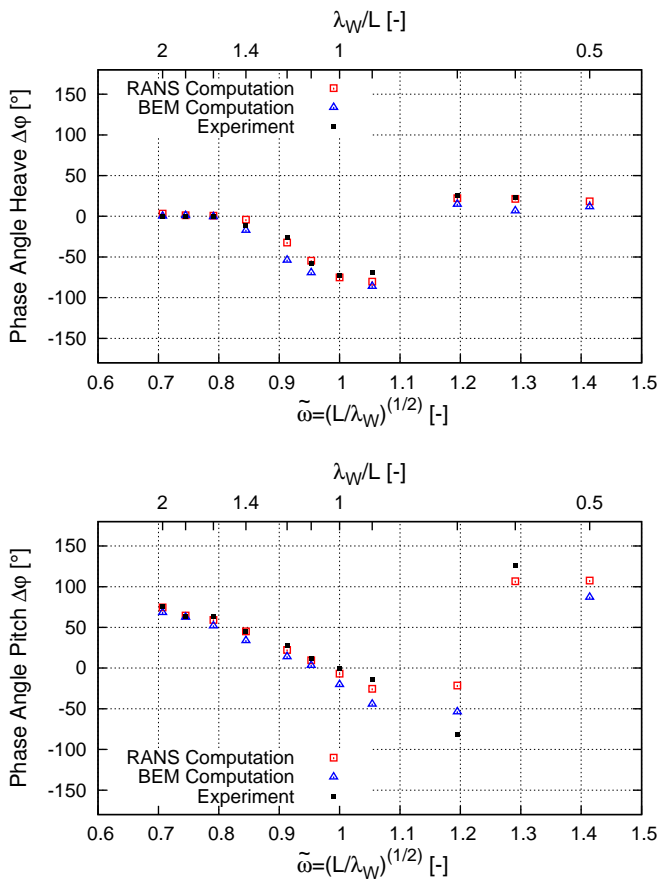
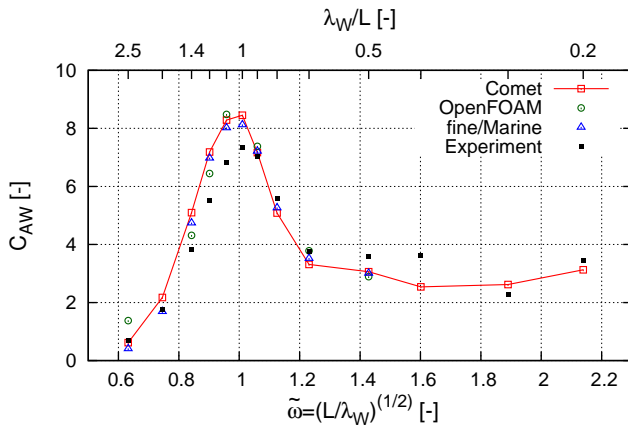
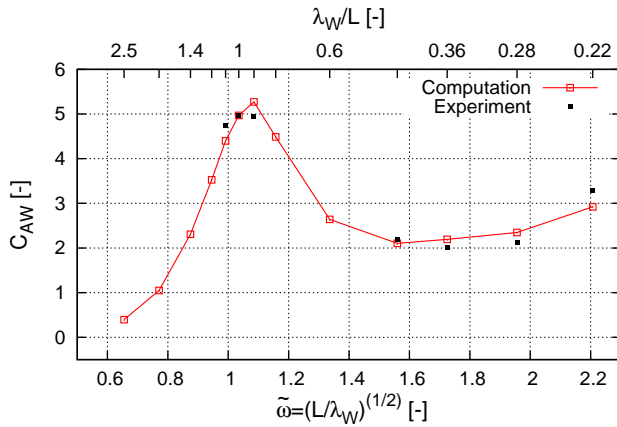


Figure 37: Computed and measured phase angles of heave and pitch motions in regular head waves for the Tanker KVLCC2 at $\mathbf{Fn} = 0.142$

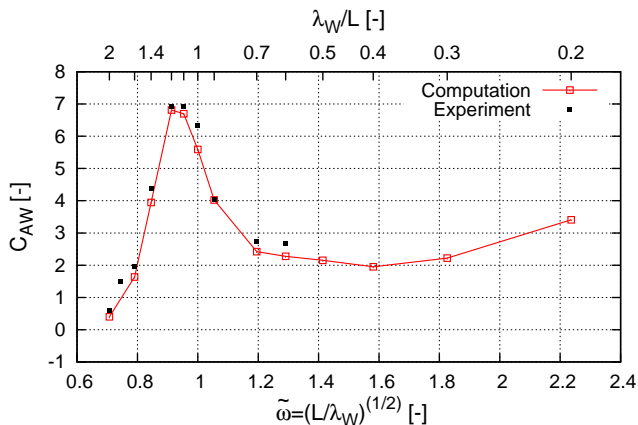


(a) Cruise Ship

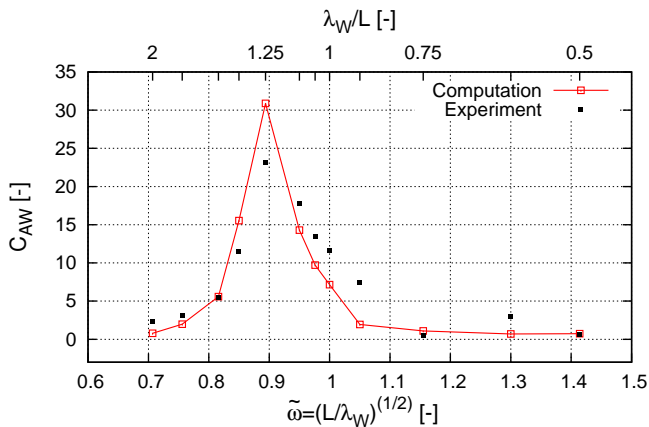


(b) Containership DTC

Figure 38: Computed and measured wave-added resistance coefficients in regular head waves for the Cruise Ship at $\mathbf{Fn} = 0.223$ and the Containership DTC at $\mathbf{Fn} = 0.139$



(a) Tanker KVLCC2



(b) Wigley Hull

Figure 39: Computed and measured wave-added resistance coefficients in regular head waves for the Tanker KVLCC2 at $\mathbf{Fn} = 0.142$ and the Wigley Hull III at $\mathbf{Fn} = 0.30$

Figure 40 compares the wave-added resistance coefficients of three investigated ship types at similar Froude numbers. For the two slender ships (cruise ship and containership), the wave-added resistance in short waves is similar. For the tanker (characterized by a relatively large block coefficient), the wave-added resistance (coefficient) increases in shorter waves, and its peak value shifts towards longer waves.

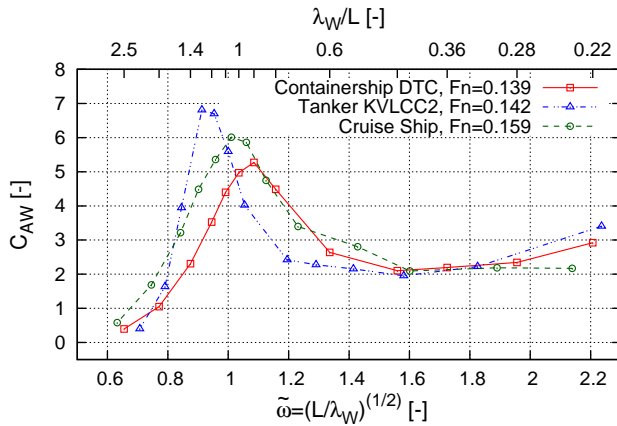


Figure 40: Comparative computed wave-added resistance coefficients for the Cruise Ship at $\mathbf{Fn} = 0.159$, the Containership DTC at $\mathbf{Fn} = 0.139$ and the Tanker KVLCC2 at $\mathbf{Fn} = 0.142$

5.2.2 Effects of Ship Speed on the Wave-Added Resistance

To investigate effects of ship speed on the wave-added resistance, heave and pitch motion and the wave-added resistance were computed at various forward speeds, albeit only for the cruise ship and the containership. For the cruise ship, computations were performed at full-scale speeds of 15 kts and 21 kts, corresponding to Froude numbers of 0.159 and 0.223, respectively; for the containership, at 6 kts and 16 kts, corresponding to Froude numbers of 0.052 and 0.139, respectively.

The comparative response amplitude operators of heave and pitch amplitudes shown in figures 41 and 42 demonstrate the generally fair agreement between computations and measurements. It is seen that pitch motions are nearly unaffected by ship speed. In contrast, with heave motions in the range of wave length equal to ship length, this is not the case. Here, heave motions are distinctly less at slower ship speeds.

This is reflected by the associated wave-added resistance coefficients for these two ships presented in figure 43. As expected, at slower ship speeds the wave-added resistance is less. This effect is more pronounced at peak values of the wave-added resistance coefficient and in long waves, where radiation is dominant. In short waves, where diffraction is dominant, the effect of ship speed on the wave-added resistance is moderate.

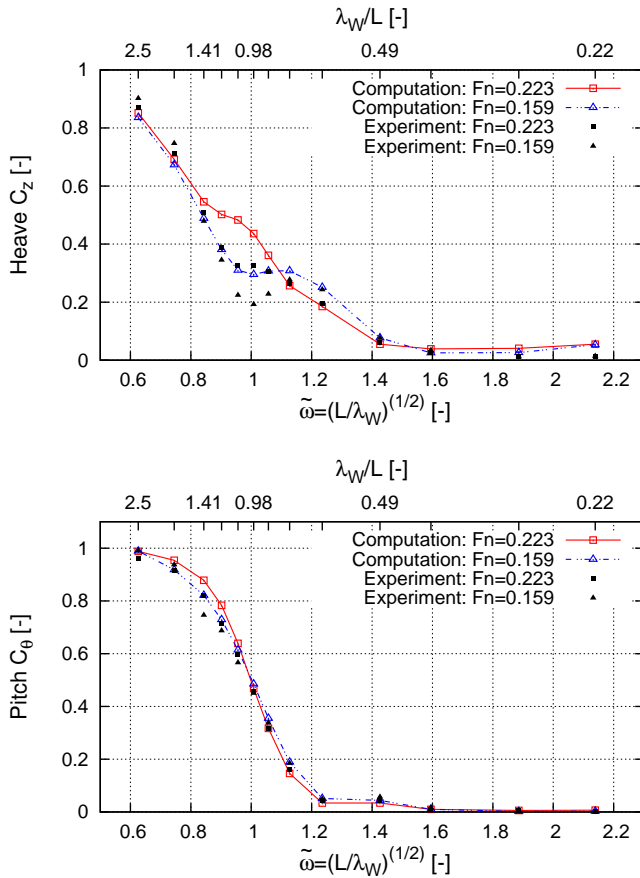


Figure 41: Response amplitude operators of computed and measured heave and pitch motions for the Cruise Ship advancing at two different ship speeds in regular head waves

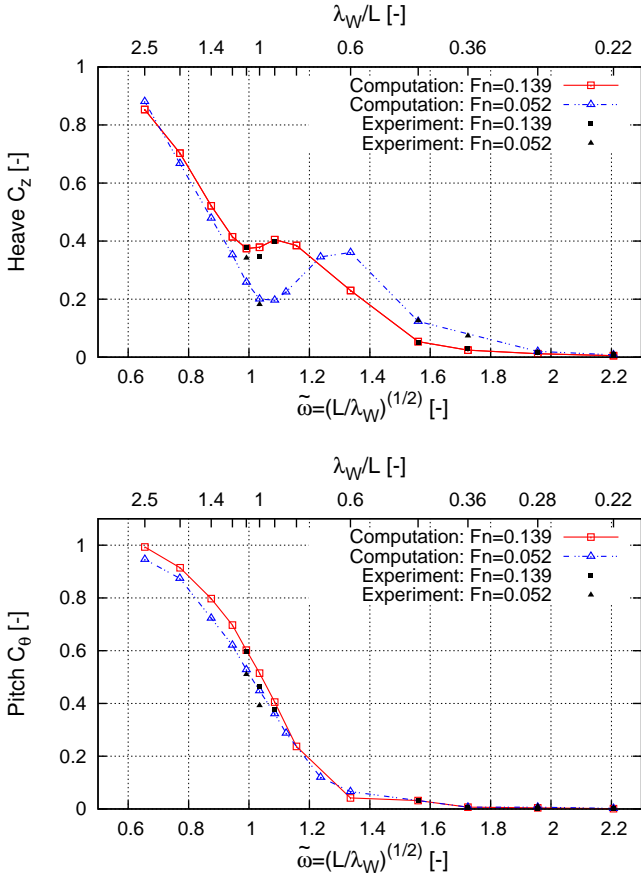
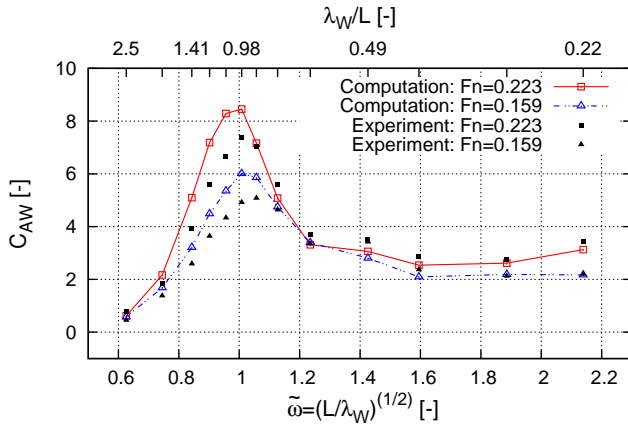
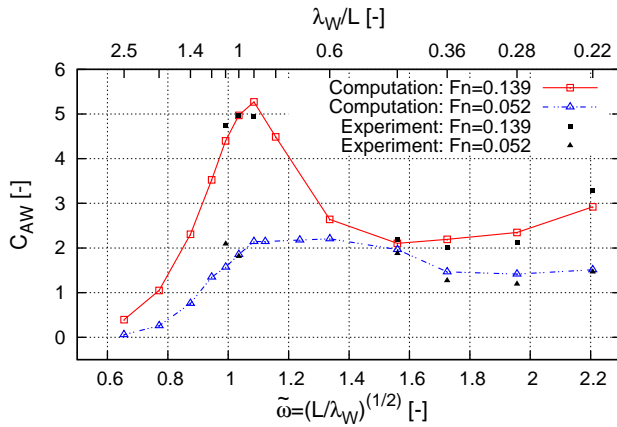


Figure 42: Response amplitude operators of computed and measured heave and pitch motions for the Containership DTC advancing at two different ship speeds in regular head waves



(a) Cruise Ship



(b) Containership DTC

Figure 43: Comparative computed and measured wave-added resistance coefficients for the Cruise Ship and the Containership DTC advancing at two different ship speeds in regular head waves

5.2.3 Effects of Viscosity on the Wave-Added Resistance

It is assumed that the wave-added resistance is driven by pressure forces and hence can be extrapolated using Froude similarity (Söding, 1982). Traditional methods such as physical tests and potential theory based methods are hardly suitable to investigate the frictional wave-added resistance. In the present work the frictional-added resistance was determined by subtracting the calm water friction force from the mean friction force in waves. Figures 44 - 46 present time histories of the longitudinal friction force of the cruise ship and the tanker in a short, intermediate and long waves. Furthermore the average longitudinal friction force in waves and the calm water friction force are included. The oscillation amplitudes of the friction force are relatively small compared to those of the total force (see figure 27). However, significant differences between mean friction force in waves and calm water friction force are obvious.

Figures 47 and 48 show computed and measured total wave-added resistance together with the computed frictional component of the wave-added resistance, including its percentage of the total wave-added resistance for all investigated ships. The non-dimensional frictional wave-added resistance increases with decreasing wave lengths. At their peaks, the frictional part contributes about 5% to total wave-added resistance in waves. In short waves (e.g., $\lambda_w/L = 0.2$), the frictional part exceeds 20% of the total value.

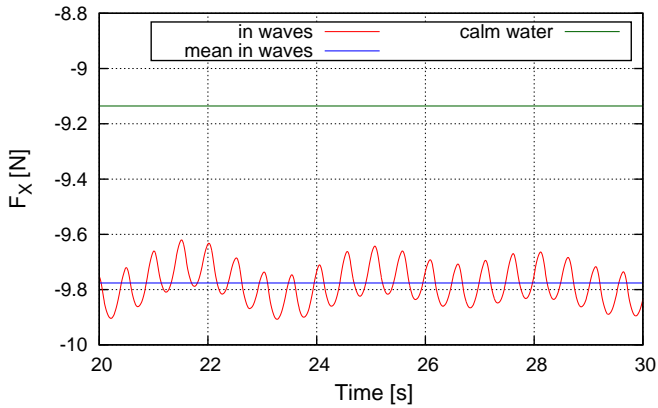
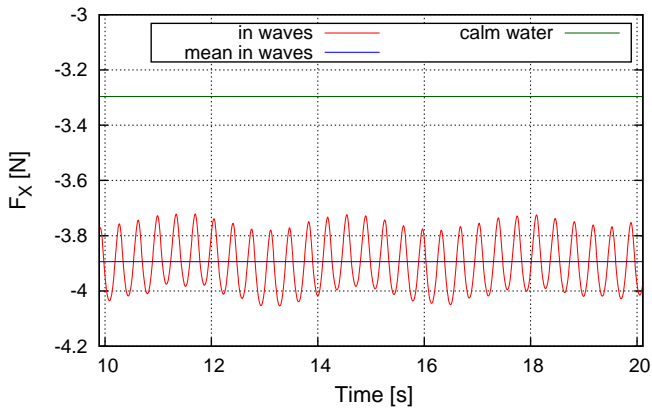
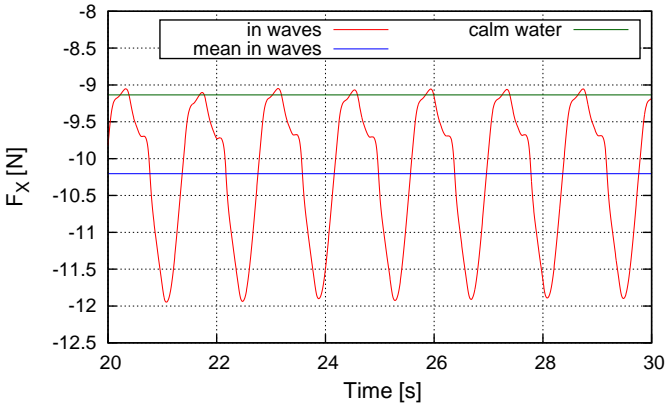
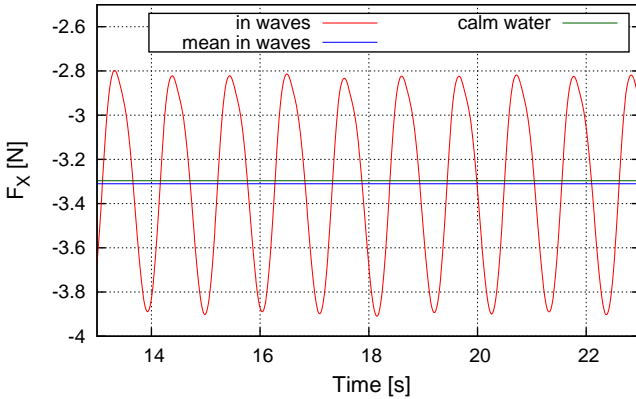
(a) Containership DTC, $\lambda_w/L = 0.22$ (b) Tanker KVLCC2, $\lambda_w/L = 0.22$

Figure 44: Computed time histories, mean and calm water values of friction force for the Containership DTC at $\mathbf{Fn} = 0.139$ and $\mathbf{Re} = 6.1 \cdot 10^6$ and the Tanker KVLCC2 at $\mathbf{Fn} = 0.142$ and $\mathbf{Re} = 2.5 \cdot 10^6$ in short waves



(a) Containership DTC, $\lambda_w/L = 1.0$



(b) Tanker KVLCC2, $\lambda_w/L = 1.0$

Figure 45: Computed time histories, mean and calm water values of friction force for the Containership DTC at $\mathbf{Fn} = 0.139$ and $\mathbf{Re} = 6.1 \cdot 10^6$ and the Tanker KVLCC2 at $\mathbf{Fn} = 0.142$ and $\mathbf{Re} = 2.5 \cdot 10^6$ in intermediately long waves

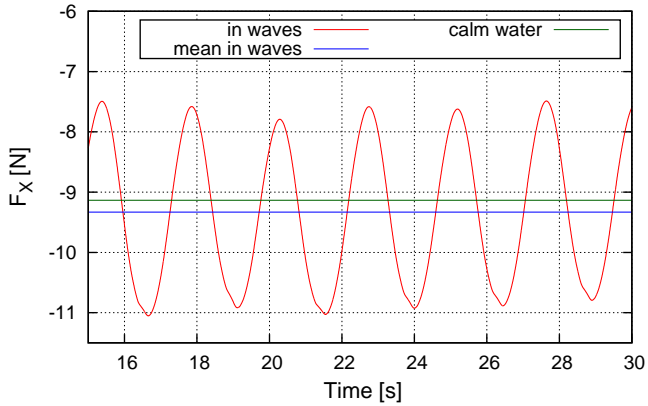
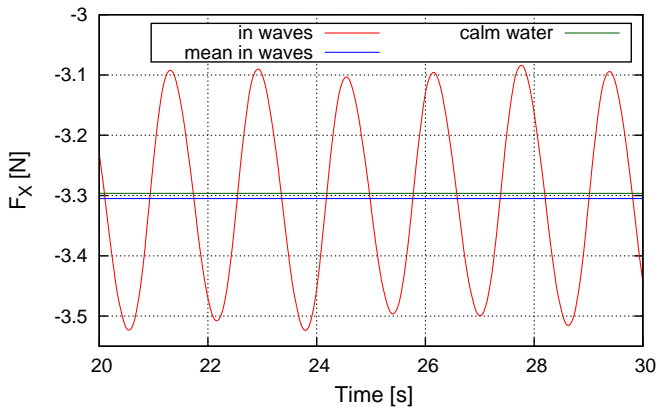
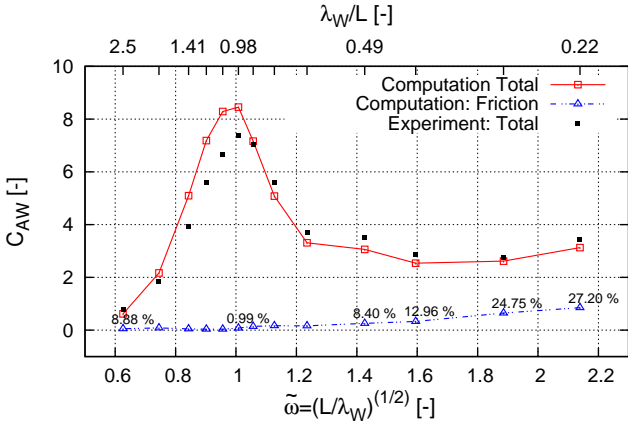
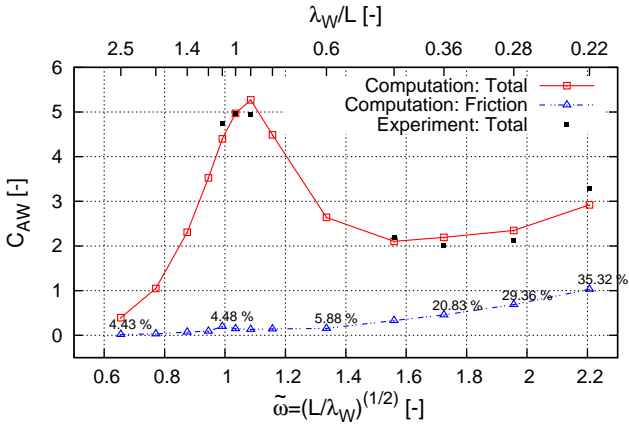
(a) Containership DTC, $\lambda_w/L = 2.5$ (b) Tanker KVLCC2, $\lambda_w/L = 2.8$

Figure 46: Computed time histories, mean and calm water values of friction force for the Containership DTC at $\mathbf{Fn} = 0.139$ and $\mathbf{Re} = 6.1 \cdot 10^6$ and the Tanker KVLCC2 at $\mathbf{Fn} = 0.142$ and $\mathbf{Re} = 2.5 \cdot 10^6$ in long waves

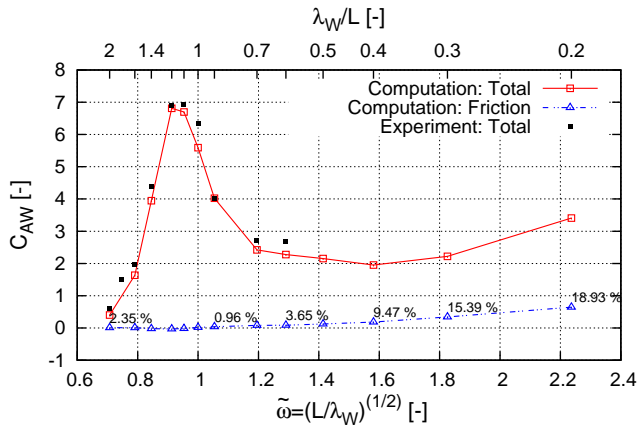


(a) Cruise Ship

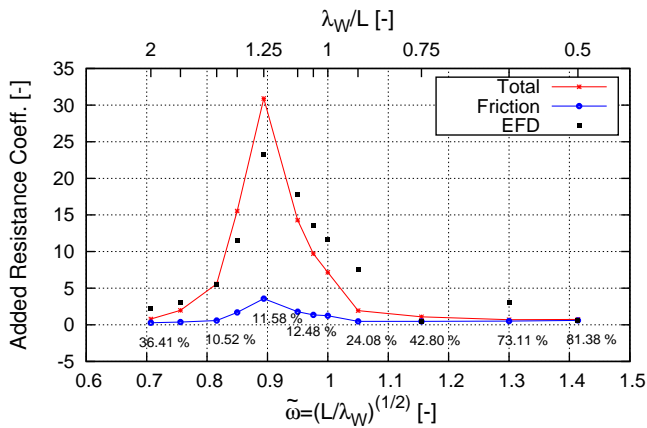


(b) Containership DTC

Figure 47: Computed and measured coefficients of total (red) and frictional (blue) wave-added resistance for the Cruise Ship at $\mathbf{Fn} = 0.223$ and the Containership DTC at $\mathbf{Fn} = 0.139$ in regular head waves



(a) Tanker KVLCC2



(b) Wigley Hull

Figure 48: Computed and measured coefficients of total (red) and frictional (blue) wave-added resistance for the Tanker KVLCC2 at $\mathbf{Fn} = 0.142$ and the Wigley Hull III at $\mathbf{Fn} = 0.30$ in regular head waves

To better understand these results, computed representative shear stress distributions on the hulls of the containership and tanker advancing at constant forward speed in calm water and in waves are shown in figure 49. Total shear force in the picture is almost equal to the mean shear force in waves. The orbital velocities in waves caused the molecular and turbulent shear stresses to increase and led to higher frictional forces acting on the wetted hulls. High shear stresses, marked by dark areas in figure 49, are noticeable underneath the wave crests. Beyond that, the viscous pressure distribution in waves may contribute. However, we did not investigate this phenomenon, because it was impossible to readily separate viscous and wave-induced pressures.

As mentioned above, all computations so far were performed at model scale. However, viscous effects depend strongly on the Reynolds number; therefore, we performed computations in short waves with full-scale Reynolds numbers and a mean dimensionless wall distance of $y^+ = 1000$.

Figure 50 shows computed and measured coefficients of total and frictional wave-added resistance at model scale (MS) and full scale (FS) of the containership at $Fn = 0.14$ in regular head waves. As expected, the frictional wave-added resistance is smaller at full scale than at model scale. Its contribution is roughly halved compared to model scale. Consequently, the frictional component of the wave-added resistance is overestimated when predictions are performed at model scale. Nevertheless, this component is still significant and should not be neglected.

At this stage, it can be noted that in short waves, the total amount of the wave-added resistance is relatively small (in some instances, it only amounts to a few percent of calm water resistance for a ship at service speed). That is, in waves the viscous part of the wave-added resistance may not contribute substantially in the total resistance (calm water and wave-added resistance). Nevertheless, these viscous effects may still be useful, e.g., to correct the more efficient potential theory based wave-added resistance predictions.

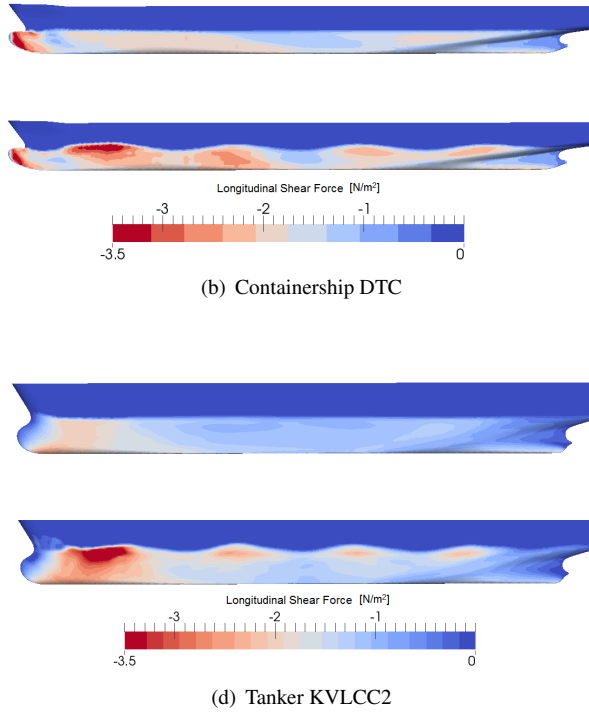


Figure 49: Representative shear stress distributions in calm water (upper hull) and in regular head waves (lower hull) for the Containership DTC at $\mathbf{Fn} = 0.139$ and $\mathbf{Re} = 6.1 \cdot 10^6$ and the Tanker KVLCC2 at $\mathbf{Fn} = 0.142$ and $\mathbf{Re} = 2.5 \cdot 10^6$

5.2.4 Effects of Wave Steepness on the Wave-Added Resistance

In linear regime, the wave-added resistance depends quadratically on wave height (Söding, 1982). However, ships also operate in nonlinear waves of variable steepness. Thus, the question arose in what way this dependency is also valid in nonlinear regime. To address this issue, the wave-added resistance was computed for the cruise ship, the containership, and the tanker in waves of different steepness, defined as wave height divided by wave length.

For these two ships advancing in head waves of different steepness, figures 51 and 52 plot the results, together with experimental measurements, in terms of wave-added resistance coefficients against wave length and normalized wave frequency. For the cases investigated, a distinct dependence of the wave-added resistance on wave steepness can be observed. At their peaks, the wave-added resistance coefficients decrease with increasing wave steepness. In this range of wave lengths radiation is dominant, and nonlinear effects are moderate. In short waves nonlinear effects are important, and diffraction is dominant.

The distinct influence of wave steepness on the added resistance coefficient becomes noticeable in wave lengths that are shorter than one-half ship length ($\lambda_W/L < 0.5$); that is, as waves get shorter, the influence of wave steepness increases. The slope of the wave-added resistance coefficient as wave frequency increases gets distinctly larger with greater wave steepness. The influence of wave steepness on the wave-added resistance is more pronounced for the full-bodied tanker than for the relatively slender containership. In wave lengths of $\lambda_W/L < 0.28$, increasing the wave steepness from 2.1% to 3.5% causes a 35.2% increase in the wave-added resistance coefficient for the containership. In waves of this same length (e.g., when $\lambda_W/L < 0.28$), increasing the wave steepness from 0.6% to 1.9% causes a 201% increase in the wave-added resistance coefficient for the tanker.

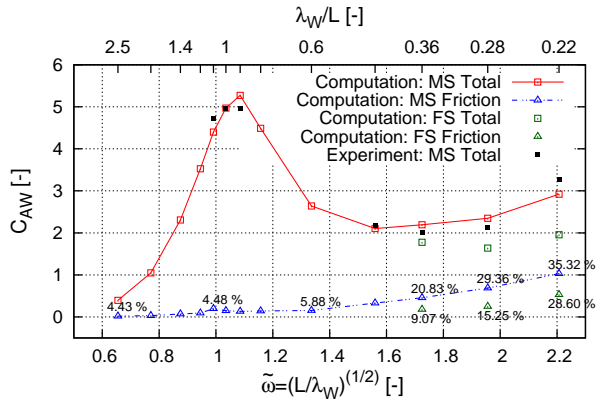


Figure 50: Total and frictional wave-added resistance coefficients at $Re = 6.1 \cdot 10^6$ and $Re = 2.9 \cdot 10^9$ (full scale) of the Containership DTC at $Fn = 0.139$ in regular head waves

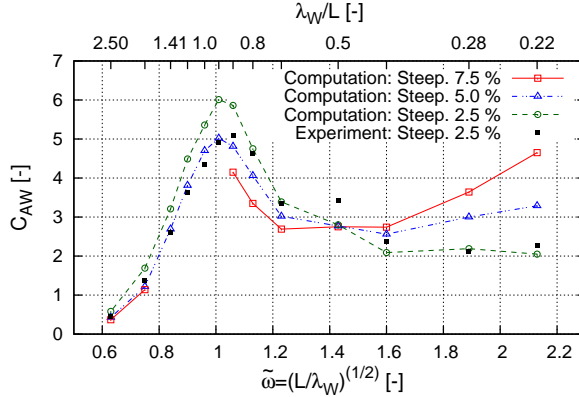


Figure 51: Computed and measured wave-added resistance coefficients in regular head waves of different steepness for the Cruise Ship at $Fn = 0.223$

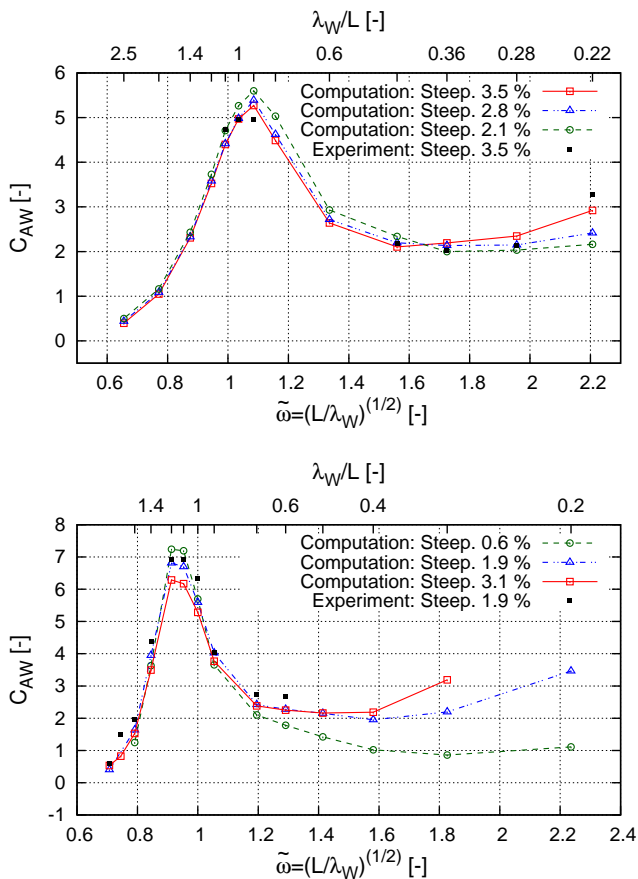


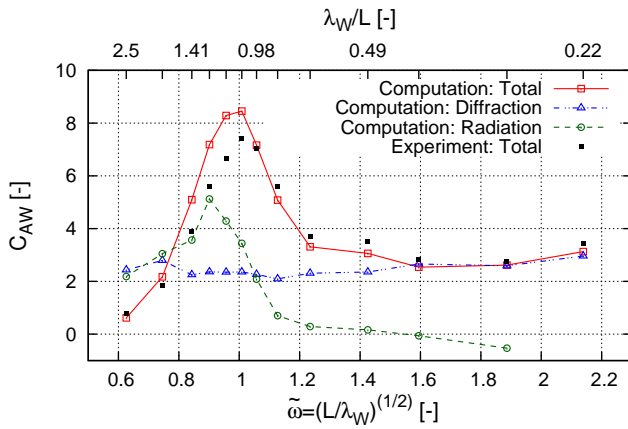
Figure 52: Computed and measured wave-added resistance coefficients in regular head waves of different steepness for the Tanker KVLCC2 at $F_n = 0.142$ for the Containership DTC at $F_n = 0.139$

An experimental study performed by Yasukawa et al. (2016) shows similar trends. Most of the literature dealing with computational and experimental investigations of the wave-added resistance does not specify wave steepness, and one aim of this work was to demonstrate its importance. In this regard, a comparison between computations and experimental measurements of the wave-added resistance, especially for ships advancing in short waves, is meaningful only for waves of the same wave steepness.

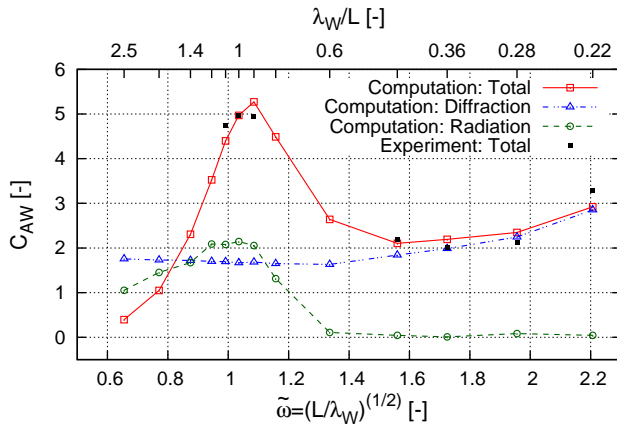
5.2.5 Interaction between Radiation and Diffraction Forces

In the current work, the interaction between radiation and diffraction in non-linear regime was investigated. To quantify these interactions, diffraction and radiation forces were determined separately for the four investigated ship types. To this end, three different computations were performed. First, the total wave-added resistance was computed. Second, the resistance of the fixed ships advancing with constant forward speed in incoming head waves (diffraction) was determined. Third, the resistance of the moving ships advancing in calm water was determined by prescribing the computed motions obtained in the first step (radiation).

Figures 53 and 54 plot computed and measured total wave-added resistance as well as the associated computed radiation and diffraction forces against wave length to ship length ratios as well as against normalized wave frequencies. Although interaction between radiation and diffraction is more pronounced in long waves, it vanished almost completely in short waves, as was expected. In long waves (e.g., when $\lambda_W/L > 1$) the radiation part of the wave-added resistance becomes significant, and the diffraction part is only moderately influenced by waves. Nevertheless, interaction between radiation and diffraction is important. In short waves (e.g., when $\lambda_W/L < 0.50$) radiation forces are nearly zero, and diffraction forces depend only moderately on wave frequency. Thus, in short waves diffraction forces match the total wave-added resistance. Consequently, the radiation part of the wave-added resistance coefficients display a significant peak in the range of large motion response (e.g., when $\lambda_W = L$). These findings were found to be valid for all ships at all Froude numbers. The interaction between radiation and diffraction was also addressed and discussed by Kashiwagi et al. (2010).

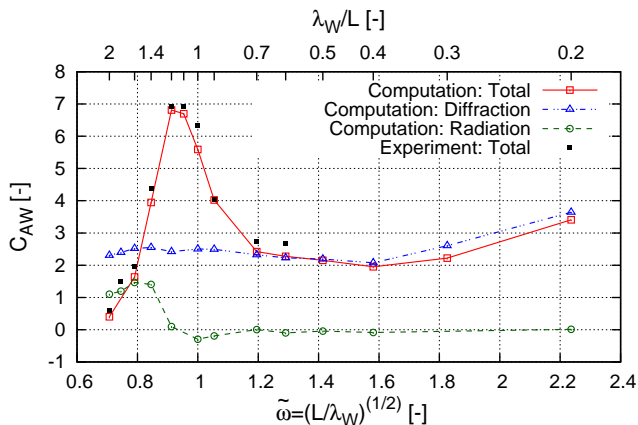


(a) Cruise Ship

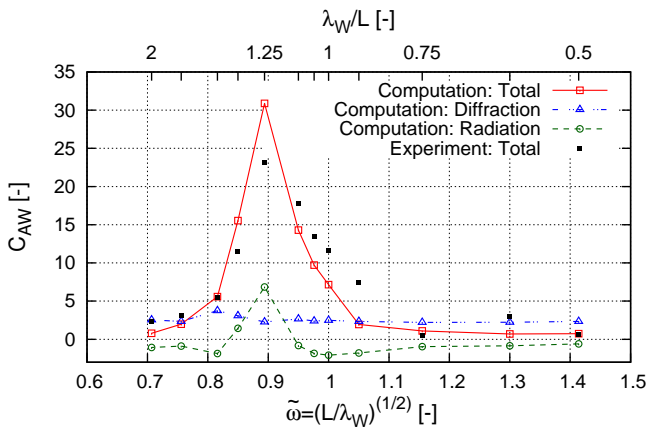


(b) Containership DTC

Figure 53: Coefficients of total wave-added resistance (solid), diffraction force (dotted line) and radiation force (dashed line) for the Cruise Ship at $\mathbf{Fn} = 0.223$, the Containership DTC at $\mathbf{Fn} = 0.139$



(a) Tanker KVLCC2



(b) Wigley Hull

Figure 54: Coefficients of total wave-added resistance (solid), diffraction force (dotted line) and radiation force (dashed line) for the Tanker KVLCC2 at $\mathbf{Fn} = 0.139$ and the Wigley Hull III at $\mathbf{Fn} = 0.30$

5.2.6 Influence of Encounter Angle on the Wave-Added Resistance

To investigate the influence of the encounter angle on the wave-added resistance computations of the cruise ship in oblique waves were performed. Thereby, encounter angles of $\mu = 180^\circ, 150^\circ, 120^\circ$ and 90° were considered. In the model tests, springs were used to enable first order oscillation motions in six degree of freedom while simultaneously restricting drift motions, see Valanto and Hong (2015). In the computations the model was only free to heave, pitch, and roll. Yaw, surge and sway were suppressed. Springs or other arrangements to keep the model in position were thus not necessary. That significantly reduces the computational effort. The complete fluid domain was discretized because no symmetry could be exploited. Grid and boundary conditions were adapted accordingly. A numerical grid and representative free surface elevation of a computation with oblique waves are shown in figure 55.

Figures 56 shows the transfer functions of heave, pitch and roll at an encounter angle of 150° . Computed heave and pitch amplitudes show fair agreement with model test data. As seen earlier, computed heave amplitudes are slightly overestimated in the computation. Roll amplitudes are generally under predicted in the computations, which may be caused by the restriction of the yaw motion in the computation.

The quadratic transfer functions of the wave-added resistance are shown in figures 57 and 58. Wave-added resistances coefficients in the peak range are of the same magnitude for $\mu = 180^\circ, 150^\circ$ and 120° . However, the peaks are shifted toward higher frequencies due to decreasing encounter frequencies. The response amplitude operators for $\mu = 90^\circ$ show no peak in the considered range of wave lengths. In general, fair agreement between the computation and experiment is achieved even though different motion setups were used in the computations and tests.

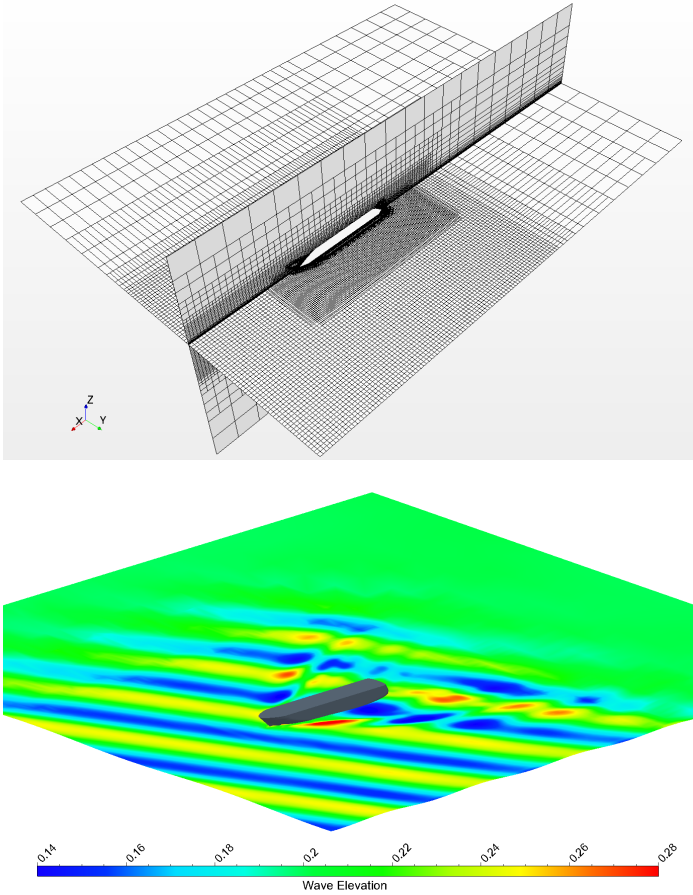


Figure 55: Numerical grid used for oblique wave computations (top) and wave pattern of the Cruise Ship at $\mathbf{Fn} = 0.159$, $\lambda_{\mathbf{W}}/\mathbf{L} = 1.09$ and $\mu = 150^\circ$ (bottom)

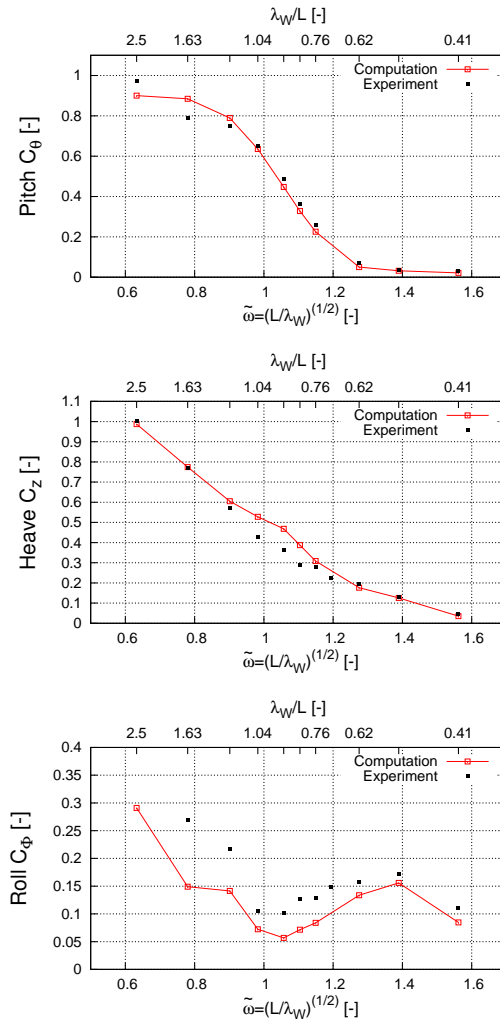
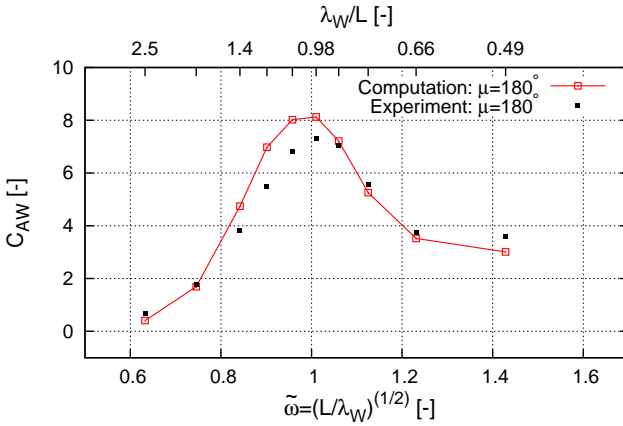
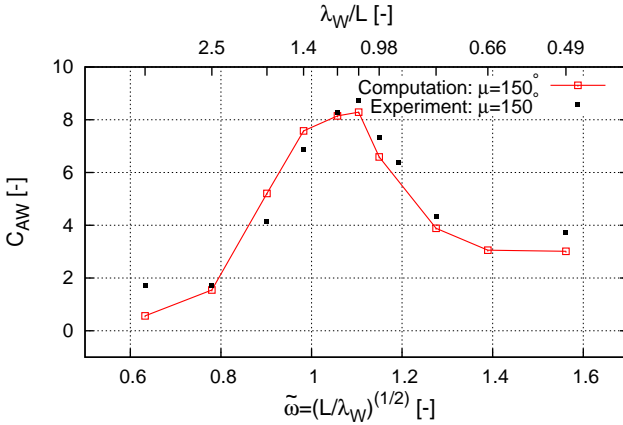


Figure 56: Computed and measured RAOs of heave, pitch and roll amplitudes in regular oblique waves for the Cruise Ship at $\mathbf{Fn} = 0.159$ and $\mu = 150^\circ$



(a) Encounter Angle $\mu = 180^\circ$



(b) Encounter Angle $\mu = 150^\circ$

Figure 57: Computed and measured wave-added resistance coefficients in regular oblique waves for the Cruise Ship at $\mathbf{Fn} = 0.159$

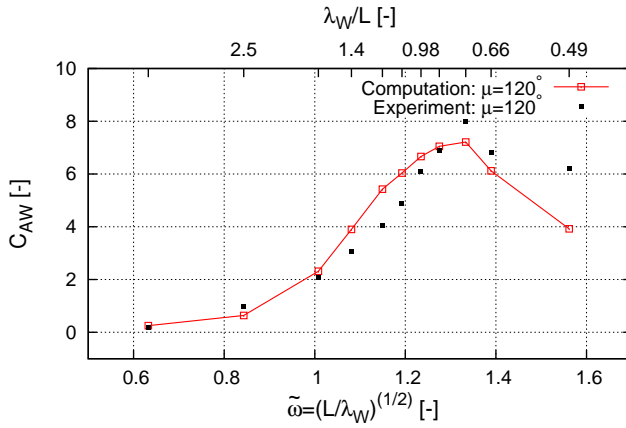
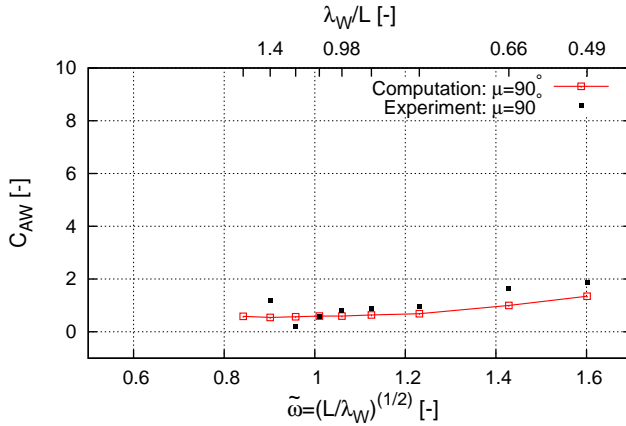
(a) Encounter Angle $\mu = 120^\circ$ (b) Encounter Angle $\mu = 90^\circ$

Figure 58: Computed and measured wave-added resistance coefficients in regular oblique waves for the Cruise Ship at $\mathbf{Fn} = 0.159$

5.3 Conclusions

Predicting the wave-added resistance of ships remains a challenge. Nevertheless, the practical relevance of this subject motivated systematic investigations in the use of advanced numerical methods to analyze the wave-added resistance of ships.

Initially, discretization errors were investigated. Then, based on the outcome, spatial and time-dependent discretizations suitable for simulations were identified. Furthermore, appropriate numerical methods to predict the wave-added resistance were introduced. Two findings were important. On the one hand, computations of the calm water resistance and the wave-added resistance in waves should be conducted on the same numerical grid. On the other hand, the wave-added resistance should always be normalized against the actual wave amplitude, not the targeted wave amplitude.

Ship motions and the wave-added resistance were computed for the four ship types and compared to the experimental model test measurements. In general, the computations and measurements correlated favorably. This was also the case for the wave-added resistances in short and long waves, thereby demonstrating that the methods based on solving the Reynolds-averaged Navier-Stokes equations were capable of predicting reliable wave-induced first- and higher-order responses, such as ship motions and the wave-added resistance, respectively. The results showed that radiation forces were affected more strongly by ship speed than diffraction forces. Thus, peaks of the wave-added resistance coefficients were less pronounced at lower ship speeds.

By subtracting the frictional resistance in calm water from the frictional resistance in waves, the frictional wave-added resistance was determined. The computations showed that, in short waves, friction accounted for a significant part of the total wave-added resistance, namely, 20% or even more. However, full-scale computations showed that this effect was less pronounced at full scale.

Diffraction and radiation forces at different frequencies were investigated, where diffraction forces were obtained by restraining the ship in waves and the radiation forces were obtained by prescribing the motions of the ship in calm water. In long waves, the sum of diffraction and radiation forces did

not match the total resistance, i.e., the interaction of these two force components had to be accounted for. In short waves, the diffraction part of the total resistance was dominant as almost no ship motions were induced.

Generally, the assumption of a quadratic correlation between wave height and the wave-added resistance was confirmed for ships advancing in waves of moderate to long wave lengths (almost linear). However, this assumption did not hold for ships advancing in short waves because diffraction was dominant in short waves and nonlinear effects are pronounced.

The computed wave-added resistances in oblique waves considering only heave, pitch, and roll motions showed fair agreement with measurements also considering surge, sway, and yaw. This does not hold for side force and yaw moment.

6 Nominal Wake Field in Waves

Efficiency and comfort, in terms of vibration and noise, of a ship are significantly influenced by the conditions, a propeller works in: the wake field. Hull design attempts to optimize the nominal wake field to create good operating conditions for the propeller. Consequently, the prediction and optimization of a reasonable wake field are major issues in ship hydrodynamics.

Although wave-induced orbital velocities and ship motions may have a significant influence on the wake field, it is common to consider the wake field only under calm water conditions during the design process. Systematic investigations of the influence of waves on the wake field are still rare. Thus, the influence of waves on the wake field, particularly the axial wake fraction, was investigated here considering both the average and the time histories of the nominal wake fraction in waves. A preliminary study of the influence of the spatial discretization was performed. The numerical methods, settings, boundary conditions and grids presented above were used for the computation of the nominal wake fraction. For detailed information, please refer to section 5.

6.1 Grid Sensitivity Study

Since detailed information of the velocity field is essential to determine the nominal wake fraction, the influence of the spatial discretization in the vicinity of the propeller plane was investigated. Therefore, local refinements around the aft ship were included in the fine grids presented above. The refined aft ships of the containership and resulting wake fields in calm water conditions are shown in figure 59. The nominal wake fractions obtained with the various grid refinements are listed in table 9.

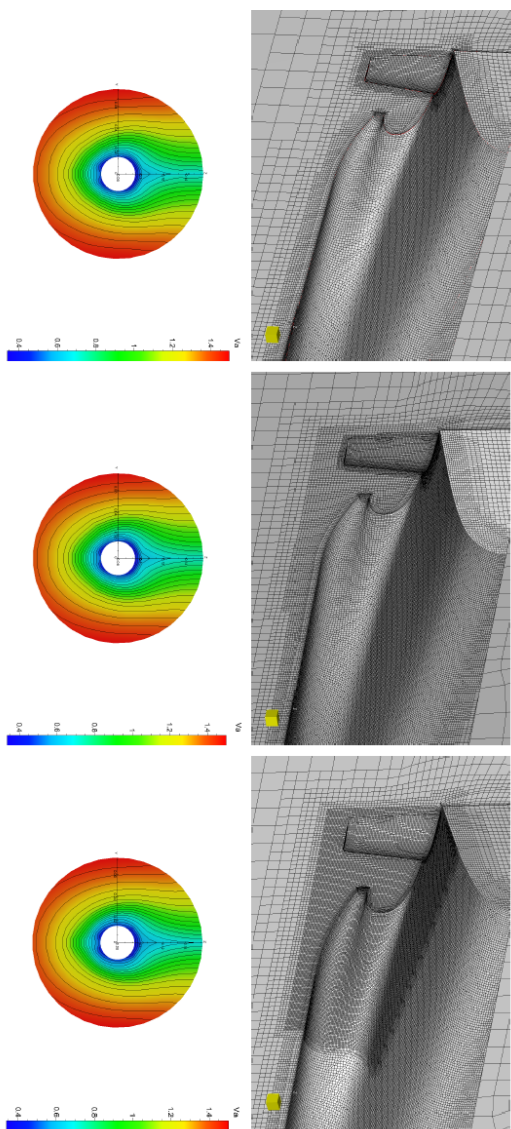


Figure 59: Influence of local refinements on the nominal wake fraction for the Containership DTC at $F_n = 0.139$

Table 9: Containership DTC at $Fn = 0.139$: Influence of local refinements on the computed nominal wake fraction

| | w/o Refinement | 1st Refinement | 2nd Refinement |
|---------------|----------------|----------------|----------------|
| Wake Fraction | 0.314 | 0.321 | 0.323 |

The wake field is nearly unaffected by grid fineness in the aft ship area and the wake fraction changes negligibly when refining the aft ship as presented. Thus, for determining the nominal wake fraction, the fine grids used earlier (section 5) were used.

6.2 Results

To determine the nominal wake fraction in waves, axial velocities defined in ship fixed coordinates were interpolated at 316 points in the propeller plane and averaged. The points were attached to the ship's movement, which was updated every time step. With the averaged axial velocity in the propeller plane and the constant ship speed, the wake fraction was determined with a time step of 0.04 seconds. The mean wake fraction in waves was determined by averaging all wake fractions within one encounter period. With the constant time interval the wake fraction was computed between 12 and 120 times per encounter period, depending on the current wave period.

Figure 60 shows twelve wake fields of the containership within one encounter period at $Fn = 0.218$, $\lambda_W/L = 1.125$, and $h_W = 0.12m$. The colors contours indicate the ratio of the current axial velocity, v_a , and the ship speed, v_s . From examining the series of images, it is obvious that a significant change in the inflow conditions occurs.

To illustrate the pronounced fluctuation of the wake fraction, time histories in short, intermediate and long waves are presented in figures 61 - 63. These graphics also contain time-averaged and calm water values. The time histories extend over one encounter period.

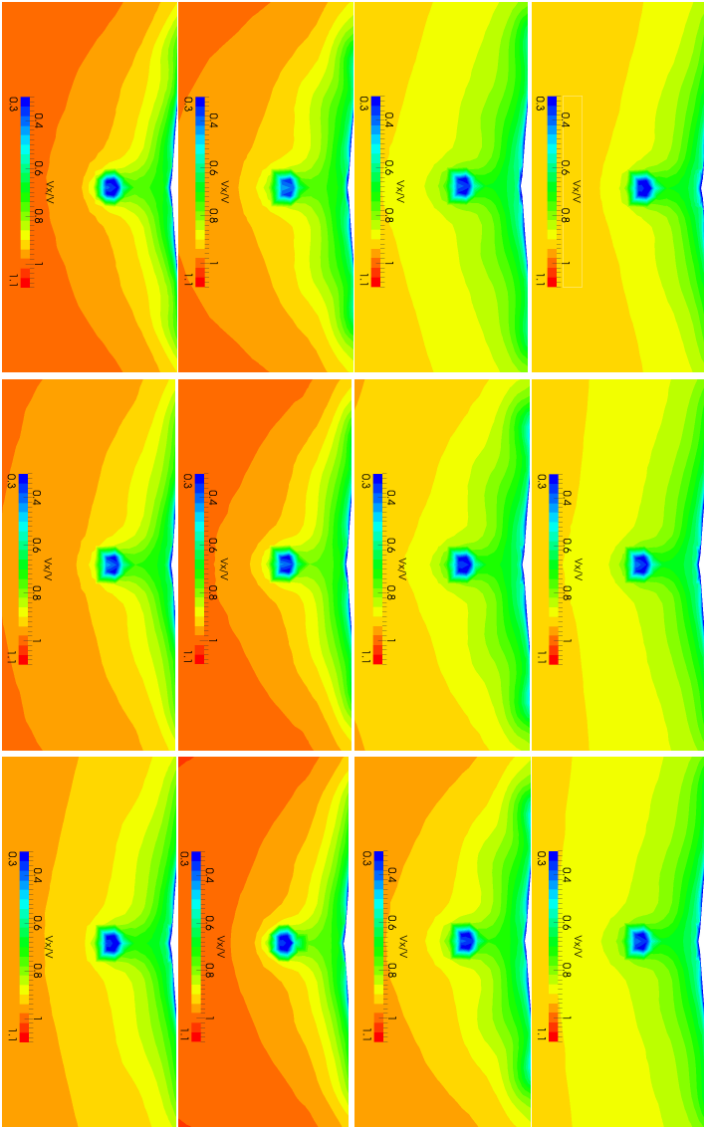


Figure 60: Change in the wake field during one encounter period for the Containership DTC at $F_n = 0.139$

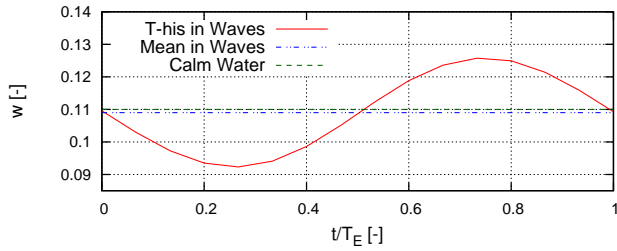
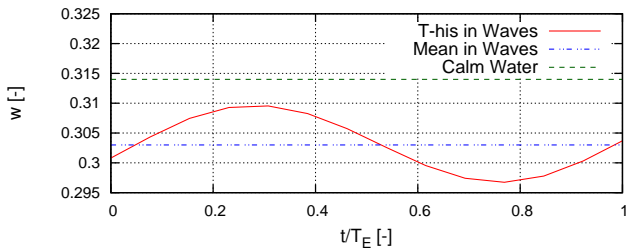
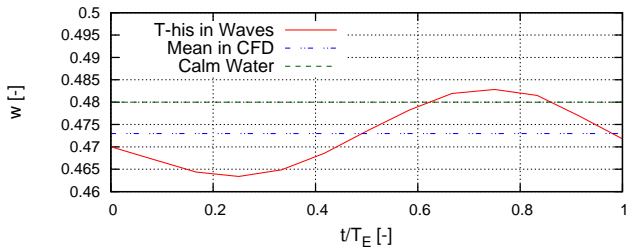
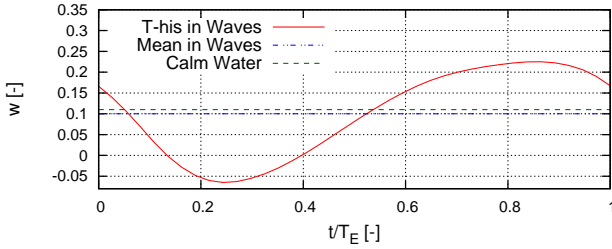
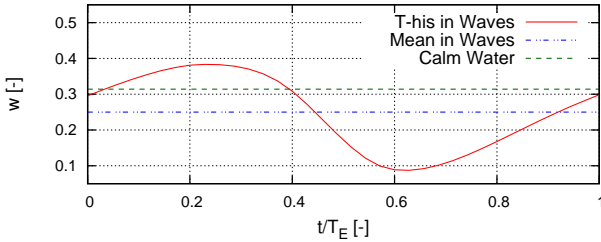
(a) Cruise Ship, $\lambda_W/L = 0.22$ (b) Containership DTC, $\lambda_W/L = 0.28$ (c) Tanker KVLCC2, $\lambda_W/L = 0.2$

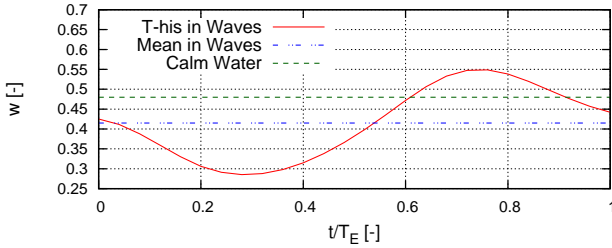
Figure 61: Time histories and time-averaged values of the wake fraction in short waves as well as calm water values for the Cruise Ship at $\mathbf{Fn} = 0.223$, the Containership DTC at $\mathbf{Fn} = 0.139$, and the Tanker KVLCC2 at $\mathbf{Fn} = 0.142$



(a) Cruise Ship, $\lambda_W/L = 0.98$



(b) Containership DTC, $\lambda_W/L = 1.0$



(c) Tanker KVLCC2, $\lambda_W/L = 1.0$

Figure 62: Time histories and averaged values of the wake fraction in medium long waves as well as calm water values for the Cruise Ship at $F_n = 0.223$, the Containership DTC at $F_n = 0.139$, and the Tanker KVLCC2 at $F_n = 0.142$

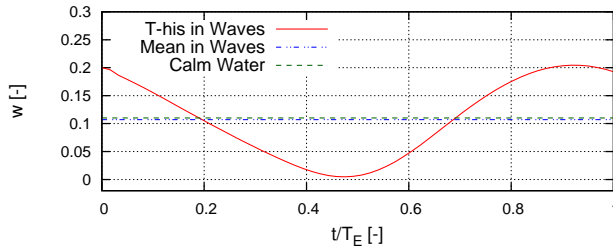
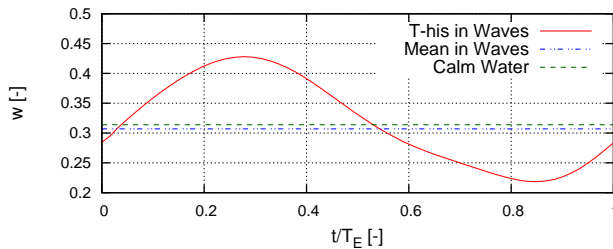
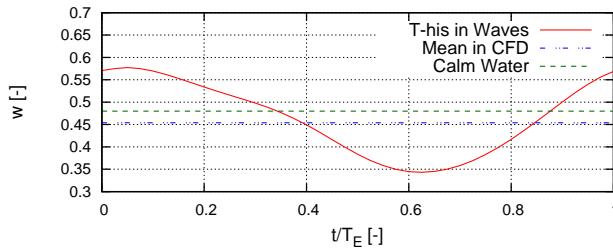
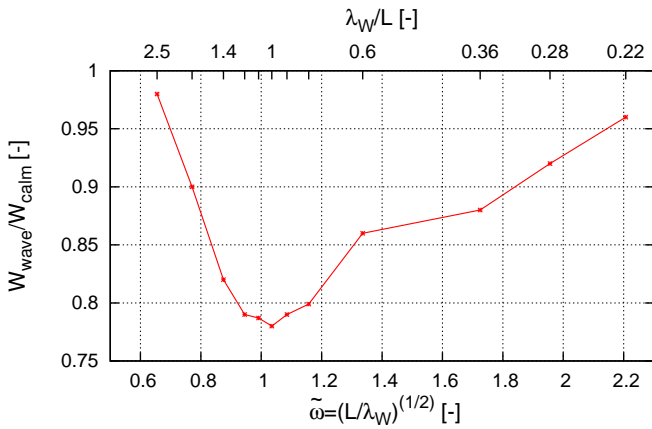
(a) Cruise Ship, $\lambda_W/L = 2.5$ (b) Containership DTC, $\lambda_W/L = 2.5$ (c) Tanker KVLCC2, $\lambda_W/L = 2.0$

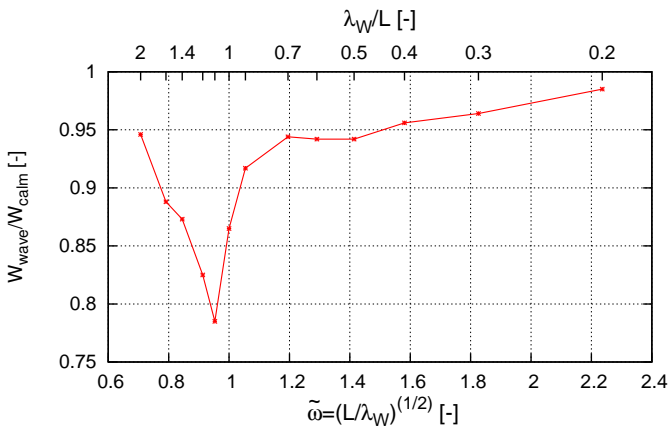
Figure 63: Time histories and averaged values of the wake fraction in long waves as well as calm water values for the Cruise Ship at $\mathbf{Fn} = 0.223$, the Containership DTC at $\mathbf{Fn} = 0.139$, and the Tanker KVLCC2 at $\mathbf{Fn} = 0.142$

In all cases, the wake fraction oscillates with the encounter frequency and time histories have considerable amplitudes. The amplitudes change significantly for different wave length. Although, calm water values are completely different for the considered ships, the amplitudes of the time histories are comparable in similar waves. Due to the different mean values, in peak range ($\lambda_W/L \approx 1$) the amplitudes range from 150% of the averaged value for the cruise ship to 25% of the averages value for the tanker. The nominal wake fraction of the cruise ship in regular waves with a length equal to ship length oscillates between -0.06 and 0.225 . Consequently, during one encounter period, the axial inflow velocity oscillates between 106% and 77.5% of the ship speed.

The ratio of the time-averaged nominal wake fraction in waves and the calm water value are plotted against λ_W/L in figures 64 and 65. For all ship types, the nominal wake fraction decreases in waves (which means an acceleration of the inflow velocity). The maximal decrease occurs when the ship's motion is the greatest ($\lambda_W/L \approx 1$). For the cruise ship, in a wave of $\lambda_W/L = 1$, the wake fraction presents 86.1% of the calm water value, whereas for the single-screw container ship and tanker, the lowest wake fraction is $\approx 78\%$ of the calm water value. Regarding the time averaged values, there appears to be a relation between the influence of waves on the nominal wake fraction and the calm water wake fraction: the lower the calm water wake fraction is, the less is the influence of waves on the time-averaged wake fraction in waves. However, this assumption needs to be proven by considering far more ships.



(a) Containership DTC



(b) Tanker KVLCC2

Figure 64: Ratio of wake fraction in calm water and in waves against dimensionless wave frequency for the Containership DTC at $\mathbf{Fn} = 0.139$ and the Tanker KVLCC2 at $\mathbf{Fn} = 0.142$

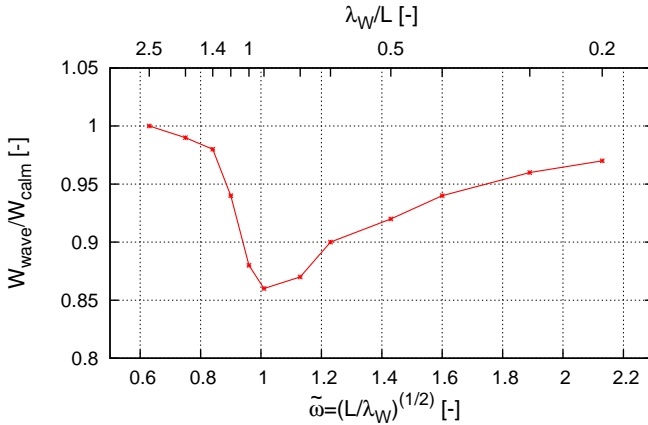


Figure 65: Ratio of wake fraction in calm water and in waves against dimensionless wave frequency for the Cruise Ship at **Fn = 0.223**

6.3 Conclusion

In general, RANS methods are well-suited to investigate the wake field of a ship in waves. The nominal wake fraction has been determined for three different ship types in twelve different wave length ranging from 0.2 to 2 times the ship length. The time-averaged nominal wake fraction decreases in waves. Its change depends on the ship type. The wake fraction of the twin-screw cruise ship was at maximum 13.9%, and the single-screw ships (container ship and tanker) was at most $\approx 22\%$ lower than the according calm water values. In contrast, the oscillation amplitudes of the wake fraction in waves were almost independent of ship type. For all ship types, the amplitudes of the wake fraction time histories due to orbital velocities and ship motions were in the same range. It may be summarized that the change of the time-averaged wake fraction in waves depends on ship’s hull form and the position of the propeller, whereas the oscillation amplitudes of the wake fraction in waves depend on the wave parameters. Furthermore, the amplitudes

of the wake fraction time histories in waves are larger than the changes of the averaged wake fraction. Thus both effects should be taking into account when designing a propeller.

7 Ship Propulsion in Waves

This section presents an investigation of the propulsion characteristics of ships in waves. This investigation focuses on the change of the propulsion characteristics due to waves and ship motion, compared to the calm water values. Initially, the setup and results of all the computations, namely resistance tests, the propeller open water tests, and the propulsion tests are shown. In general, numerical grids and boundary conditions were similar to those used for the computations of the wave-added resistance presented earlier (section 5). To avoid repetition at this point, the resistance computations will be presented only briefly. Then, the propulsion characteristics in waves are shown together with calm water values. Computational results are compared with experimental data. The content of this chapter has been published in Sigmund and el Moctar (2017), partly in exact wording.

7.1 Experimental and Computational Procedure

The investigation was performed using the twin-screw cruise ship and the single-screw containership (see section 4). Calm water towing tank tests for both ships were performed without the propeller(s), but with bilge keels and rudder(s) attached to the hull. Propulsion tests in waves were performed with self-propelled models with propeller(s) turning at a constant rate. A viscous drag component was not deducted for the containership. The propeller(s) thrust and torque, the model's motions as well as the model's speed were measured. For additional details of the experimental setup, see Valanto and Hong (2015), Sprenger, et al. (2016) and el Moctar et al. (2016).

Table 10: Wave parameter and propeller speed in ship scale

| | F_n [-] | λ_W/L_{PP} [-] | h_W [m] | h_W/λ_W [] | n [1/s] |
|---------------|-----------|------------------------|------------|--------------------|-----------|
| | | | Calm Water | | 78.8 |
| Cruise Ship | 0.223 | 0.28 | 1.22 | 0.02 | 79.152 |
| | | 0.39 | 1.70 | 0.02 | 80.070 |
| | | 0.49 | 2.14 | 0.02 | 81.438 |
| | | 0.66 | 3.02 | 0.02 | 84.270 |
| | | 0.79 | 3.20 | 0.02 | 87.984 |
| | | 0.89 | 3.20 | 0.02 | 90.498 |
| | | 0.98 | 3.36 | 0.02 | 92.382 |
| | | 1.09 | 3.59 | 0.01 | 93.180 |
| | | | Calm Water | | 52.532 |
| Containership | 0.087 | 0.44 | 4.20 | 0.03 | 76.179 |
| | | | 6.36 | 0.04 | 83.185 |
| | | 0.85 | 4.20 | 0.01 | 63.951 |
| | | | 6.36 | 0.02 | 72.226 |

Propulsion tests of the cruise ship were performed for a velocity of $21kts$ (ship scale) and wave length with $\lambda/L = 0.21 - 1.09$. The wave steepness, h_W/λ , was kept constant at a value of 2.3 percent. The model was free to heave and pitch, the influence of the other degree of freedom was assumed to be small in head waves (Ley et al., 2014). The test conditions are summarized in Table 10 including non-dimensional wave length, λ_W/L , and steepness, h_W/λ_W , as well as propeller speed, n .

Although advanced numerical methods allow using new concepts to evaluate propulsion performance of ships, numerical propulsion computations were performed in the same way as the physical tests described above. This holds for towing tests as well as for open water tests and made it possible to directly compare computations and model test measurements. Consequently, numerical computations comprised open water propeller characteristics, ship resistance tests, self-propulsion tests in calm water, and wave-added resistance and propulsion tests in waves. Whereas the propeller open water test

was performed only once, the resistance and propulsion tests need to be performed for each considered wave. The propulsion characteristics in waves were determined using averaged values. To minimize errors based on different discretization, model and iterative errors, all computations were performed using the same numerical method and numerical grids. Resistance computations were performed again, to take into account adjustment of numerical setup and grids.

Grids presented in section 4 were used for the computations. At the inlet boundary, velocities, volume fractions, turbulent kinetic energies, and dissipation rates were specified. The hull and appendages surfaces were defined as no-slip walls. At the outlet and top boundaries, the pressure boundary condition was defined, while at the symmetry plane, a symmetry boundary condition was imposed. The origin of the ship-fixed reference frames was situated at the ship's center of gravity. To guaranty best comparability, computations were performed in model scale. The computations were performed for the same conditions as in physical tests. Propeller speed, ship speed etc. were taken from model tests.

7.2 Results

Computed results comprised, first, propeller open water characteristics, then resistance predictions of the towed models and, finally, propulsion characteristics in waves.

7.2.1 Propeller Open Water Test

The computations employed a so-called rotating reference frame, where the coordinate system rotated with the propeller. Momentum conservation equations were extended to account for centrifugal and Coriolis forces (el Moc-tar, 2001). Outer boundaries of the computational domain were situated a sufficiently large distance away from the propeller to largely eliminate disturbances caused by the boundaries. The diameter of the cylindrical computational domain was five propeller diameters large; the inlet boundary was located three propeller diameters ahead of the propeller; the outlet boundary,

ten propeller diameters behind the propeller. Numerous studies examined the associated discretization errors as well as the influence of the size of the computational domain; for details, see el Moctar (2001) and Abdel-Maksoud et al. (1998). Computations were performed at model scale and with a constant turning rate of $n = 15\text{rps}$ and various inflow velocities. The velocity distribution around the propeller is shown in figure 66.

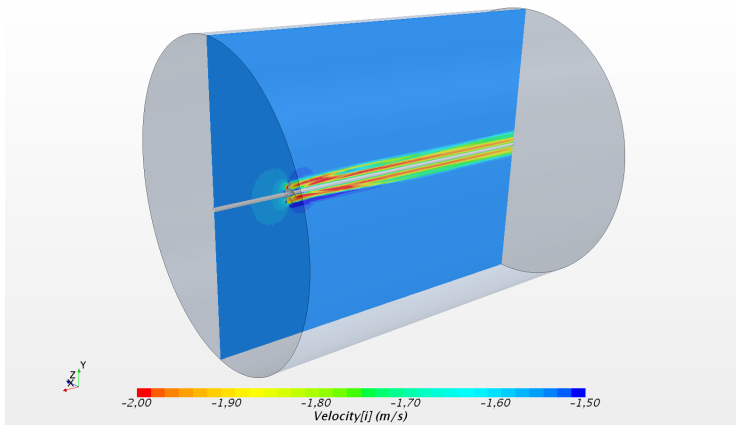
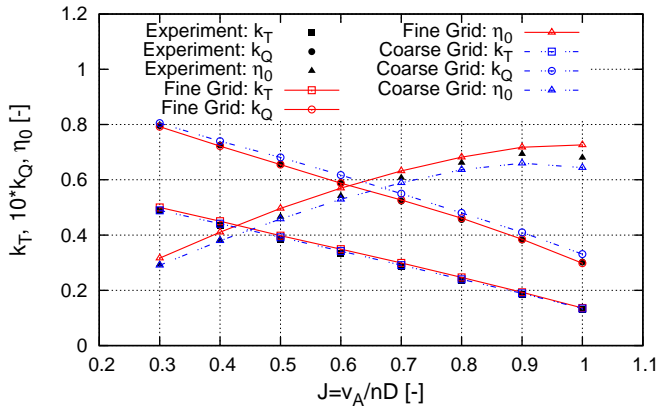
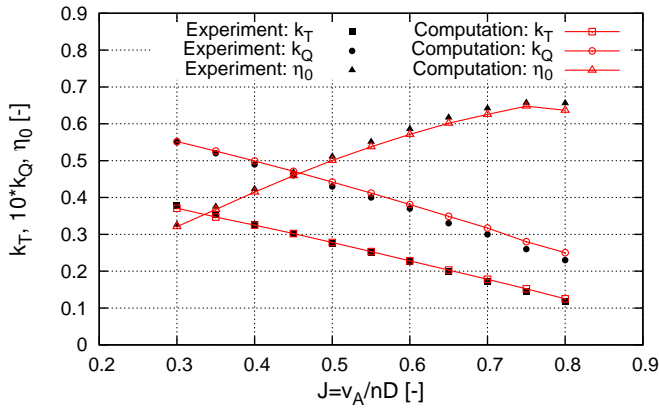


Figure 66: Axial velocity distribution around the propeller of the Container-ship DTC in homogeneous inflow

Figure 67 presents computed propeller open water characteristics. The maximum deviation between measured and computed propeller are less than 3%. The computed open water characteristics were used for the determination of the propulsion characteristics discussed later on.



(a) Cruise Ship



(b) DTC

Figure 67: Computed and measured propeller open water characteristics for the Cruise Ship and the Containership DTC

7.2.2 Resistance Test

Based on the computations performed to investigate the wave-added resistance, described in section 5, resistance computations in calm water and waves were performed again, since small adjustment on the grid has been made to integrate appendages and the propeller domain. In principle however, computational procedure, post-processing and results were similar to the results presented above. To avoid repetition, only the results are presented.

Table 11 summarizes computed and measured calm water resistances of the cruise ship and the containership for the considered forward speeds. Also listed are the associated percentage deviations between computed and measured values. Deviations were less than 3.0% for the cruise ship. Unfortunately, no experimentally-determined calm water resistances were available for the containership.

Table 11: *Computed and measured calm water resistance for the Cruise Ship and the Containership DTC determined for propulsion investigation*

| | Fn [-] | $C_T \cdot 10^3$ | | |
|-------------------|----------|------------------|------------|----------|
| | | Computation | Experiment | Diff [%] |
| Cruise Ship | 0.223 | 4.21 | 4.088 | 2.98 |
| Containership DTC | 0.087 | 3.88 | — | — |

The results in waves are presented in table 12 and are similar to those performed earlier (see section 5). They show fair agreement with results computed earlier and with experimental data in the range of short waves. Differences between computed and measured values in peak range of the cruise ship, were also observed earlier and are discussed in section 5.

7.2.3 Self-Propelled Model

The above investigations demonstrated that the applied numerical method together with the chosen grids were capable to adequately predict not only pro-

Table 12: Computed and measured wave-added resistance for the Cruise Ship and the Containership DTC determined for propulsion investigation

| | | C_{AW} | | | |
|---------------|----------|---------------|-------------|------------|----------|
| | Fn [-] | λ_w/L | Computation | Experiment | Diff [%] |
| Cruise Ship | 0.223 | 0.28 | 2.894 | 2.76 | 4.97 |
| | | 0.39 | 2.904 | 2.85 | 1.76 |
| | | 0.46 | 3.546 | 3.53 | 0.41 |
| | | 0.66 | 3.845 | 3.71 | 3.62 |
| | | 0.79 | 5.731 | 5.61 | 2.22 |
| | | 0.89 | 7.254 | 7.05 | 2.93 |
| | | 0.98 | 8.329 | 7.40 | 12.60 |
| | | 1.09 | 8.077 | 6.66 | 21.29 |
| Containership | 0.087 | 0.44 | 2.5 | — | — |
| | | 0.85 | 3.46 | — | — |

peller characteristics, but also ship resistance in clam water and in waves. Fine grids surrounding the propeller(s) and the ship were combined to consistently assess propulsion forces. A sliding interface connected both grids, thereby allowing the geometrically modeled propeller to rotate.

Propulsion computations were performed initially under calm water conditions and, afterwards, under wave conditions summarized in table 10. For these cases, the forward speed of the cruise ship corresponded to $Fn = 0.223$; the forward speed of the containership, to $Fn = 0.087$. The aim of the physical tests of the containership was to investigate minimum power requirements in adverse conditions where the ship speed is supposed to be low. The scaling factor for the containership was 63.64 according to model tests performed at MARINTEK.

Based on previous investigations (el Moctar, 2001), it was found necessary to specify a small time step to yield accurate propeller forces. This time step was so small that the propeller rotated only one degree over the duration of this time step. However, to reduce the overall computational effort,

computations were started with a ten times larger time step, that is, with the propeller now rotating 10° over the duration of this time step. Computations with the larger time step lasted until the wave pattern and ship motions were sufficiently stable. Only then was computing continued with the smaller time step and accurate and reliable propeller and hull forces were obtained thereafter. Figure 68 shows wave patterns of the self-propelled containership and the cruise ship in waves.

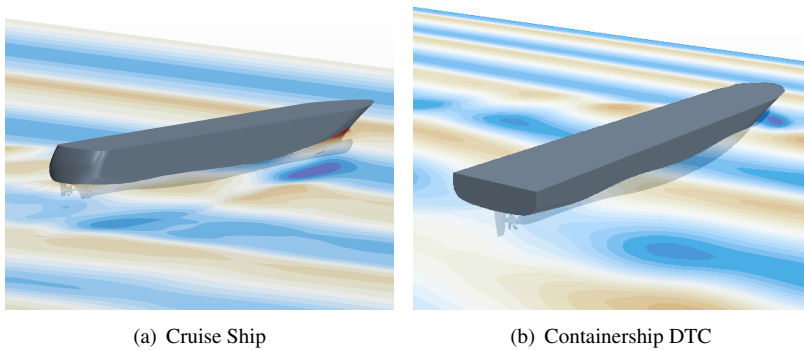


Figure 68: Wave pattern for the Cruise Ship at $\mathbf{Fn} = 0.223$, $\lambda_w/L = 1.09$, $\mathbf{h}_w = 0.1\mathbf{m}$ and $\mathbf{n} = 15.53\mathbf{rps}$ and for the Containership DTC at $\mathbf{Fn} = 0.087$, $\lambda_w/L = 0.85$, $\mathbf{h}_w = 0.1\mathbf{m}$ and $\mathbf{n} = 9.05\mathbf{rps}$

Orbital velocities and motion induced velocities affect flow conditions around the hulls significantly. To illustrate this, figures 69 - 71 show non-dimensional axial velocities, V_x/V_S , at aft ship of the containership and the cruise ship during a encounter period. The axial velocity directly ahead of the propeller varies between 80% and 120% of the model's speed.

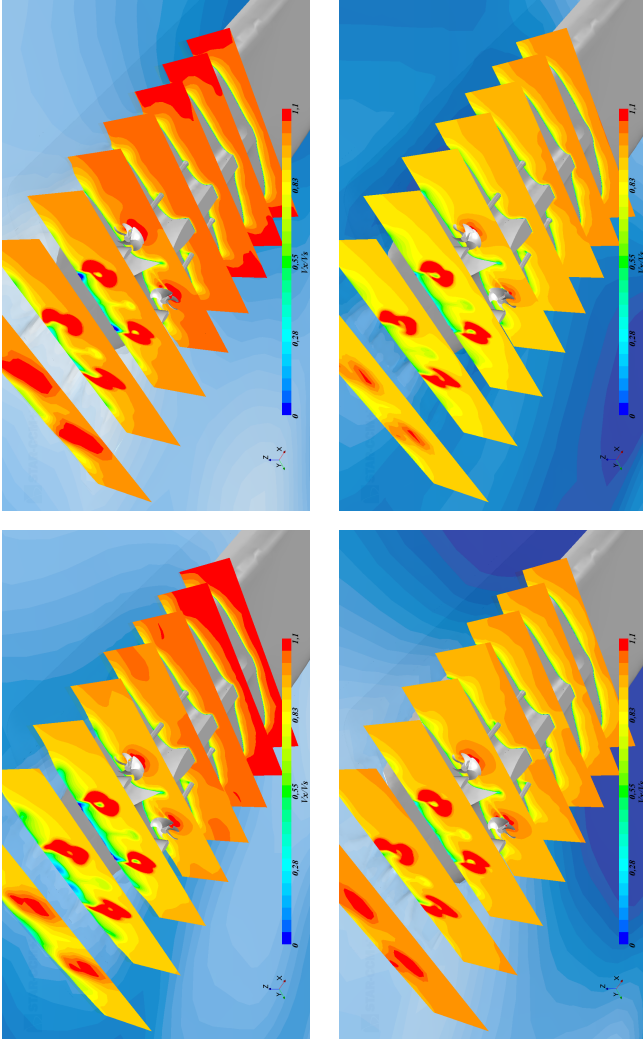


Figure 69: Axial velocities at aft ship for the Cruise Ship at $\text{Fn} = 0.223$, $\lambda_w/L = 1.09$, $h_w = 0.1\text{m}$ and $n = 15.53\text{rps}$

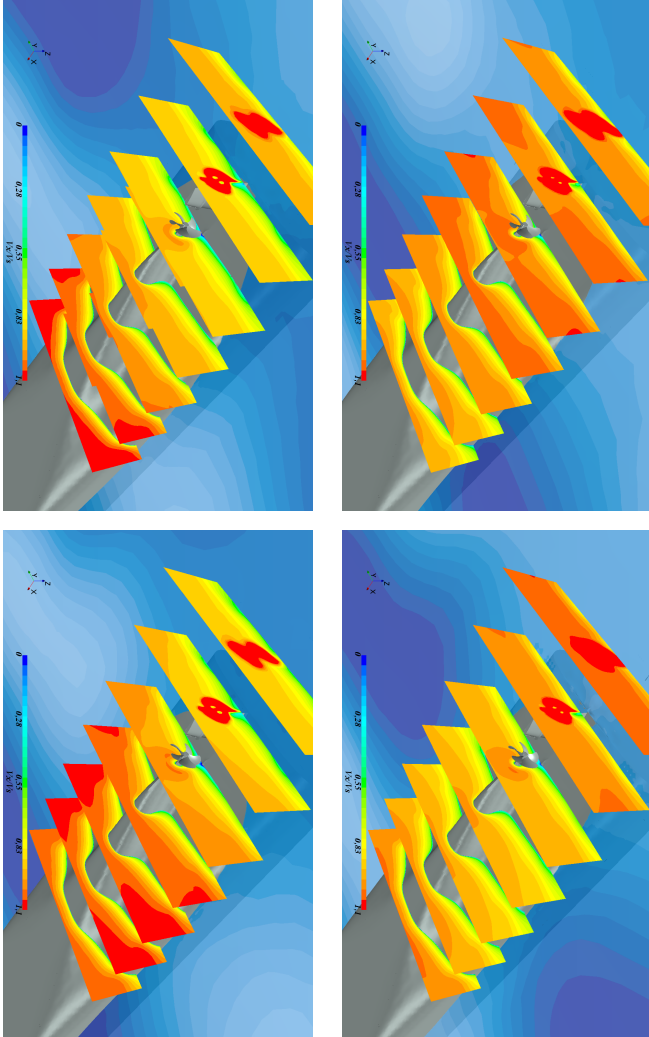


Figure 70: Axial velocities at aft ship for the Containership DTC at $\text{Fn} = 0.087$, $\lambda_w/L = 0.85$, $h_w = 0.1\text{m}$ and $n = 9.05\text{rps}$

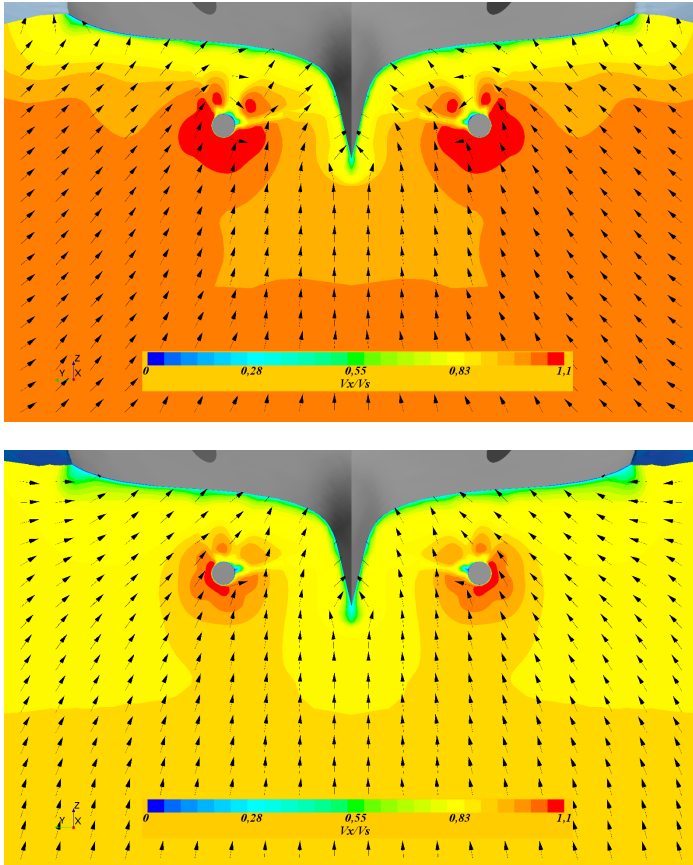


Figure 71: Variation of axial propeller inflow for the Cruise Ship at $F_n = 0.223$, $\lambda_w/L = 1.09$, $h_w = 0.1\text{m}$ and $n = 15.53\text{rps}$

Figure 72 presents representative computed and measured time histories and mean values of the vertical motion in the propeller plane for the cruise ship at $F_n = 0.223$, $\lambda_w/L = 1.09$ and $n = 15.53rps$. Due to wave nonlinearities and their interaction with hull and appendages, the computed and measured time histories do not behave purely harmonic. This issue is taken into account when determining averaged values.

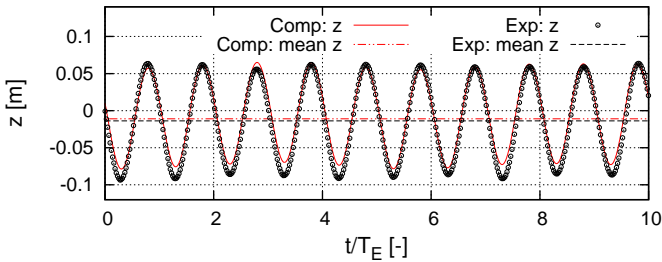


Figure 72: Time history of the vertical motion in the propeller plane for the Cruise Ship at $F_n = 0.223$, $\lambda_w/L = 1.09$ and $n = 15.53rps$

Figures 73 and 74 presents comparative heave and pitch motion time histories of the towed and self-propelled ships. These time histories extend over one encounter period, T_E . The wave length for the cruise ship corresponds to $\lambda_w/L = 0.98$; the wave length for the containership, to $\lambda_w/L = 0.85$. The wave height was $0.1m$ and $0.095m$, respectively. The wave steepness was moderate and, therefore, heave and pitch motions are seen to behave linearly. Overall, motion behavior is nearly similar under towed and self-propelled conditions. Under the wave conditions considered here, motion amplitudes of the ships when towed are slightly larger than when the ships are self-propelled. Apparently, the turning propeller dampened the wave-induced heave and pitch motions of the self-propelled ships. This trend is also noticeable from the heave and pitch RAOs of the cruise ship presented in figure 75. Here, coefficients C_z and C_θ are heave and pitch amplitudes normalized against wave amplitude and wave slope, respectively.

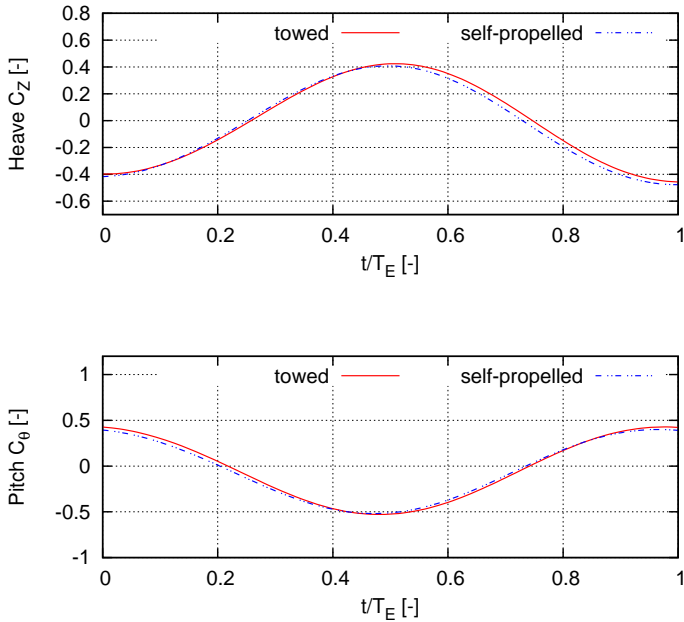


Figure 73: Non-dimensional heave and pitch for the Cruise Ship at $\mathbf{Fn} = 0.223$, $\lambda_W/L = 0.98$, $h_W = 0.1\text{m}$ and $\mathbf{n} = 15.4\text{rps}$ under towed and self-propelled conditions (see Tabel 10)

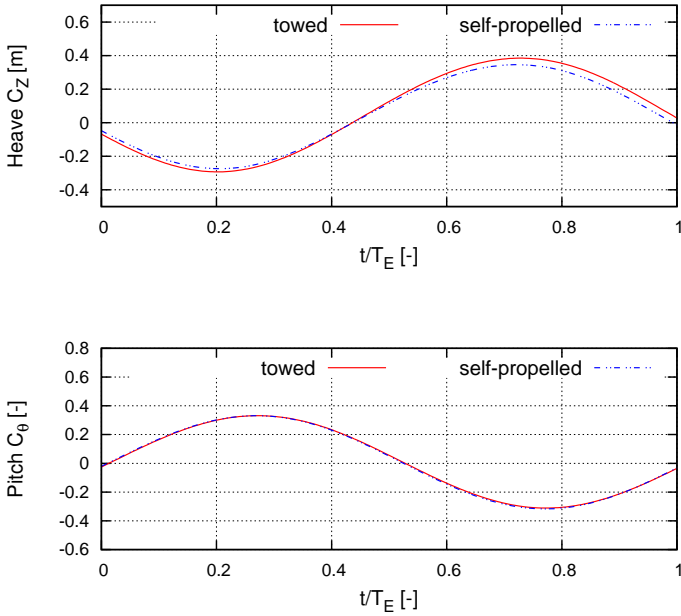


Figure 74: Non-dimensional heave and pitch for the Containership DTC at $\mathbf{Fn = 0.087}$, $\lambda_W/L = 0.85$, $\mathbf{h_W = 0.095m}$ and $\mathbf{n = 10.43rps}$) under towed and self-propelled conditions (see Tabel 10)

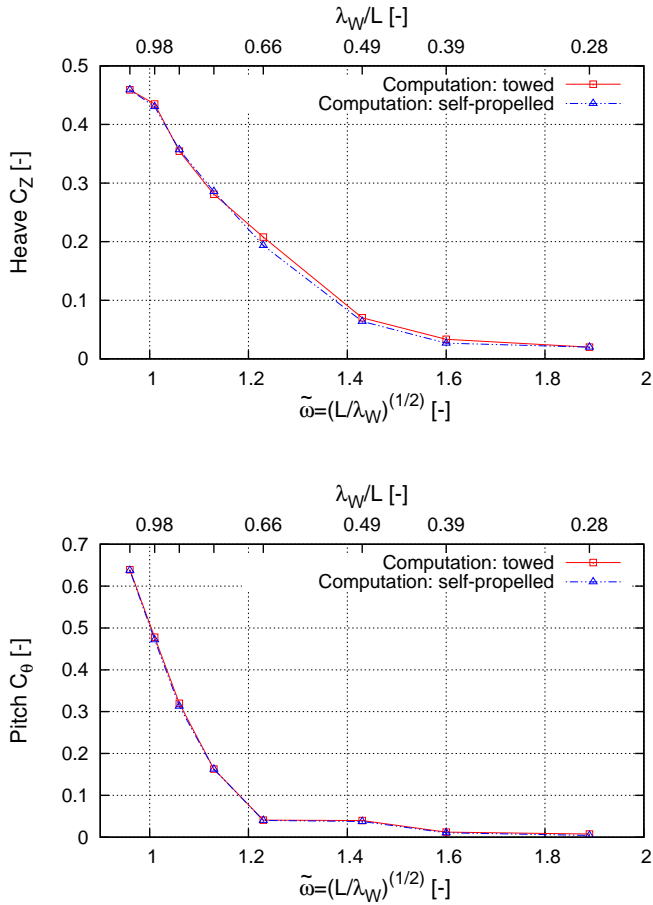


Figure 75: Heave and pitch RAOs for the towed and the self-propelled Cruise Ship at $F_n = 0.223$

Figures 76 - 79 show computed and measured time histories, extending over one encounter period, for the two ships advancing in regular head waves at speeds corresponding to $Fn = 0.223$ for the cruise ship and $Fn = 0.087$ for the containership. In these figures, the upper graphs trace time histories and mean values of vertical motion at the propeller hub; the center graphs, time histories and mean values of propeller torque coefficient, k_Q ; and the bottom graphs, time histories and mean values of propeller thrust coefficient, k_T . Figures 76 and 78 are valid for results obtained in relatively short waves ($\lambda_w/L = 0.49$ for the cruise ship and $\lambda_w/L = 0.44$ for the containership); figures 77 and 79, for results obtained in longer waves ($\lambda_w/L = 0.98$ for the cruise ship and $\lambda_w/L = 0.85$ for the containership).

The propeller torque and thrust traces are characterized by pronounced fluctuations. Qualitatively, propeller torque and thrust resemble each other, indicating the direct coupling that exists between both. The cause of these thrust fluctuations is related to propeller inflow variations induced by orbital velocities and ship motions. Angle of attack and relative velocity at the blades vary now with radius and blade position during propeller revolution, el Moctar (2001). Higher frequency fluctuations are related to blade frequency, whereas the low frequency corresponds to the encounter frequency. In short waves the phase angle between vertical propeller motion and propeller forces is small. Propeller forces exhibit extreme values whenever vertical motions reach their upper or lower dead centers. At these instants of time, heave motions reach their maxima/minima values. Further on, the wave crest/trough is located at the propeller level and, consequently, the longitudinal components of orbital fluid velocities attain their maxima/minima. Thus, the influence of orbital velocities is dominant in short waves (figure 69, left). In longer waves, ship motion amplitudes become larger, and consequently motion-induced velocities. The phase angle between vertical motions and propeller forces increases. As expected, in longer waves ship motions have a greater influence on propeller forces.

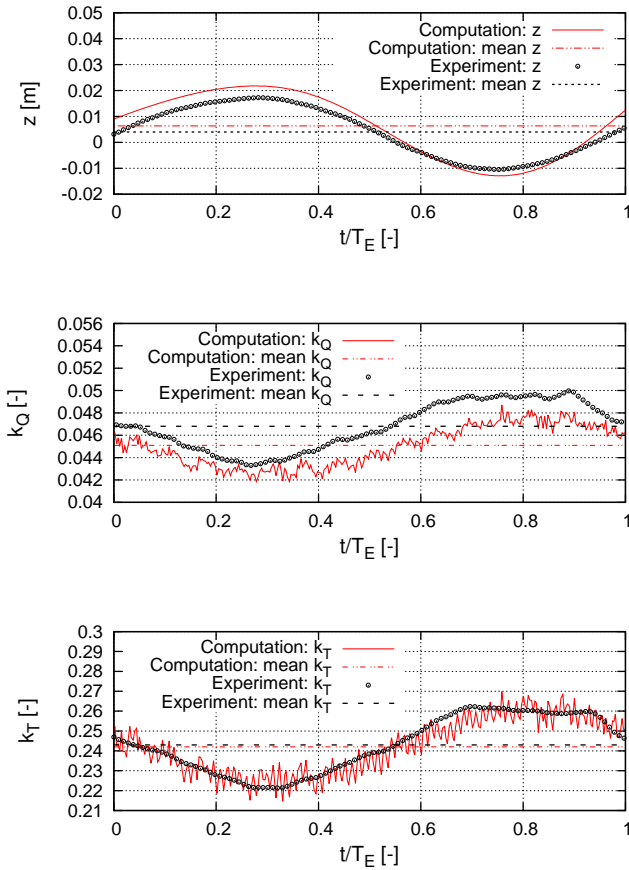


Figure 76: Time histories of the propeller's vertical motion (top), the torque coefficient (center), and the thrust coefficient (bottom) for the Cruise Ship at $F_n = 0.223$, $\lambda_w/L = 0.49$, $h_w = 0.1\text{m}$ and $n = 13.57\text{rps}$

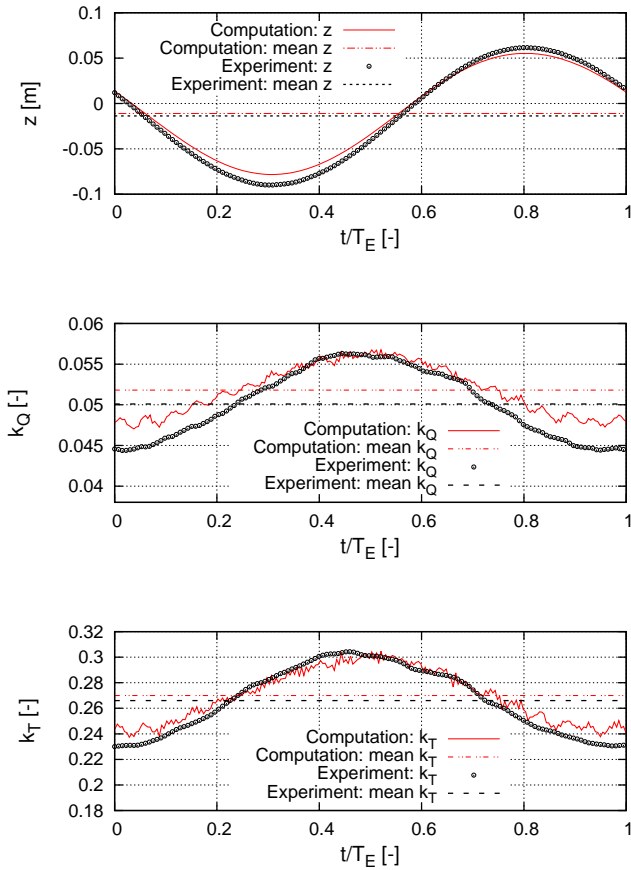


Figure 77: Time histories of the propeller’s vertical motion (top), the torque coefficient (center), and the thrust coefficient (bottom) for the Cruise Ship at $F_n = 0.223$, $\lambda_w/L = 0.98$, $h_w = 0.1\text{m}$ and $n = 15.4\text{rps}$

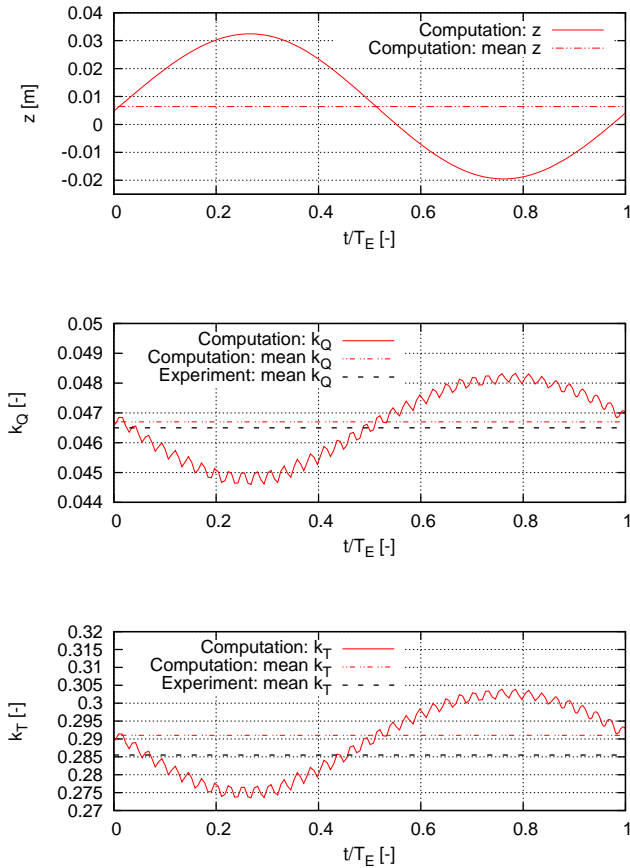


Figure 78: Time histories of the propeller's vertical motion (top), the torque coefficient (center) and the thrust coefficient (bottom) for the Containership DTC at $\text{Fn} = 0.087$, $\lambda_W/L = 0.44$, $h_W = 0.1\text{m}$ and $n = 8.02\text{rps}$

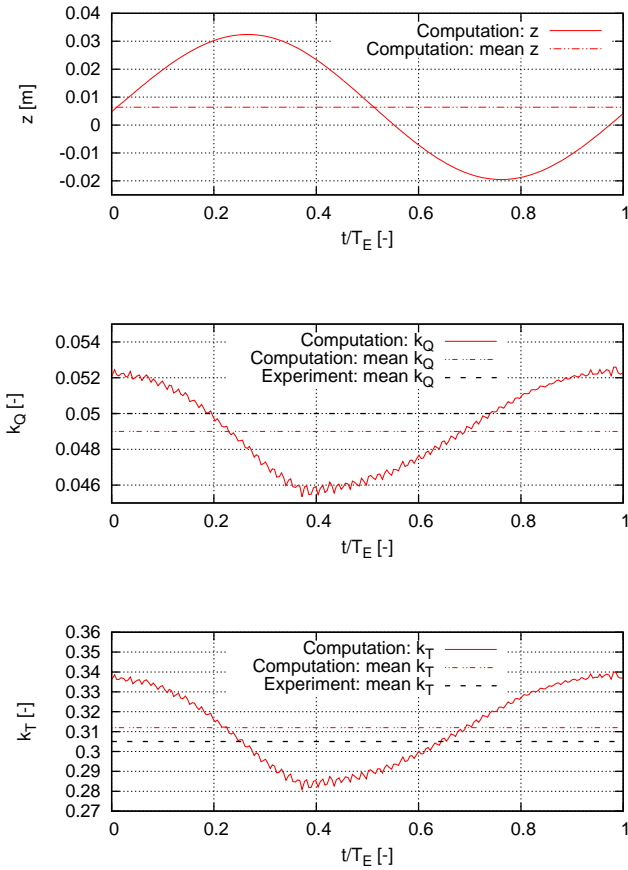
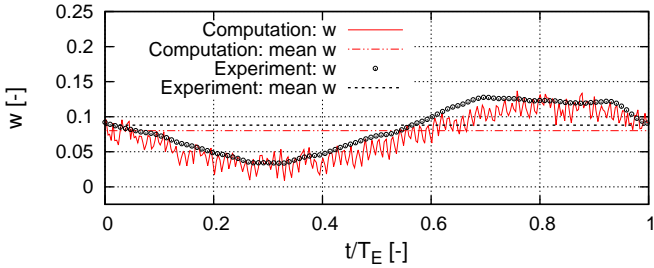


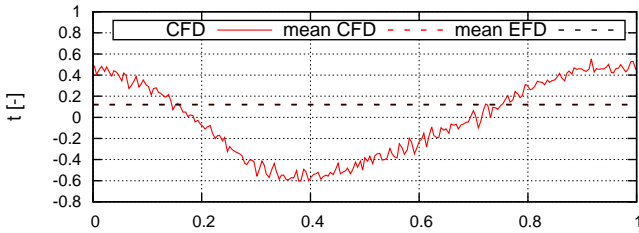
Figure 79: Time histories of the propeller’s vertical motion (top), the torque coefficient (center) and the thrust coefficient (bottom) for the Containership DTC at $\lambda_W/L = 0.85$, $h_W = 0.1\text{m}$ and $n = 9.05\text{rps}$

Figures 80 and 81 present computed and measured time series, extending over one encounter period, of the wake fraction, w , and thrust deduction fraction, t , pertaining to the cruise ship advancing in regular head waves at a speed corresponding to $Fn = 0.223$. The graphs in figure 80 are valid for results obtained in relatively short waves of $\lambda_w/L = 0.49$; the graphs in figure 81, for results obtained in longer waves of $\lambda_w/L = 0.98$. The wake fraction was calculated based on the thrust identity approach (the propeller produces the same thrust in a wake field of wake fraction as in open-water with speed $v_a = v(1 - w)$ for the same propeller rate (Bertram, 2000)). Distinctive fluctuations are noticeable, and they are more pronounced in longer waves. For example, in long waves the wake fraction varies between 0.04 and 0.12, which corresponds to an 8% fluctuation of axial propeller inflow velocities.

Figure 82 plots computed and measured coefficients of propeller torque, k_Q , and propeller thrust, k_T , versus the wave length to ship length ratio, λ_w/L , as well as the normalized encounter frequency, $\tilde{\omega}$, for the two ships advancing in calm water and in regular head waves at speeds corresponding to $Fn = 0.223$ for the cruise ship and $Fn = 0.087$ for the containership. Solid lines represent computed values, measured values are marked with points, and dashed and dotted lines identify measured and computed calm water values, respectively. Generally, computed and measured values compare favorably. For the cruise ship, the time-average values of computed thrust coefficients deviate on average 3.15% and at most 4.84% from measured values; for the containership, these values deviate on average 2.25% and at most 4.8% from measured values. For the cruise ship, the time-average values of computed torque coefficients deviate on average 3.42% and at most 4.24% from measured values; for the containership, these values deviate on average 1.79% and at most 4.66% from measured values. In short waves diffraction dominates and ship motions are small. In long waves ship motions and thus also the inclined flow into the propeller plane are more pronounced, consequently, the propeller forces and moments increase (el Moctar, 2001). Furthermore, the propeller's operating point changed with increasing ship resistance. Consequently, propeller forces and moments increase in longer waves.

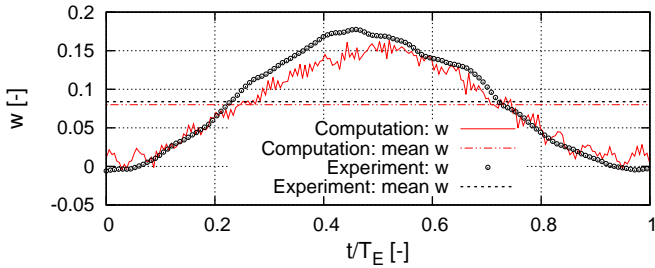


(a) Wake fraction

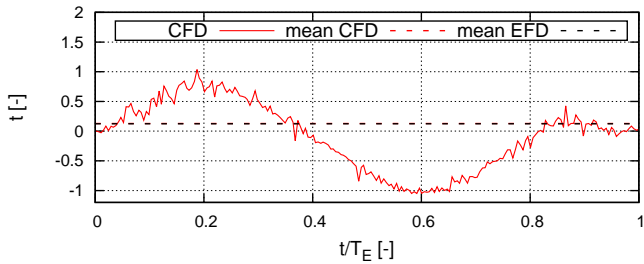


(b) Thrust deduction

Figure 80: Time histories of wake fraction and thrust deduction for the Cruise Ship at $\mathbf{Fn} = 0.223$, $\lambda_w/L = 0.49$, $h_w = 0.1\text{m}$ and $\mathbf{n} = 13.57\text{rps}$

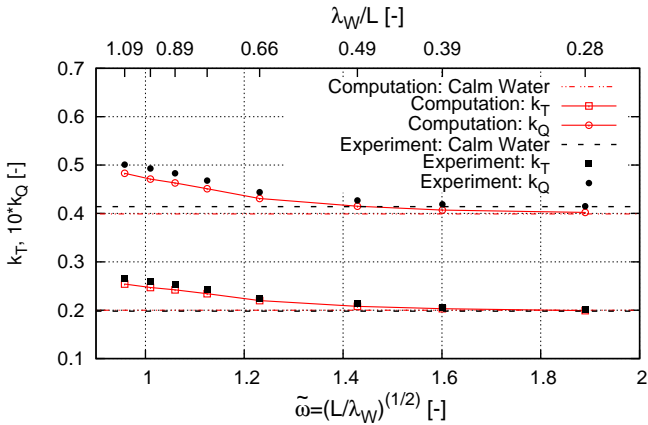


(a) Wake fraction

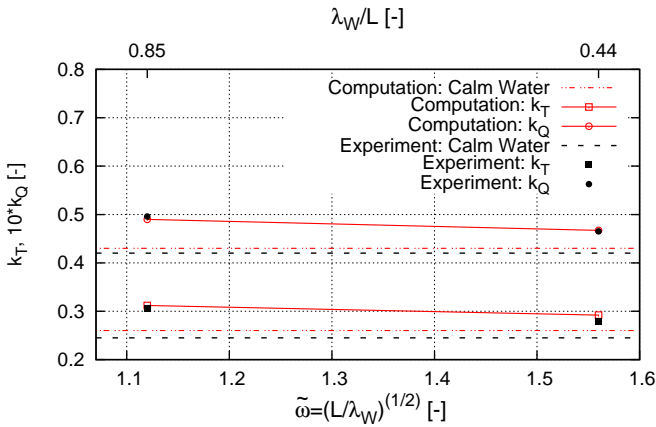


(b) Thrust deduction

Figure 81: Time histories of wake fraction and thrust deduction for the Cruise Ship at $\mathbf{Fn} = 0.223$, $\lambda_w/L = 0.98$, $\mathbf{h}_w = 0.1\mathbf{m}$ and $\mathbf{n} = 15.4\mathbf{rps}$



(a) Cruise Ship



(b) Containership DTC

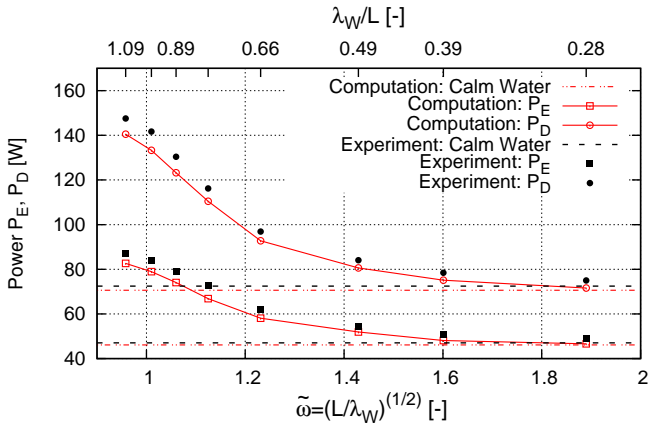
Figure 82: Computed and measured coefficients of thrust and torque for the Cruise Ship at $\mathbf{Fn} = 0.223$ and the Containership DTC at $\mathbf{Fn} = 0.087$ in regular head waves and calm water

7.2.4 Propulsion Characteristics in Waves

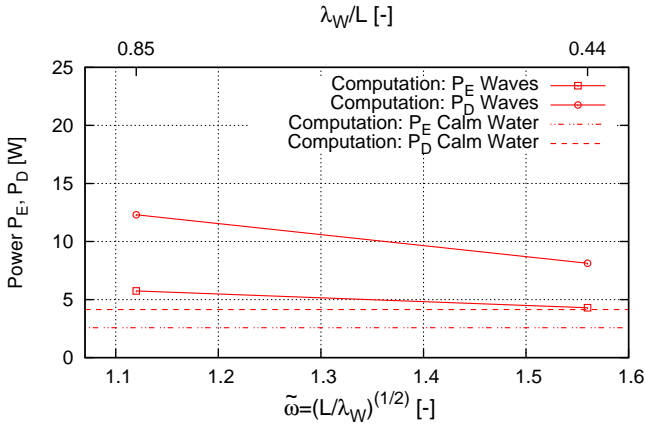
Values of ship resistance and propeller forces, computed on fine grids as described above, were used to determine the propulsion characteristics according to procedures recommended by the ITTC (2008), and these results were compared with available model test measurements. For the cases investigated and listed in table 4 of the cruise ship at $Fn = 0.223$ and the containership at $Fn = 0.087$, figure 83 plots computed and measured effective and delivered power, P_E and P_D , in calm water and in regular head waves against non-dimensional wave length and non-dimensional wave frequency. Measured values are given only for the cruise ship because these were not available for the containership. In calm water as well as in waves within the range of frequencies plotted in table 10, the computed effective power and the propeller delivered power compared favorably to measurements. For the cruise ship, mean and maximum values of delivered propeller power deviate from measurements by 4.77 and 5.48%, respectively; mean and maximum values of effective power, by 5.6 and 6.3%, respectively. As expected, the required power increases in longer waves. In waves of $\lambda_W/L = 1.09$ the propeller delivered power of the cruise ship is almost 100% higher than in calm water, and the effective power increases by 78%. In contrast, in shorter waves of $\lambda_W/L = 0.49$ the propeller delivered power of the cruise ship is only 14.3% higher than in calm water, and the effective power increases by only 12.8%.

For the containership, this trend is similar. In waves of $\lambda_W/L = 0.85$ and $h_W = 0.067m$, delivered power and effective power increase by 197% and 122%, respectively; in waves of $\lambda_W/L = 0.44$ and $h_W = 0.062m$ this increase is only 96% and 66%, respectively. The relatively large power increase of the containership is related to its relatively low forward speed ($Fn = 0.087$). As expected, the propeller delivered power increases at a greater rate than effective power.

Consequently, the propulsion efficiency, η_D , decreases in waves, as seen in figure 84. Measured values are given only for the cruise ship because these were not available for the containership. For the cruise ship, computed and measured propulsion efficiency compare favorably to measurements. Over the entire frequency range, their mean and maximum deviation is only 0.95%



(a) Cruise Ship



(b) Containership DTC

Figure 83: Effective and delivered power for the Cruise Ship at $\mathbf{Fn} = 0.223$ and the Containership DTC at $\mathbf{Fn} = 0.087$ in regular head waves and calm water

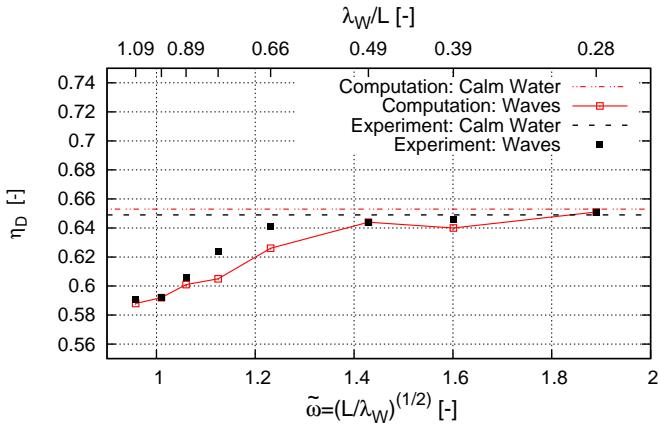
and 2.96%, respectively. For the containership, the propulsion efficiency in waves is up to 9.95% less than in calm water, for containership this value reduces by maximum 24.2%.

Propulsion efficiency can also be expressed by the product of hull efficiency, η_H , relative rotative efficiency, η_R , and propeller open water efficiency, η_0 ; that is, $\eta_D = \eta_H \eta_0 \eta_R$. Decomposition of the propulsion efficiency enabled a detailed look into the underlying physics.

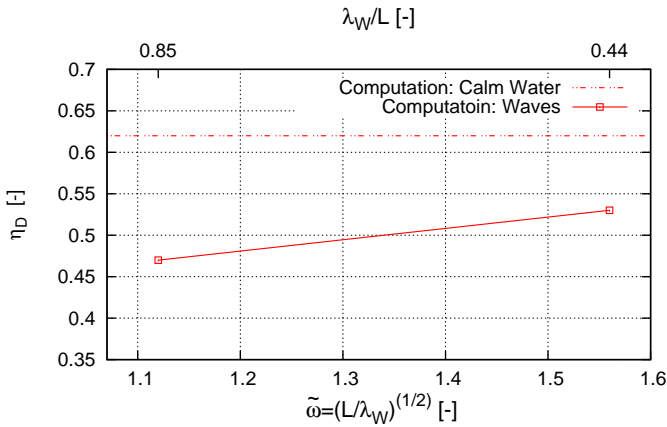
For the cruise ship at $Fn = 0.223$ and the containership at $Fn = 0.087$, figure 85 plots computed propeller open water efficiency, η_0 , in calm water and in regular head waves against normalized wave length and normalized wave frequency. Here again, measured values are given only for the cruise ship because these were not available for the containership. As found above, in calm water as well as in waves within the range of frequencies listed in table 10, computed values compare favorably to measurements. The mean deviation is 1.6%; the maximum deviation, 2.54%. For both ships the propeller open water efficiency decreases with increasing wave length. For the cruise ship, this decrease is 7.58%; for the containership, 22.18%. This influence is mainly related to the higher propeller loading caused by the wave-added resistance of the ships in waves, i.e., open water efficiency decreases with increasing wave-added resistance in waves, see figure 66.

For the cruise ship at $Fn = 0.223$ and the containership at $Fn = 0.087$ in calm water and in regular head waves, figure 86 plots the relative rotative efficiency, η_R , against normalized wave length and normalized wave frequency. Generally, computed and measured values compare favorably. For the cruise ship, the mean of computed values deviates 0.43% from measurements; the maximum of computed values, 0.83%. It is seen that, for the cruise ship, η_R is not significantly affected by wave length, as in waves η_R differs at most by only 0.6% compared to its value in calm water. For the containership, the greatest difference of η_R values in waves is 2%. Thus, the influence of waves on rotative efficiency is slightly larger for the containership. Nevertheless, it was found that η_R is hardly affected by the relatively moderate waves investigated here.

For the cruise ship at $Fn = 0.223$ and the containership at $Fn = 0.087$ in calm water and in regular head waves, figure 87 plots hull efficiency, η_H ,

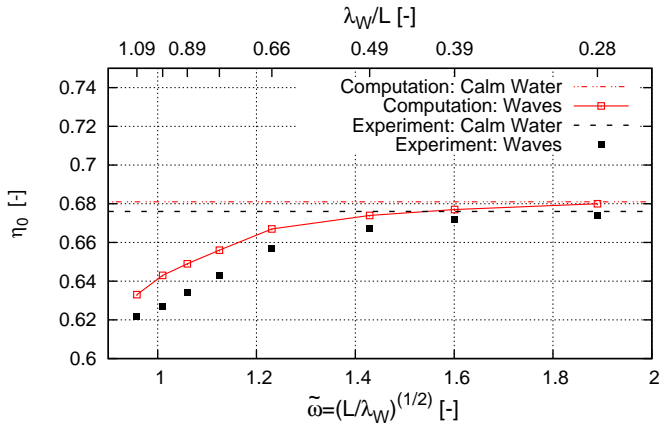


(a) Cruise Ship

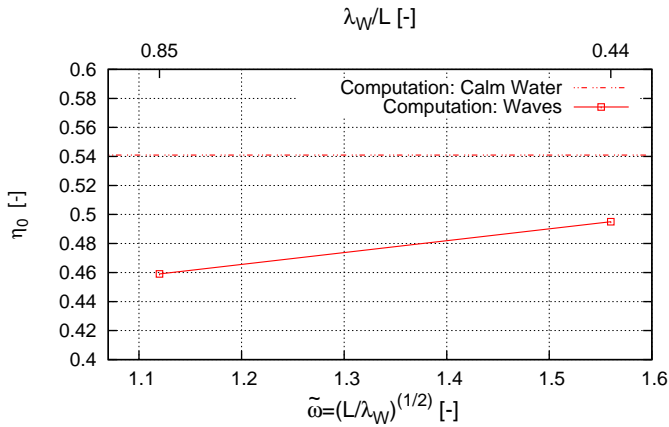


(b) Containership DTC

Figure 84: Propulsive efficiency for the Cruise Ship at $\mathbf{Fn} = 0.223$ and the Containership DTC at $\mathbf{Fn} = 0.087$ in regular head waves and calm water

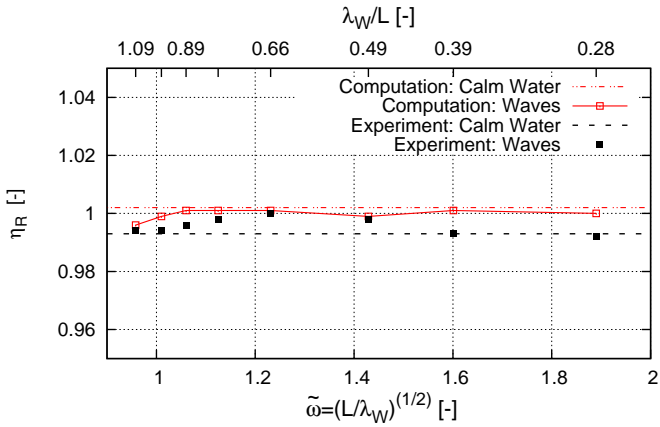


(a) Cruise Ship

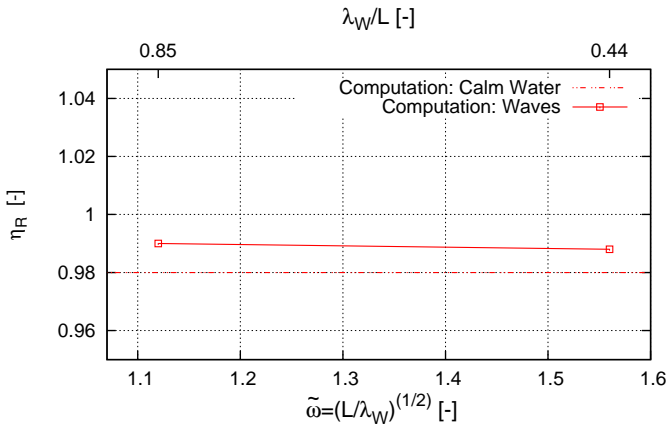


(b) Containership DTC

Figure 85: Open water efficiency for the Cruise Ship at $\mathbf{Fn} = 0.223$ and the Containership DTC at $\mathbf{Fn} = 0.087$ in regular head waves and calm water



(a) Cruise Ship



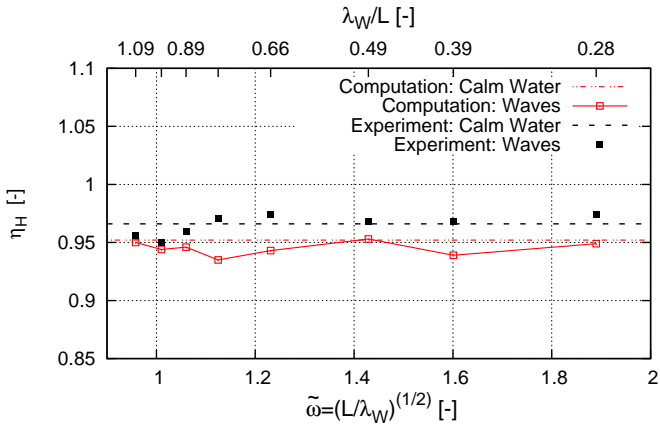
(b) Containership DTC

Figure 86: Rotative efficiency for the Cruise Ship at $\mathbf{Fn} = 0.223$ and the Containership DTC at $\mathbf{Fn} = 0.087$ in regular head waves and calm water

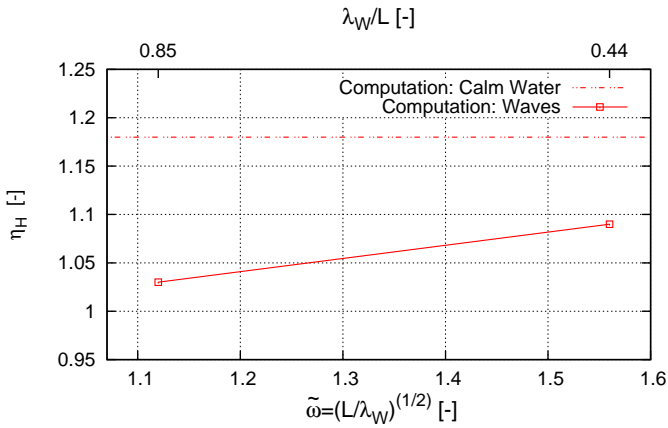
against normalized wave length and normalized wave frequency. Computed and measured values generally compare favorably. Computed mean and maximum values deviated 2.1% and 3.7% from measured values, respectively. For the cruise ship, η_H values in waves differed at most 3% from those in calm water; however, for the containership, η_H values in waves differed up to 12.7% from those in calm water. Thus, the cases considered here demonstrated that the waves influenced hull/propeller interaction significantly less for the twin screw cruise ship than for the single screw containership.

To find out the reasons for the ship-dependent sensitivity of hull efficiency, η_H , on wave height, the wake fraction and the thrust deduction factor were determined in waves. Figures 88 and 89 plot these values against normalized wave length and normalized wave frequency. Comparative measured values are given only for the cruise ship because these were not available for the containership. Deviations between computed and measured values are 10.2% for thrust deduction and 7.12% for wake fraction in average. It is apparent that not only the wake fraction, but also the thrust deduction fraction for the containership are influenced more by waves than is the case for the cruise ship. Thus, for the cruise ship, the wake fraction in waves is at most 6.2% less than wake fraction in calm water, and the thrust deduction factor changes by at most 5.18%. In contrast, for the containership, the wake fraction which changes up to 38.1%, and the thrust deduction factor, which changes up to 57.4%, are affected more by waves. The differing sensitivity of hull efficiency, η_H , for the two ship types can be distinctly traced to the influence of waves on wake fraction and thrust deduction factor. Thus, the cases considered here demonstrated that waves had a greater influence on hull/propeller interaction for the single screw containership than for the twin screw cruise ship.

For the cruise ship at $Fn = 0.223$ and the containership at $Fn = 0.087$ in calm water and in regular head waves, figure 90 plots all four propulsion efficiencies ($\eta_D, \eta_H, \eta_R, \eta_0$) against normalized wave length and normalized wave frequency. It summarizes the findings attained regarding the influence of waves on the propulsion characteristics for the cruise ship and the containership. For the cruise ship, the decreasing propulsion efficiency, η_D , in waves was caused almost exclusively by the decreasing open water propeller effi-



(a) Cruise Ship



(b) Containership DTC

Figure 87: Hull efficiency for the Cruise Ship at $\mathbf{Fn} = 0.223$ and the Containership DTC at $\mathbf{Fn} = 0.087$ in regular head waves and calm water

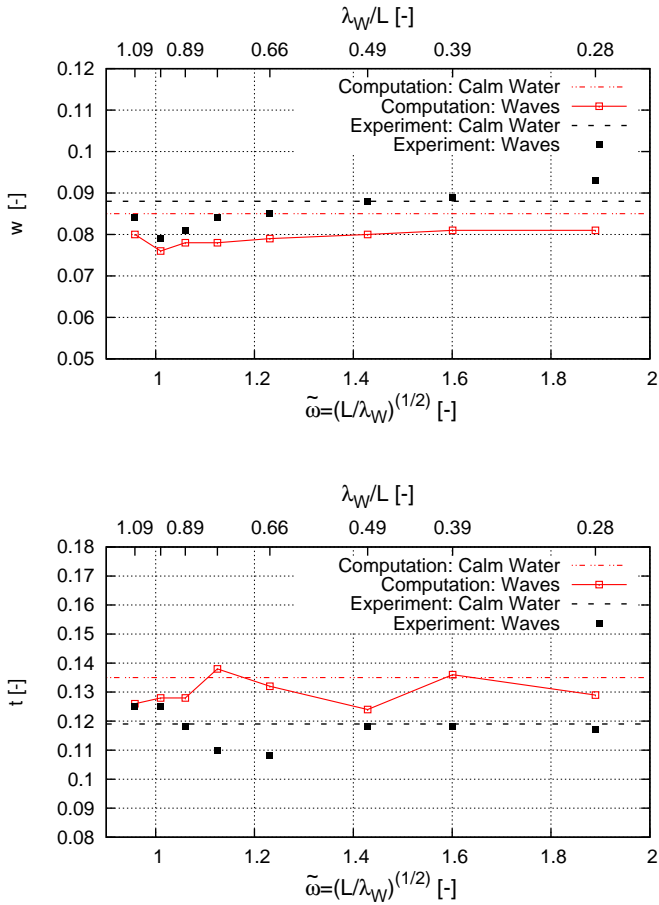


Figure 88: Thrust deduction factor and wake fraction for the Cruise Ship at $F_n = 0.223$ in regular head waves and calm water

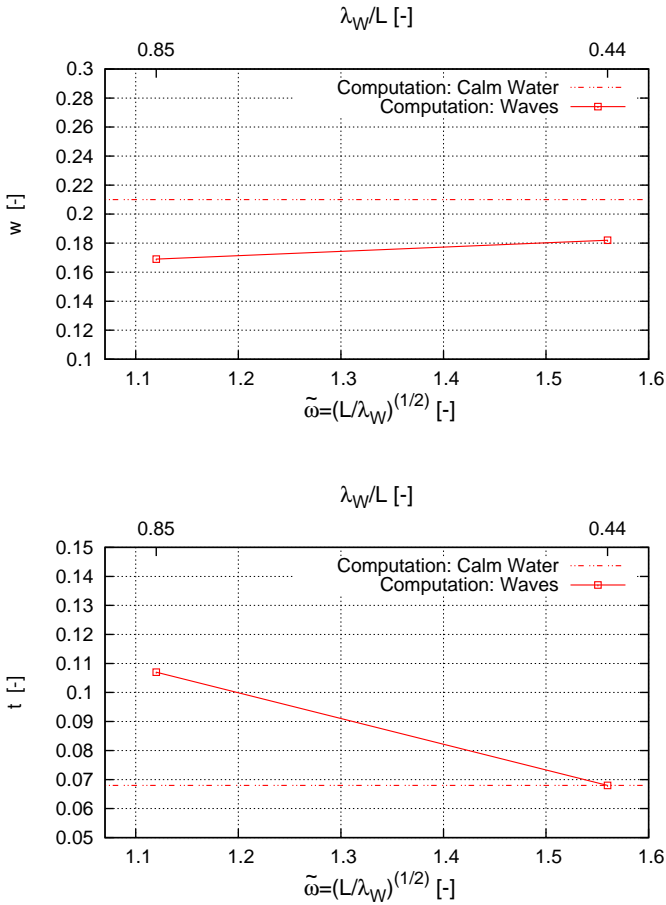
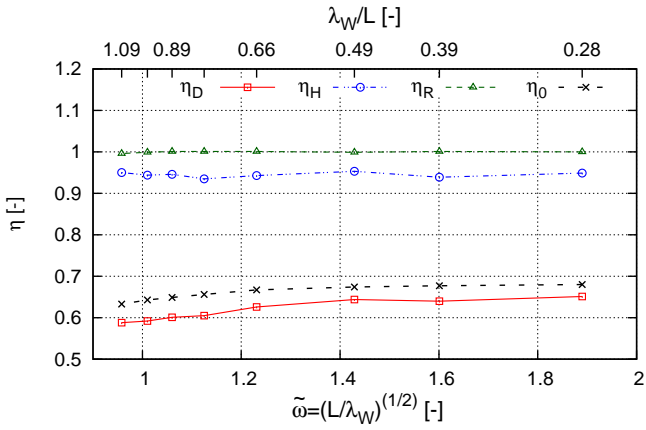


Figure 89: Thrust deduction factor and wake fraction for the Cruise Ship at $F_n = 0.223$ and the Containership DTC at $F_n = 0.087$ in regular head waves and calm water

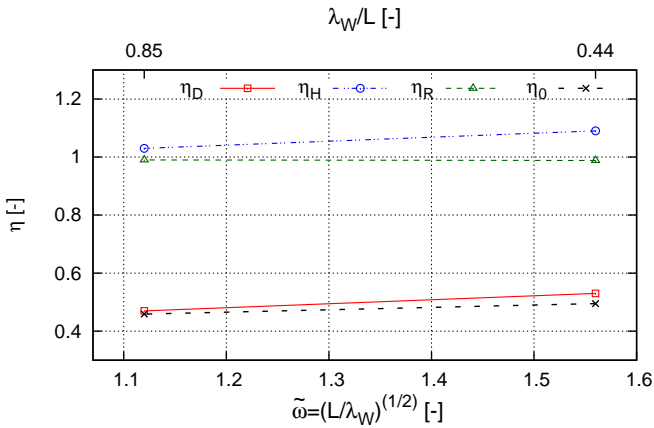
ciency, η_0 , which depends on the operation point of the propeller and there-with, on the ship's resistance. Although wake fraction and thrust deduction factor oscillate strongly, their mean values are hardly influenced by waves. Hence, the ship's hull efficiency, η_H , remains nearly constant in waves. This means that under considered wave conditions neither orbital fluid velocities nor ship motions significantly influenced hull/propeller interaction. Also the rotative efficiency, η_R , does not significantly change in waves. To estimate the propulsion characteristics of the cruise ship in moderate waves, it is sufficient to account for the wave-added resistance when evaluating the operation point of the propeller.

For the containership, on the other hand, the change of propulsion efficiency, η_D , in addition to the change of open water propeller efficiency, η_0 , is mainly caused by the ship's hull efficiency, η_H . Hence, here the changing flow surrounding the hull and the inflow to the propeller do indeed affect the ship's propulsion characteristics. The hull/propeller interaction is mainly governed by the change of the mean value of the thrust deduction fraction, see figure 88. It stands to reason that the diverse behavior of the ship's hull efficiency, η_H , is related to the configuration of the propulsion unit itself.

Generally, high accuracy was required to compute propulsion characteristics, especially for the wake fraction and the thrust deduction factor and, with it, the hull efficiency, as they reacted sensitively to small changes of the propulsion conditions and the propeller service point. To what extent the obtained results are transferable to other propeller operation points and to different ships needs to be demonstrated in further investigations.



(a) Cruise Ship



(b) Containership DTC

Figure 90: All efficiency for the Cruise Ship at $\mathbf{Fn} = 0.223$ and the Containership DTC at $\mathbf{Fn} = 0.087$ in regular head waves

7.3 Conclusion

The influence of regular head waves on propulsion characteristics of a twin screw cruise ship and the single screw containership DTC was numerically and experimentally investigated using a RANS based flow-solver. Employing the sliding interface method allowed the geometrically modeled propeller to rotate when needed. All computations were performed on the same numerical grids to limit errors originating from different spatial and temporal discretizations. Grid studies were performed to evaluate discretization errors occurring in separate mesh regions, such as regions surrounding the hulls and the rotating propellers. Numerical results were compared to experimental measurements obtained from model tests. Discretization errors may significantly influence computed propeller torque, but computed propeller thrust was nearly unaffected. Fair agreement between measured and computed thrust and torque was obtained on the fine grids. Computations of the towed models in calm water and in regular head waves compared favorably to experimental measurements. Computations of the self-propelled model in calm water and in regular head waves were performed to obtain hull-propeller interaction characteristics and propeller forces. Propeller forces were sensitive to temporal discretizations; therefore, to obtain accurate results, it was necessary to specify small time steps, leading to at most one degree of propeller rotation per time step. Such small time steps, together with the use of the sliding interface method, caused computations to be time consuming. Generally, computed forces compared favorably to measurements. The greatest deviation between computed and measured propeller forces for all cases was less than five percent; the average deviation, about 3.5%. Numerical results were used to estimate propulsion characteristics; specifically, propulsion efficiency, rotative efficiency, hull efficiency, and propeller open water efficiency. This required accurate computation of intermediate steps as well as careful evaluation of results. All factors, including the thrust deduction factor and wake fraction, correlated favorably to measurements. It was found that the propulsion efficiency decreased in waves. Based on the considered cases, this was related to the configuration of the propulsion units themselves. The main cause for the decreasing propulsion efficiency of the twin screw ship was

the propeller's efficiency, which in turn depended on the propellers' operation point and, thereby, on the ship's added resistance. For the containership, the changed operation point of the propeller and the ship's hull efficiency were responsible for the changing propulsion efficiency. Hence, for this ship the ever-changing flow surrounding the hull and the inflow to the propeller caused by the orbital fluid velocities and the ship motions affected its propulsion characteristics.

8 Speed Loss in Waves

Structural loads on a ship hull in seaways primarily depend on the actual ship speed and the angle between wave propagation and the ship's heading. The actual ship speed in seaways depends on the ship size, hull shape and propulsion system and may vary significantly from ship to ship. Classification societies consider the actual ship speeds to be $\frac{2}{3}$ of the service speed, which is assumed to be conservative in critical seaways. Thus hull structure may be oversized and causes an unnecessary increase in ship weight, which stands in contrast to economic and ecological interests. Furthermore, the forward speed of a ship has a significant influence on the ship's maneuverability. In particular, in coastal waters, good maneuverability is required to ensure safe ship operations. Good maneuverability includes criteria such as holding position, changing course or leaving dangerous water even against wave and wind in heavy weather conditions. These are only two aspects that require a profound prediction of the speed loss in moderate and adverse sea states.

The above-presented computations confirmed the general suitability of the RANS methods and the numerical grids used to compute the ship behavior, namely, motion, resistance and propulsion characteristics in waves. Due to the holistic view of the system and the possibility of performing full-scale investigations, a great range of opportunities are available for the dynamic analysis of ship designs. One of these opportunities is the direct determination of the speed loss of ships in waves.

In this section, RANS computations of the speed loss of the free-running cruise ship in waves are presented. Initially, speed loss was determined in regular waves with a constant propeller speed. The results were compared with the model test performed at HSVA for validation purposes (Valanto, 2015). In the next step, the speed loss in long-crested irregular waves was determined. In this case, engine dynamics were considered. Except for the model of en-

gine dynamics, the simulation setup was similar for both computations. To enable an reasonable comparison between computed and measured attainable speeds the computations were performed in model scale. Due to scaling effects regarding the ship resistances and the operation point of the propeller, scaling effects may have a significant influence on the attainable speed. Thus, full scale extrapolation includes uncertainties.

First, the numerical setup will be presented in the following. Then, the results of the computations of the attainable speed in regular and irregular waves will be presented and discussed.

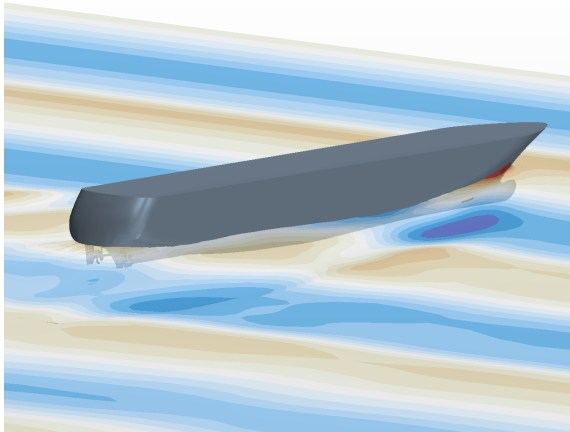


Figure 91: Wave pattern for the free-running Cruise Ship with constant propeller speed at $n = 14.8\text{rps}$ and $\lambda_w/L = 0.89$

8.1 Computational Procedure

The computations were essentially set up similar to the previously presented propulsion computations, see section 6. However, a different grid configuration was used to account for large ship motions and propeller rotation simulta-

neously. As discussed earlier, the previously used moving grid approach has drawbacks when modeling large ship rotations, because large relative motions between the free surface and numerical grid in the far field occur. This caused instability and non-physical deformation of the free surface at the inlet and outlet boundaries.

To overcome this issue, the rotations of the ship were realized using a morphing algorithm. Therefore, the domain was split into a "morphing" and a "moving" region. To avoid cell deformation in the vicinity of the propeller, which also had a negative effect on numerical stability, a third region around the hull was implemented. This "hull" region was rigid and followed all ship motions. The moving region was linked to the vertical and horizontal translations only (moving grid technique). Relative motions between the hull and moving region were realized by cell deformation in the morphing region. The grid setup is shown in figure 92. In this figure, blue indicates the moving region, brown indicates the morphing region, and gray indicates the hull region. In general, the resolution of the hull (including y^+ values), propeller and free surface was adopted from the propulsion computations.

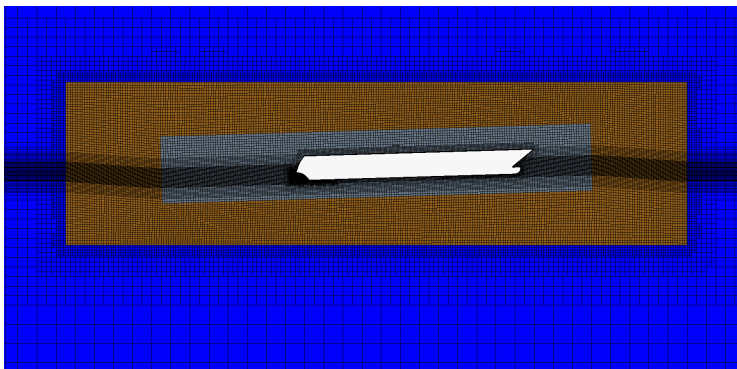


Figure 92: Numerical grid used for computations of the speed loss in regular and irregular head waves

Table 13: *Speed and wave parameters of the performed computations*

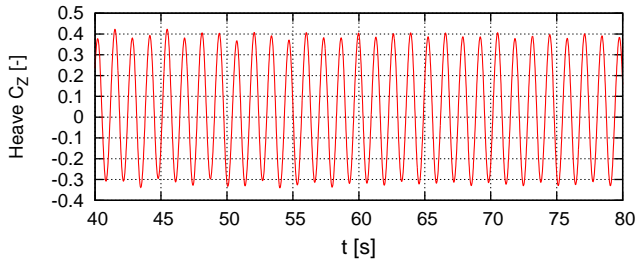
| n [rps] | λ_W/L [-] | h_W [m] | h_W/λ_W [%] |
|-----------|-------------------|------------|---------------------|
| | | Calm Water | |
| | 0.22 | 1.20 | 2.47 |
| | 0.28 | 1.55 | 2.52 |
| | 0.39 | 2.17 | 2.53 |
| | 0.49 | 3.6 | 3.34 |
| 14.8 | 0.66 | 3.6 | 2.48 |
| | 0.79 | 3.6 | 2.07 |
| | 0.89 | 3.6 | 1.84 |
| | 0.98 | 3.6 | 1.67 |
| | 1.41 | 3.6 | 1.16 |
| | 1.8 | 3.6 | 0.91 |
| | 2.5 | 3.6 | 0.65 |

8.2 Speed Loss in Regular Waves

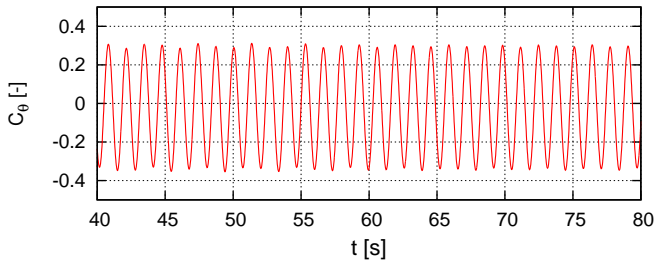
The speed loss measurements of the cruise ship model in regular waves were performed at HSVA (Valanto, 2016). The wave parameters and the propeller speed, n , are presented in table 13.

Computations were initialized with the calm water speed, $v = 1.8$ m/s, and the according propeller speed, $n = 14.8$ rps. The model was let free after five seconds and the speed dropped instantly. After the ship speed converged, the speed was averaged for multiple encounter periods. Speed loss was defined as the difference between the mean speed in waves and the calm water speed. Figure 91 shows the wave pattern of the free-running cruise ship in regular head waves with $\lambda_W/L = 0.89$.

Figure 93 shows the time histories of the heave and pitch motions of the cruise ship. The motions are nearly unaffected by ship speed and are similar to the motions in the propulsion tests performed with constant speed. The time histories of the model tests are not available; thus, only the computational results are shown.



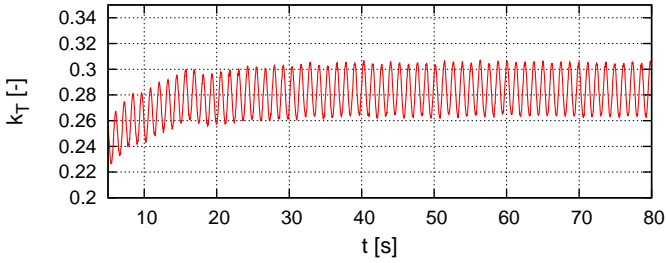
(a) Heave



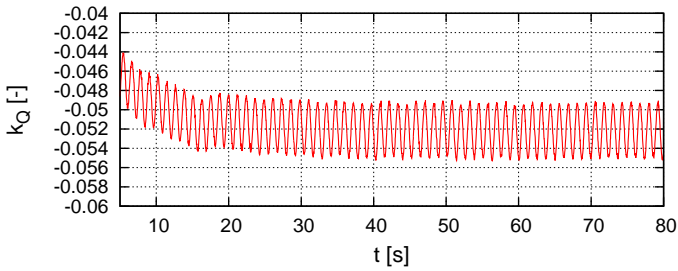
(b) Pitch

Figure 93: Heave and pitch motions for the free-running Cruise Ship in regular head waves with propeller speed at $n = 14.8\text{rps}$ and $\lambda_w/L = 0.98$

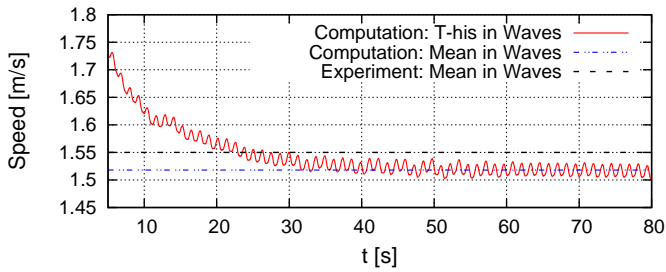
Figure 94 shows the time histories of the computed propeller thrust and torque and the corresponding ship speed. The time histories oscillate with the encounter period of the waves. Initially, the speed decreases rapidly until a constant running average is reached. The correlation between propeller forces and ship speed is obvious. The propeller load increases when the ship speed decreases due to a lower inflow velocity. A relatively long physical time needs to be computed to cover the final speed decrease. Constant mean ship speeds are achieved after ≈ 50 seconds, corresponding to 300 seconds in full scale.



(a)



(b)



(c)

Figure 94: Propeller thrust (top), torque (middle) and ship speed (bottom) for the Cruise Ship at $n = 14.8\text{rps}$ and $\lambda_W/L = 0.98$

Figure 95 presents a comparison between the computed and measured speed losses in regular head waves. With the mean speed in waves, v_W , and the calm water speed, v_M , the speed loss is defined as $(v_W - v)/v$. Speed loss is presented in percentage of the calm water speed.

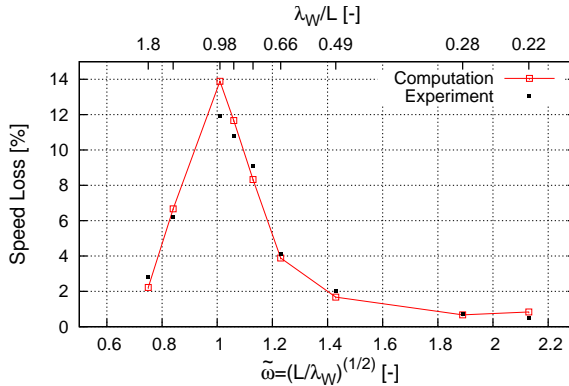


Figure 95: Computed and measured speed losses for the Cruise Ship in regular waves

Overall, very good agreement between the measured and computed speed losses is obtained. The maximal speed loss from the tests is approximately 11%, whereas that from the computation is approximately 14%. Thus, the numerical method used in combination with the chosen setup proved to be suitable for this type of investigation.

8.3 Speed Loss in Irregular Waves

In adverse conditions, such as maneuvering or heavy weather, ship resistance increases and the propeller is highly loaded. The current propeller power may overstep the maximum power the engine delivers. This situation causes an instant drop in the engine speed. Simultaneously, however, if the propeller torque is lower than the engine limits, then the current rotation rate increases again. It stands to reason that these permanent changes in the rotation rate of the varying loaded propeller have a significant influence on the speed loss of a ship in adverse sea states. To take this issue into consideration, an engine dynamics model developed at ISMT was implemented and attached to the RANS flow solver (el Moctar et al. 2015). This model is based on a simplified engine curve. At every time step, the current propeller torque Q_P is compared with the present maximal engine torque Q_E ; if Q_P is larger than Q_E , the propeller speed is reduced, and vice versa. Limits are a maximal and a minimal rotation rate. To increase the numerical stability and to avoid instantaneous jumps in the rotation rate, a maximal acceleration of rotation rate was introduced. The limiting engine characteristics are presented in table 14.

Table 14: Engine characteristics used for computations

| | Ship | Model |
|---------------------------------------|---------|-------|
| Max. Rotation Rate [1/min] | 158.0 | 948.0 |
| Min. Rotation Rate [1/min] | 158.0 | 948.0 |
| Max. Engine Torque [Nm] | 46656.0 | 1.0 |
| Max. Acceleration [1/s ²] | 0.16 | 1.0 |

The JONSWAP spectrum, as reported by Hasselmann (1973), was used to model the irregular waves. The peak enhancement factor, $\gamma = 3.3$, significant wave height, $H_S = 0.15$ m, and peak period, $T_P = 1.33$ s, according to 5.4 m and 7.98 s in ship scale, were chosen. Figure 96 shows a section of the resulting wave pattern in the vicinity of the model and a time history of the wave elevation beside the model’s bow.

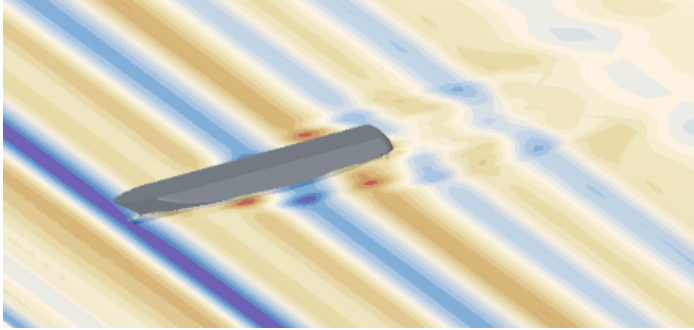
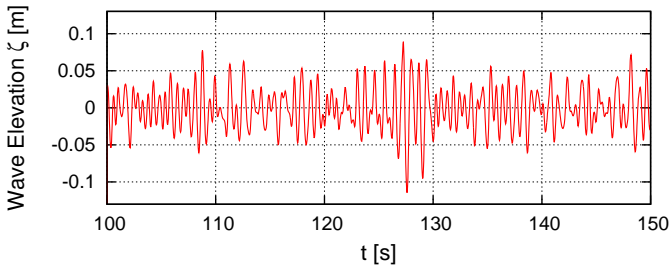


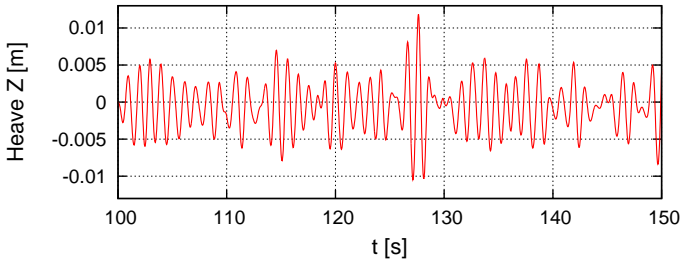
Figure 96: Wave pattern around the free-running Cruise Ship in irregular waves according to JONSWAP spectrum with $\gamma = 3.3$, $H_S = 0.15\text{m}$, and $T_p = 1.33\text{s}$, taking engine dynamics into account

The corresponding time histories of the heave and pitch motions are presented in figure 97. In contrast to the motion behavior in regular waves, wave elevation and motion amplitudes do not correlate directly. Figure 98 shows the varying propeller speed and the corresponding propeller torque and thrust. The engine is not capable of turning the propeller with the initial speed during the simulation. The rotation speed of 15.09 rps rapidly decreases until it oscillates around a constant running mean value of 12.2 rps. After this decrease in the propeller speed, the propeller moment and force level out at the torque limit of 0.5 Nm and a thrust of 18.7 N. The oscillation amplitudes are approximately 12.5% of the mean values.

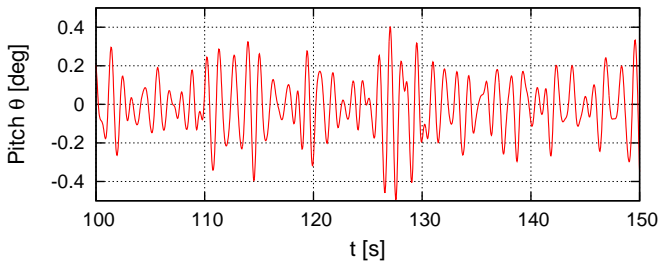
Finally, figure 99 shows the ship speed of the cruise ship in irregular waves. It behaves similarly to the propeller speed. Initially, the ship speed significantly decreases, and then it oscillates around a relatively constant running mean. For this case, the attainable speed is approximately 1.66 m/s, which means a speed loss of 8% in these wave conditions only.



(a) Wave elevation

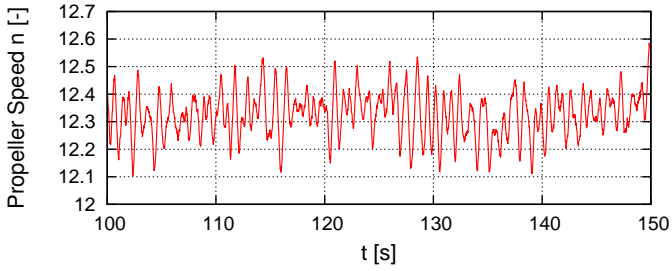


(b) Heave

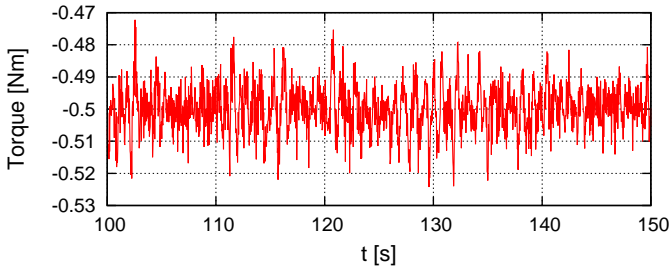


(c) Pitch

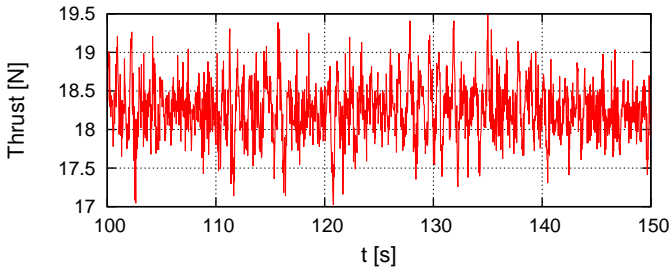
Figure 97: Time histories of the wave elevation, heave and pitch motions for the Cruise Ship in irregular waves according to JONSWAP spectrum with $\gamma = 3.3$, $H_S = 0.15\text{m}$, and $T_P = 1.33\text{s}$ taking engine dynamics into account



(a) Propeller speed



(b) Torque



(c) Thrust

Figure 98: Propeller speed, torque, and thrust for the Cruise Ship in irregular waves according to JONSWAP spectrum with $\gamma = 3.3$, $H_S = 0.15\text{m}$, and $T_P = 1.33\text{s}$ taking engine dynamics into account

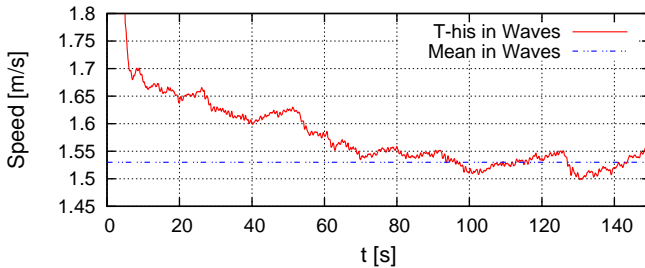


Figure 99: Computed speed loss for the Cruise Ship in irregular waves according to JONSWAP spectrum with $\gamma = 3.3$, $H_S = 0.15\text{m}$, and $T_P = 1.33\text{s}$ taking engine dynamics into account

8.4 Conclusion

The speed loss of the cruise ship in regular and in irregular waves has been computed. An engine dynamics model has been implemented and used for the irregular wave computations. Computations were performed in model scale. This enables a reasonable comparison with experimental results. However, full scale extrapolation is questionable.

The results in regular waves showed very good agreement with the experimental values. With constant propeller speed, $n = 14.8$ rps, the maximal speed loss occurs in waves of $\lambda_W/L = 1.0$ and $h_W = 0.1$ m. In this case, the speed in waves was 14% lower than the corresponding calm water speed. In general, the plot of the speed loss versus wave length behaves similar to the quadratic transfer function of the wave-added resistance.

Computations with irregular waves showed plausible results. However, experimental data were not available. Considering engine dynamics, not only the ship speed, but also the propeller force, moment and speed constantly vary. Thus, very long simulation times are necessary to determine a constant mean speed loss. In irregular waves, according to JONSWAP with $h_S = 0.15$ m and $T_P = 1.33$ s, the speed loss of the cruise ship was about 8% of the calm water speed.

Generally, RANS-based methods are capable of computing the speed loss even in irregular waves and considering the engine dynamics. However, the computational effort is very high; thus, a systematic investigation is very time consuming. However, results could be used to develop more efficient BEM methods.

9 Conclusion and Outlook

In this thesis, systematic investigations of the performance of ships in waves were conducted. Specifically, ship motion, the wave-added resistance, and the propulsion in waves were investigated. Four different ship types, namely, a Cruise Ship, the Containership "Duisburg Test Case", the Tanker "KVLCC2" and the well-known test case Wigley Hull, were considered. Commonly used methods based on empirical formulas or the potential theory, mostly do not account for nonlinearities, such as viscosity, wave breaking, flow separation etc.. Thus, advanced numerical methods based on the solution of the Reynolds-averaged Navier-Stokes equation were used, to account for nonlinearities related to resistance and propulsion of ships in waves. Discretization errors were evaluated by performing grid studies. When possible, computations were performed using similar numerical grids to minimize errors originating from different simulation setups. Actual wave amplitudes were monitored and used for normalization. The time histories of the forces and mean motion amplitudes were carefully analyzed by performing Fourier analysis for multiple encounter periods. When possible, the results of the computations were compared with experimental data. In general, very good agreement was obtained.

Predicting the wave-added resistance of ships remains a challenge. Nevertheless, the practical relevance of this subject motivated systematic investigations of the use of advanced numerical methods to analyze the added resistance of ships in waves. Initially, discretization errors were investigated. Then, based on the outcome, spatial and time-dependent discretizations suitable for simulations were identified. Furthermore, appropriate numerical methods to predict the wave-added resistance were introduced. Two findings were important. On the one hand, computations of the calm water resistance and the wave-added resistance in waves should be conducted on the

same numerical grid. On the other hand, the wave-added resistance should always be normalized against the actual wave amplitude, not the targeted wave amplitude. Ship motions and the wave-added resistance were computed for the four ship types and compared to the experimental model test measurements. In general, the computations and measurements correlated favorably. This was also the case for the wave-added resistances in short and long waves, thereby demonstrating that the methods based on solving the Reynolds-averaged Navier-Stokes equations were capable of predicting reliable wave-induced first- and higher-order responses, such as ship motions and wave-added resistance, respectively. The results showed that radiation forces were affected more strongly by ship speed than diffraction forces. Thus, peaks of added resistance coefficients were less pronounced at lower ship speeds. By subtracting the frictional resistance in calm water from the frictional resistance in waves, the frictional-added resistance was determined. The computations showed that, in short waves, friction accounted for a significant part of the total added resistance, namely, 20% or even more. However, full-scale computations showed that this effect was less pronounced at full scale. Diffraction and radiation forces at different frequencies were investigated, where diffraction forces were obtained by restraining the ship in waves and the radiation forces were obtained by prescribing the motions of the ship in calm water. In long waves, the sum of diffraction and radiation forces did not match the total resistance, i.e., the interaction of these two force components had to be accounted for. In short waves, the diffraction part of the total resistance was dominant as almost no ship motions were induced. Generally, the assumption of a quadratic correlation between wave height and added resistance was confirmed for ships advancing in waves of moderate to long wave lengths (mostly linear). However, this assumption did not hold for ships advancing in short waves because diffraction was dominant in short waves (nonlinear). The computed wave-added resistances in oblique waves considering only heave, roll and pitch motions showed fair agreement with measurements also considering surge, sway, and yaw. This does not hold for side force and yaw moment.

The nominal wake fraction was determined for three different ship types in 12 different wave lengths ranging from 0.2 to 2 times the ship length. The

time-averaged nominal wake fraction decreases in waves. Its change depends on the ship type. The wake fraction of the twin-screw cruise ship was a maximum 13.9%, and for the single-screw ships (container ship and tanker), was at most $\approx 22\%$ lower than the according calm water values. In contrast, the oscillation amplitudes of the wake fraction in waves were almost independent of ship type. For all ship types, the amplitudes of the wake fraction time histories due to orbital velocities and ship motions were in the same range. It may be summarized that the change of the time-averaged wake fraction in waves depends on ship's hull form and the position of the propeller, whereas the oscillation amplitudes of the wake fraction in waves depend on the wave parameters. Furthermore, the amplitudes of the wake fraction time histories in waves are larger than the changes of the averaged wake fraction. Thus both effects should be taking into account when designing a propeller.

The influence of regular head waves on propulsion characteristics of a twin screw cruise ship and the single screw containership DTC was numerically and experimentally investigated using a RANS based flow-solver. Employing the sliding interface method allowed the geometrically modeled propeller to rotate when needed. All computations were performed on the same numerical grids to limit errors originating from different spatial and temporal discretizations. Grid studies were performed to evaluate discretization errors occurring in separate mesh regions, such as regions surrounding the hulls and the rotating propellers. Numerical results were compared to experimental measurements obtained from model tests. Discretization errors may significantly influence computed propeller torque, but computed propeller thrust was nearly unaffected. Fair agreement between measured and computed thrust and torque was obtained on the fine grids. Computations of the towed models in calm water and in regular head waves compared favorably to experimental measurements. Computations of the self-propelled model in calm water and in regular head waves were performed to obtain hull-propeller interaction characteristics and propeller forces. Propeller forces were sensitive to temporal discretizations; therefore, to obtain accurate results, it was necessary to specify small time steps, leading to at most one degree of propeller rotation per time step. Such small time steps, together with the use of the sliding interface method, caused computations to be time consuming. Gen-

erally, computed forces compared favorably to measurements. The greatest deviation between computed and measured propeller forces for all cases was less than five percent; the average deviation, about 3.5%. Numerical results were used to estimate propulsion characteristics; specifically, propulsion efficiency, rotative efficiency, hull efficiency, and propeller open water efficiency. This required accurate computation of intermediate steps as well as careful evaluation of results. All values, including thrust deduction and wake fraction, correlated favorably to measurements. It was found that the propulsion efficiency decreased in waves. Based on the considered cases, this was related to the configuration of the propulsion units themselves. The main cause for the decreasing propulsion efficiency of the twin screw ship was the propeller efficiency, which in turn depended on the propellers' operation point and, thereby, on the ship's wave-added resistance. For the containership however, beside the propeller efficiency also the hull efficiency changed in waves. Hence, for this ship not only the increased resistance, but the ever-changing flow surrounding the hull and the inflow to the propeller caused by the orbital fluid velocities and the ship motions affected its propulsion characteristics in waves.

The speed loss of the cruise ship in regular and in irregular waves has been computed. An engine dynamics model has been implemented and used for the irregular wave computations. Computations were performed in model scale. This enabled a reasonable comparison with experimental results. However, full scale extrapolation is questionable. The results in regular waves showed very good agreement with the experimental values. With constant propeller speed, $n = 14.8 \text{ rps}$, the maximal speed loss occurs in waves of $\lambda_W/L = 1.0$ and $h_W = 0.1 \text{ m}$. In this case, the speed in waves was 14% lower than the corresponding calm water speed. In general, the plot of the speed loss versus wave length behaves similar to the quadratic transfer function of the wave-added resistance. Computations with irregular waves showed plausible results. However, experimental data were not available. Considering engine dynamics, the propeller force -moment, and -speed vary constantly in addition to the ship speed. Thus, very long simulation times are necessary to determine a constant mean speed loss. In irregular waves, according to JON-SWAP with $h_S = 0.15 \text{ m}$ and $T_P = 1.33 \text{ s}$, the speed loss of the cruise ship

was about 8% of the calm water speed. Generally, RANS-based methods are capable of computing the speed loss even in irregular waves and considering the engine dynamics. However, the computational effort is very high; thus, a systematic investigation is very time consuming.

Novel and most considerable outcomes of the presented work are the following:

- Wave-added resistance could have a significant frictional part
- To determine the wave-added resistance the wave steepness is of significant importance. Actual wave amplitude should be used for the normalization
- Diffraction and radiation forces interact significantly in long waves
- Ship speed reduces radiation forces significantly, diffraction is nearly unaffected
- Nominal wake fraction oscillates significantly in waves and averaged values decrease
- Propulsive efficiency decreases in waves caused by the change of the open water efficiency, η_0 , and hull efficiency, η_H
- Prediction method of the speed loss in regular and irregular waves, taking engine dynamics into account

The obtained findings may be used to improve efficient methods for the prediction of the performance of ships in seaways. Furthermore, the results may be used to reconsider the calm water based design process.

In the future, social conscience and increasing environmental pollution intensify the conflict between environmental and safety issues in the marine industries. Therefore, it is essential to minimize emissions by improving the performance and efficiency of ships without reducing safety standards. In this context, seakeeping and required power in operational conditions, including maneuverability, will be of great interest in the future. Improved prediction methods and design procedures are needed. Going forward, an even better understanding of the influence of operational conditions on the required ship power is essential. Ability to perform full scale investigations of the ship's propulsion is one of the greatest advantages of advance numerical methods.

Conclusion and Outlook

To increase the reliability of full scale computations need to be addressed more extensively in the future. Following that path, future steps could be to challenge the frequently used spectral method by performing computations with irregular waves, to predict the drift forces in oblique waves, and to investigate the maneuverability in adverse conditions. Furthermore it would be very beneficial to initiate a full scale benchmark case to validate full scale computations.

Bibliography

- [1] Abdel-Maksoud, M., Menter, F. and Wuttke, H. (1998): *Viscous flow simulations for conventional and high-skew marine propellers*. Ship Technology Res., 64-71.
- [2] Bertram, V. (2000): *Practical Ship Hydrodynamics*. Oxford: Butterworth-Heinemann.
- [3] Carrica, P. M., Castro, A. M. and Stern, F. (2010): *Self-propulsion computations using a speed controller and a discretized propeller with dynamic overset grids*. J Mar Sci Technol.
- [4] Carrica, P. M., Fu, H. and Stern, F. (2011): *Computations of self-propulsion free to sink and trim and of motions in head waves of the KRISO Container Ship (KCS) model*. Applied Ocean Research, 33(2011), pp. 309-320.
- [5] Choi, J. E., Kim, J. H., Lee, H. G., Choi, B. J. and Lee, D. H. (2010): *Computational predictions of ship speed performance*. J Mar Sci Technol.
- [6] Cura-Hochbaum, A. and Vogt, M. (2008): *Maneuvering prediction for two tankers based on RANS calculations*. Copenhagen, Denmark: SIMMAN 2008.
- [7] Peric, M. and Schreck, E. (2009): *Advances in Simulation for Marine Engineering. In 2nd Asian Symposium on Computational Heat Transfer and Fluid Flow*. Jeju, Korea.
- [8] Boese, P. (1970): *A Simple Method for the Calculation of Resistance Increase of a Ship in a Seaway*. J. of Ship Technology Research, Vol. 17(86).

Bibliography

- [9] Brunswig, J. and el Moctar, O. (2004): *Prediction of Ship Motions in Waves Using RANSE*. Proc. of the 7th Numerical Towing Tank Symposium (NUTTS). Hamburg, Germany.
- [10] CD-Adapco. (2016): *Starccm+ User Guide 6.02.007*.
- [11] Dilk, V. (2012): *Comparison of different methods for the computation of the added resistance of ships in waves*.
- [12] Duan, W., and Li, C. (2013): *Estimation of added resistance for large blunt ship in waves*. Journal of Marine Science and Application, 12(1):1–12.
- [13] el Moctar, O., Lantermann, U., Mucha, P., Höpken, J., and Schellin T. E. (2015): *RANS-Based Simulated Ship Maneuvering Accounting for Hull-Propulsor-Engine Interaction* Ship Technol. Res. 61(3): 142-161
- [14] el Moctar, O., Shigunov, V., and Zorn, T. (2010): *Duisburg Test Case: Post-Panamax Container Ship for Benchmarking*. Ship Technology Research Journal, Vol. 59/3, pp. 50-64.
- [15] el Moctar, O. (2001): *Numerical computations of flow forces in ship manoeuvring*. Ship Technol. Res., 98-123.
- [16] el Moctar, O., Ley, J., and Oberhagemann, J. (2016): *Advanced Computational Methods for Hydroelastic Effects of Ships in Extreme Seas*. Ocean Engineering, Vol. 130, 659-673.
- [17] el Moctar, O., Oberhagemann, J., and Schellin, T. (2011): *Free Surface RANS Method for Hull Girder Springing and Whipping*. SNAME Trans., Vol. 119, pp. 48-66.
- [18] el Moctar, O., Sigmund, S., Ley, J., and Schellin, T. (2016): *Numerical and Experimental Analysis of Added Resistance of Ships in Waves*. J. Offshore Mech. Arct. Eng 139(1), 011301.
- [19] el Moctar, O., Sigmund, S. Ley, J., and Schellin, T. (2015): *Numerical and Experimental Analysis of Added Resistance of Ships in Waves*. Proc.

- 34rd Int. Conf. on Ocean, Offshore, and Arctic Eng., st. Johns, Canada, OMAE2015-42403.
- [20] el Moctar, O., Sprenger, F., Schellin, T., and Papanikolaou, A. (2016): *Numerical and Experimental Investigations of Ship Maneuvers in Waves*. Proceedings of the 35th International Conference on Ocean, Offshore and Arctic Engineering OMAE 2016. Busan, South Korea.
- [21] Faltinsen, O. M. (1998): *Sea Loads on Ships and Offshore Structures*.
- [22] Faltinsen, O. M., Minsaas, K., Liapis, N., and Skjrdal, S. O. (1980): *Prediction of resistance and propulsion of a ship in a seaway*. The 13th Symposium on Naval Hydrodynamics , pp. 505–529.
- [23] Ferziger, J., and Peric, M. (2002): *Computational Methods for Fluid Dynamics*. 3rd ed. Berlin Heidelberg New York: Springer Berlin.
- [24] Gerritsma, J., and Beukelman, W. (1972): *Analysis of the Resistance Increase in Waves of a Fast Cargo Ship*. Int. Shipbuilding Progress, Vol. 19, 285-293.
- [25] Guo, B., and Steen, S. (2011): *Evaluation of added resistance of kvlcc2 in short waves*. Journal of Hydrodynamics, 23(6):709–722.
- [26] Hadler, J. (1958): *Coefficients for international towing tank conference 1957 model ship correlation line*. Tech. rep., DTIC Document.
- [27] Hasselmann K., T.P. Barnett, E. Bouws, H. Carlson, D.E. Cartwright, K. Enke, J.A. Ewing, H. Gienapp, D.E. Hasselmann, P. Kruseman, A. Meerburg, P. Mller, D.J. Olbers, K. Richter, W. Sell, and H. Walden (1973): *Measurements of wind-wave growth and swell decay during the Joint North Sea Wave Project (JONSWAP)*. Ergnzungsheft zur Deutschen Hydrographischen Zeitschrift Reihe, A(8) (Nr. 12), p.95.
- [28] Hirt, C.W.; Nichols, B.D. (1981): *Volume of fluid (VOF) method for the dynamics of free boundaries*.

Bibliography

- [29] International Towing Tank Conference (2008): *Testing and Data Analysis - Resistance Test*. Procedure 7.5-02-02-01.
- [30] International Towing Tank Conference (2011): *Recommended Procedures and Guidelines - Practical Guidelines for Ship CFD Applications*.
- [31] Joosen, W. P. (1966): *Added resistance in waves*. 6th Symposium on Naval Hydrodynamics.
- [32] Journée, J. (2003): *Experiments and Calculations on 4 Wigley Hull Forms in Head Waves*. Netherlands 1992: Delft University of Technology, Ship Hydromechanics Laboratory. Neudruck des Berichts 0909 (1992).
- [33] Journee, J.M.J. & W.W. Massie (2001): *Offshore Hydromechanics*. Kapitel 5
- [34] Kashiwagi, M., Ikeda, T., and Sasakawa, T. (2010): *Effects of Forward Speed of a Ship on Added Resistance in Waves*. J. Offshore and Polar Eng., Vol. 20(3), pp. 196-203.
- [35] Kim, K., and Kim, Y. (2011): *Numerical study on added resistance of ships by using a time-domain Rankine panel method*. Ocean Engineering, 38(13):1357–1367.
- [36] Kim, K.-H., Seo, M.-G., and Kim, Y. (2012): *Numerical Analysis on Added Resistance of Ships*. International Journal of Offshore and Polar Engineering, Vol. 22, No. 1, pp. 21-29.
- [37] Krueger, S. (2004): *Grundlagen der Propulsion*. Vorlesungsskript TUHH.
- [38] Krueger, S. (2015): *Umweltbedingte Zusatzwiderstaende*. Vorlesungsskript TUHH.
- [39] Kuroda, M., Tsujimoto, M., Fujiwara, T., Ohmatsu, S., and Takagi, K. (2008): *Investigation on components of added resistance in short waves*. Journal of the Japan Society of Naval Architects and Ocean Engineers, (8):171–176.

- [40] Krasilnikov, V. (2013): *Self-Propulsion RANS Computations with a Single-Screw Container Ship*. Launceston, Australia: SMP 2013.
- [41] Larsson, L., Stern, F., and Visonneau, M. (2010): *A Workshop on Numerical Ship Hydrodynamics*. Proceedings, Vol II. Göteborg.
- [42] Ley, J., Sigmund, S., and el Moctar, B. (2014): *Numerical Prediction of the Added Resistance of Ships in Waves*. Proceedings of the ASME 33th International Conference on Ocean, Offshore and Arctic Engineering. San Francisco: OMAE 2014.
- [43] Lloyd, A. R. J. M. and Frina (1998): *SEAKEEPING: Ship behaviour in rough weather*.
- [44] Liu, S., Papanikolaou, A., and Zaraphonites, G. (2011): *Prediction of Added Resistance of Ships in Waves*. J. Ocean Engineering, Vol. 38, pp. 641-650.
- [45] Lübke, L. (2005): *Numerical simulation of the flow around the propelled KCS*. Tokyo, Japan: CFDWS05.
- [46] Lyu, W., and el Moctar, O. (2017): *Numerical and experimental investigations of wave-induced second order hydrodynamic loads*. Ocean Engineering, pp. 197-212.
- [47] Maruo, H. (1957): *The Excess Resistance of a Ship in a Rough Sea*. Int. Shipbuilding Progress, Vol. 4, 337-345.
- [48] Maruo, H. (1960): *The drift force on a body floating in waves*. J. Ship Research, pp. 1-10.
- [49] Maruo, H. (1963): *Resistance in waves*. The Society of Naval Architects of Japan, Vol. 8, 60th anniversary Series.
- [50] Menter, F. R. (1994): *Two-Equation Eddy-Viscosity Turbulence Models for Engineering Applications*. AIAA Journal, Vol. 32, pp. 1598-1605.
- [51] Menter, F. R. (1993): *Zonal Two Equation $k-\omega$ Turbulence Models for Aerodynamic Flows*.

- [52] MEPC I. (2011): *Amendments to marpol annex vi on regulations for the prevention of air pollution from ships by inclusion of new regulations on energy efficiency for ships.*
- [53] Muzaferija, S., and Peric, M. (1999): *Computation of free-surface flows using interface-tracking and interface-capturing methods.* Computational mechanics publications.
- [54] Oberhagemann, J. (2016): *Dissertation: On Prediction of Wave-Induced Loads and Vibration of Ship.* Duisburg.
- [55] Oberhagemann, J., and el Moctar, O. (2007): *A Simplified Approach to Investigate Fluid-Structure Coupling Effects on Slamming Loads of Ships.* Proc. 10th Numerical Towing Tank Symposium, (S. pp. 150–155). Hamburg.
- [56] Oberhagemann, J., Shigunov, V., and el Moctar, O. (2012): *Application of CFD in Long-Term Extreme Value Analyses of Wave Loads.* Ship Technology Research 59(3), pp. 4-22.
- [57] openfoamwiki (2016): Retrieved from https://openfoamwiki.net/index.php/OpenFOAM_guide/The_PIMPLE_algorithm_in_OpenFOAM.
- [58] Papanikolaou, A., and Schellin, T. (1993): *A Three-Dimensional Panel Method for Motions and Loads on Ships with Forward Speed.* Ship Technology Research, 39.
- [59] Sadat-Hosseini, H., Wu, P.-C., Carrica, P. M., Kim, H., Toda, Y., and Stern, F. (2013): *CFD Verification and Validation of Added Resistance and Motions of KVLCC2 with Fixed and Free Surge in Short and Long Head Waves.* Ocean Engineering 59, pp.240-23.
- [60] Salvesen, N. (1978): *Added resistance of ships in waves.* J. Hydrodynamics, Vol. 12, No. 1, pp. 24-34.
- [61] Salvesen, N., Tuck, O., and Faltinsen, O. (1970): *Ship Motions and Sea Loads.* SNAME Trans., Vol. 78, pp. 250-287.

- [62] Schellin, T., and el Moctar, O. (2007): *Numerical Prediction of Impact-Related Wave Loads on Ships*. ASME J. Offshore Mechanics and Arctic Engg., Vol. 129(1), pp. 39-47.
- [63] Seo, M., Park, D., Yang, K., and Kim, Y. (2013): *Comparative study on computation of ship added resistance in waves*. Ocean Engineering, 73(C):1–15.
- [64] Seo, M., Yang, K., Park, D., and Kim, Y. (2014): *Numerical analysis of added resistance on ships in short waves*. Ocean Engineering, 73(C):1–15.
- [65] Sigmund, S. and el Moctar, O. (2017): Numerical and Experimental Investigation of Propulsion in Waves, Ocean Engineering.
- [66] Sigmund, S. and el Moctar, O. (2017): Advanced numerical and experimental investigation of added resistance of different ship types in short and long waves, Ocean Engineering.
- [67] Sigmund, S. and el Moctar, O. (2016): Numerical Prediction of the Propulsion Characteristics of Ships in Waves, Proc. 35th Int. Conf. on Ocean, Offshore and Arctic Eng., Busan, South Korea, OMAE2016-54793.
- [68] SIMMAN (2008): Retrieved from <http://www.simman2008.dk/KVLCC/KVLCC2/tanker2.html>
- [69] Simonsen, C. D., Otzen, J. F., S., J., and Stern, F. (2013): *EFD and CFD for KCS heaving and pitching in regular head wave*. Journal of Marine Science and Technology, Vol 18, Issue 4, pp. 435-459.
- [70] Söding, H. (1982): *Bewegungen und Belastungen der Schiffe im See-gang*. Vorlesungsmanuskript Nr. 18: Institut Für Schiffbau der Universität Hamburg.
- [71] Söding, H., Shigunov, V., Schellin, T., and el Moctar, O. (2014): *A Rankine Panel Method for Added Resistance of Ships in Waves*. ASME J. Offshore Mechanics and Arctic Eng., Vol. 136.

- [72] Söding, H., von Graefe, A., Shigunov, V., and el Moctar, O. (2012): *Rankine Source Method for Seakeeping Predictions*. Proc. 31th Int. Conf. on Ocean, Offshore and Arctic Eng. OMAE2012-83450.
- [73] Spalart, P.R. (1997): *Comments on the feasibility of LES for wing and on a hybrid RANS/LES approach*.
- [74] Sportelli, M., and Huijsmans, R. (2012): *Added resistance in short waves: a ray theory approach*. 27th International Workshop on Water Waves and Floating Bodies.
- [75] Sprenger, F., Maron, A., Delefortrie, G., and Papanikolaou, A. (2016): *Experimental Studies on Seakeeping and Manoeuvrability in Adverse Weather Conditions*. Proceedings SNAME2016 Annual Conference . Seattle.
- [76] Ström-Tejsen, H. J., Yeh, Y., and Moran, D. (1973): *Added Resistance in Waves*. SNAME Trans., Vol. 81, pp. 109-143.
- [77] Tsujimoto, M.; Kuroda, M.; Shibata, K. and Takagi, K. (2008): *A practical correction method for added resistance in waves*.
- [78] Turnock, S., Tanaka, H., Kim, J., Wu, B., Fu, T., Takinaci, A., and Mikkola, T. (2014): *The resistance committee-final report and recommendations to the 27th ITTC*. Proceeding of 27th International Towing Tank Conference.
- [79] Valanto, P., and Hong, Y. (2015): *Experimental Investigation of Ship Waves Added Resistance in Regular Head, Oblique, Beam and Following Waves*. Hawaii, USA: ISOPE 2015.
- [80] Vorhoelter, H. (2001): *Numerische Analyse des Nachstroms und der Propellereffektivitaet am manoevrierenden Schiff (in german)*. Ph.D. thesis, Hamburg University of Technology
- [81] Winden, B., Turnock, S. and Hudson, D. (2014): *A RANS modelling approach for predicting powering performance*. Int. J. Nav. Archit. Ocean Eng., pp. 418-430.

- [82] Wu, P.-C.; Sadat-Hosseini, H.; Stern, F.; Toda, Y. (2013): *Nominal Wake Fluctuation due to Waves: Volume Mean and Distribution Based on CFD*. DOI: 10.2534/jjasnaoe.24.13.
- [83] Wu, P.C., Kim, H., Hayashi, Y., Oshita, S., Toda, Y. (2012): *Added resistance and phase averaged wake field of KVLCC2 model ship in waves*. Proc. of EAISS2012.
- [84] Yasukawa, H., Matsumoto, A., Ikezoe, S. (2016): *Wave Height Effect on Added Resistance of Full Hull Ships in Waves*. The Japanese Society of Naval Architects and Ocean Engineers, JASNAOE, pp. 45-54.